

Reconstruction of air-shower parameters with a sparse radio array

Zur Erlangung des akademischen Grades eines
DOKTORS DER NATURWISSENSCHAFTEN
bei der Fakultät für Physik des
Karlsruher Instituts für Technologie (KIT)

genehmigte

DISSERTATION

von

Dmitriy Kostunin
aus Irkutsk

Karlsruhe
November 2015

Tag der mündlichen Prüfung: 11. Dezember 2015

Referent: Prof. Dr. Johannes Blümer,
Institut für Kernphysik und Institut für Experimentelle Kernphysik
Koreferent: Prof. Dr. Michael Feindt,
Institut für Experimentelle Kernphysik
Betreuer: Dr. Frank Gerhard Schröder,
Institut für Kernphysik

Abstract

Reconstruction of air-shower parameters with a sparse radio array

Since the discovery of cosmic rays more than hundred years ago, the instruments for their detection have developed and advanced significantly. Currently, optical techniques of air-shower detection, namely air-Čerenkov and fluorescence light detection, provide the highest resolution for the primary energy, E_{pr} , (within about 15%) and the atmospheric depth of the shower maximum, X_{max} , (within about 20 g/cm²). The main disadvantages of these techniques are the low duty-cycle (less than 15%) and high costs of deployment and maintenance. The detection of the radio emission from air-showers induced by high-energy cosmic ray particles yields an alternative to the established techniques. Radio detection offers increased duty cycle and decreased cost of deployment and operation. At the moment there are a few of experiments exploiting this technique, one of them is Tunka-Rex.

The Tunka Radio Extension (Tunka-Rex), deployed in 2012, is an array of antenna stations, interspersed with Tunka-133, an air-Čerenkov detector in Siberia near Lake Baikal. With a spacing of antenna stations of about 200 m, it covers an area of 1 km² and measures cosmic rays with primary energies above 10¹⁷ eV. For the reconstruction of air-showers, methods optimized for this particular sparse geometry were developed using simulations done with the CORSIKA/CoREAS software. The applicability of the methods has been successfully tested on Tunka-Rex measurements of 2012-2014.

The present study consists of two main parts: a theoretical description of the methods of air-shower reconstruction using the radio technique, and analysis of Tunka-Rex data using the developed methods. The main results are:

- A parameterization for the lateral distribution of radio amplitudes has been developed. The asymmetric two-dimensional lateral distribution function (LDF) can be simplified to a one-dimensional symmetric LDF by introducing one single parameter, namely, the relative strength of Askaryan, i.e. charge-excess, signal emission compared to geomagnetic emission. This one-dimensional symmetric LDF is particularly well suited for sparse arrays.
- Parameters of the developed LDF are used for the reconstruction of E_{pr} and X_{max} . The theoretical limit for the resolution is 10% for E_{pr} and 20 g/cm² for X_{max} as derived from the CoREAS simulations.
- The comparison between the radio and air-Čerenkov techniques shows that Tunka-Rex has a resolution of about 15% and 38 g/cm² for E_{pr} and X_{max} , respectively. Considering the Tunka-Rex reconstruction has been tuned on the CoREAS simulation, this gives confidence in the results of both detectors as well as the CoREAS simulation code.

Zusammenfassung

Rekonstruktion von Luftschauer-Parametern mit einem großen Radioantennenfeld

Seit der Entdeckung kosmischer Strahlung vor über 100 Jahren, haben sich die Detektoren, die für ihren Nachweis eingesetzt werden, signifikant weiterentwickelt. Optische Detektoren, die Luft-Čerenkov- oder Fluoreszenzstrahlung nachweisen, erreichen die höchste Genauigkeit für die Rekonstruktion der Primärenergie, E_{pr} (ungefähr 15%) und der atmosphärischen Tiefe des Schauermaximums, X_{max} (ungefähr 20 g/cm²). Der Nachteil dieser Methoden liegt in ihrer niedrigen Einsatzdauer (unter 15%) und den hohen Bau- und Betriebskosten. Eine mögliche Alternative zu den etablierten Methoden ist die Messung der Radioemission durch Luftschauer kosmischer Strahlung. Radiodetektion bietet einen hohen Betriebszyklus von fast 100% und geringe Kosten für Aufbau und Betrieb. Momentan gibt es einige Experimente, die diese Methode nutzen, darunter Tunka-Rex.

Die Tunka-Radio-Extension (Tunka-Rex), ist ein Radiodetektor, der 2012 auf dem Messfeld von Tunka-133, einem Luft-Čerenkov-Detektor in Sibirien, in der Nähe des Baikalsees, aufgebaut wurde. Mit einem Antennenabstand von 200 m schließt er ein Gebiet von rund 1 km² ein, um kosmische Strahlung oberhalb von 10¹⁷ eV von Primärenergien zu messen. CORSIKA/CoREAS-Simulationen wurden verwendet, um Rekonstruktionmethoden für die spezielle Geometrie des Detektors mit großen Antennenabständen zu entwickeln. Die Methoden wurden mit Tunka-Rex-Messungen von 2012-2014 erfolgreich getestet.

Die vorliegende Arbeit besteht aus zwei Teilen: einer theoretischen Beschreibung der Methoden für die Luftschauer-Rekonstruktion mit einem Radiodetektor und der Analyse der Tunka-Rex-Messungen mit den entwickelten Methoden. Die Hauptergebnisse sind:

- Es wurde eine verbesserte Parametrisierung der Lateralverteilung der Radioamplituden entwickelt. Die asymmetrische zweidimensionale Lateralverteilungsfunktion (LDF) kann zu einer eindimensionalen symmetrischen LDF vereinfacht werden. Hierfür wird ein einziger Parameter eingeführt, der die relative Stärke des Signals durch die Änderung des Ladungsüberschusses, also des Askaryaneffekts, im Verhältnis zum Signal aus der geomagnetischen Emission beschreibt. Diese eindimensionale LDF ist besonders gut für Antennenfelder mit großen Antennenabstand geeignet.
- E_{pr} und X_{max} werden über Parameter der entwickelten LDF rekonstruiert. Die theoretisch erreichbare Auflösung in den CoREAS-Simulationen ist 10% für E_{pr} und 20 g/cm² für X_{max} .
- Ein Vergleich der Radio- und Luft-Čerenkov-Messungen zeigt, dass Tunka-Rex eine Auflösung von 15% und 38 g/cm² für E_{pr} und X_{max} hat. Da die Rekonstruktion an CoREAS-Simulationen angepasst wurde, ergibt sich ein konsistentes Gesamtbild. Denn Tunka-Rex stimmt nicht nur mit den Simulationen, sondern auch mit den Tunka-133-Messungen überein.

Contents

1. Introduction	1
2. Cosmic Rays	3
2.1. The nature of cosmic rays	3
2.2. Extensive air-showers	6
2.3. Air-shower detection techniques	9
2.3.1. Particle detectors	9
2.3.2. Imaging techniques	9
2.3.3. Non-imaging techniques	10
2.3.4. Satellites for air-showers	10
2.3.5. Radio detection	10
3. Radio emission from extensive air showers	11
3.1. Emission mechanisms	11
3.2. Models	13
3.3. Detection of the radio emission from air showers	14
3.3.1. Modern experiments	14
3.3.2. Neutrino detection	16
3.3.3. Radar methods for the detection of high-energy particles	16
3.3.4. Radio background	17
4. Tunka Radio Extension (Tunka-Rex)	19
4.1. Tunka astrophysical facility	19
4.1.1. Tunka-133	20
4.1.2. Tunka-HiSCORE	20
4.1.3. Tunka-Grande	21
4.1.4. Imaging air-Čerenkov telescopes	22
4.2. Setup of Tunka-Rex	22
4.2.1. Geometry and layout	22
4.2.2. Hardware properties	23
4.2.3. Systematic uncertainties of the setup	24
4.2.4. Signal window determination	26
4.2.5. Data-acquisition and signal-reconstruction pipeline	27
4.2.6. Beacon system	31
4.3. Tunka-Rex monitoring and background measurements	32
5. Lateral distribution of the radio emission	35
5.1. Introduction	35
5.1.1. Coherence of the radio emission	35
5.1.2. Lateral distribution beyond the Čerenkov effects	37
5.1.3. “Tomography” with a dense array	37
5.2. Simulation of radio pulses	38

5.2.1. Shower maximum determination	38
5.2.2. Reproducing Tunka-133 events	39
5.2.3. A three-dimensional simulation of the radio emission	41
5.3. Asymmetry	43
5.3.1. Introduction	43
5.3.2. Asymmetry behavior	44
5.3.3. Parameterization of asymmetry	46
5.4. Reconstruction of air-showers using the lateral distribution of radio amplitudes	50
5.4.1. Parameterization of lateral distribution	50
5.4.2. Reconstruction of energy and shower maximum	51
5.4.3. Systematic uncertainties	55
5.4.4. Influence of background	55
6. Measurement of energy and shower maximum	59
6.1. Concept of semi-blind analysis	59
6.2. Pre-reconstruction improvements	60
6.2.1. Amplitude correction for noise	60
6.2.2. Rejection of false positive signals	62
6.2.3. Optimization of the lateral distribution function	62
6.2.4. Concluding remarks	66
6.3. Quality cuts	66
6.4. Reconstruction of the full dataset	67
6.4.1. Energy reconstruction	69
6.4.2. Shower maximum reconstruction	71
6.4.3. Merged dataset with additional cut	74
6.4.4. Further improvements	78
6.5. Conclusion	79
7. Conclusion	81
7.1. Where to go	82
Appendix	83
A. Antennas connected to HiSCORE stations	83
B. Software configuration for Tunka-Rex	85
C. Remarks on the complexity of the methods	89
D. Magnetic field of the Earth	91
E. Example events	93
Bibliography	97
List of Figures	109
List of Tables	113

1. Introduction

One of the important achievements of fundamental physics in the 20th century was the discovery of cosmic rays. Elementary particles and nuclei reaching the Earth are directly related to the questions of the evolution of the Universe, star and galaxy development and different powerful processes taking part inside and outside of our galaxy. In the first half of the 20th century cosmic rays became a bridge between astrophysics and particle physics. It is surprising how many elementary particles were discovered using cosmic rays: the muon and the positron, π and K mesons, Λ and Ξ baryons. Later, the synergy of astrophysics, cosmic rays and particle physics formed a special field called astroparticle physics.

The detection of the cosmic rays is a challenging activity: either they can be measured at very high altitudes (by balloon or satellite experiments) or by surface arrays detecting radiation or secondary particles from air-showers produced after the collision of cosmic-ray particles with the atmosphere. The size of the arrays depends on the energy range they aim to measure: the flux of cosmic rays falls exponentially with energy, thus, detection of ultra-high energy cosmic rays requires areas up to thousands of square kilometers. Large-scale air-shower detectors exploiting established techniques are close to their economical limits: optical detectors are expensive and have low duty-cycle and particle detectors have limited sensitivity to the composition of primary cosmic ray particles. A compromise can be reached by using the radio technique for high-energy air-shower detection. It enables measurement almost around-of-clock and provides good sensitivity to the air-shower development, and, thus, to composition.

The first experiments applying the radio-technique, conducted in the 1960s, were in-competitive in comparison with particle detectors, and the radio technique was almost forgotten for years. The next generation of the radio detectors appeared only in the beginning of the 21st century. Current experiments have proven that with digital techniques, radio emission from air-showers can be measured, analyzed and interpreted. When this proof-of-principle was shown, the most important question in this field was: “*Is it feasible to build a radio detector measuring cosmic-ray air-showers with competitive resolution?*” The results of the radio detector deployed on the base of Tunka-133, namely the Tunka Radio Extension (Tunka-Rex) suggests that the answer is “*Yes*”.

Tunka-133 is an air-Čerenkov detector placed in Siberia, nearby Lake Baikal. It consists of an array of photomultipliers, distributed on an area of 3 km². Tunka-133 measures cosmic rays in the energy range of 10¹⁵–10¹⁸ eV starting in 2009. In 2012 it was extended by the radio detector Tunka-Rex consisting of 25 antennas measuring radio emission from air-showers at energies above 10¹⁷ eV.

The present work describes the measurement of radio pulses from air-showers by this detector. The structure of this work can be logically divided into two parts: the development of the theory and methods, and the application of the developed methods on the data measured by Tunka-Rex. The theoretical part describes features of the radio pulses, used for the reconstruction of important air-shower parameters. Taking the features into account, a general parameterization of the amplitude distribution on the surface is given. Finally, the relations between measured amplitudes and air-shower parameters, particularly the energy (E_{pr}) and the shower maximum (X_{max}), are phenomenologically described.

The experimental part explains the application of the developed methods on the measurement data. Since Tunka-Rex consists of a low number of antenna stations and operates in near threshold, the data analysis was optimized for these conditions. As a final step, a cross-check was performed against the existing air-Čerenkov detector measuring the same air-showers.

The chapters of this thesis are ordered in the following way:

- Chapter 2 gives a brief overview of the current status of cosmic rays with focus on air-shower detection. The latest theoretical models of cosmic rays production and propagation are summarized. Modern techniques for air-shower detection are described and compared, including latest achievements.
- Chapter 3 briefly explains the mechanisms of the radio emission from air-showers, the environment for the measurements, and the current status of models. Furthermore, an overview on modern radio experiments is presented in this Chapter.
- Chapter 4 describes the different facilities deployed in the Tunka Valley, and its radio extension Tunka-Rex.
- Chapter 5 describes the features of the lateral distribution of radio amplitudes and their connection to air-shower parameters. A reconstruction method for the primary energy E_{pr} and the atmospheric depth of the shower maximum X_{max} , is developed.
- Chapter 6 applies the developed methods on the data measured by the Tunka-Rex detector and compares the results independently obtained by the Tunka-Rex and Tunka-133 detectors. Based on this comparison the precision of the radio reconstruction of E_{pr} and X_{max} is estimated.

2. Cosmic Rays

The discovery of cosmic rays was made more than hundred years ago [1]. First experiments were performed using detectors in hot-air balloons. Years after, cosmic-ray experiments were performed with satellite detectors measuring primary cosmic rays while orbiting Earth, and ground arrays measuring extensive air-showers produced by high-energy cosmic rays. Extensive air-showers are particle cascades which develop like the ones in calorimeters. In cosmic-ray measurements the Earth atmosphere plays the role of gigantic calorimeter, which produces cascades of billions of particles. Some of them reach the surface and are detected.

During over one hundred years of cosmic-ray research many detection techniques have been developed and implemented. These techniques reached the theoretically predicted energy limits [2, 3], however many issues remain unresolved.

Astroparticle physics is close to answering the core questions, as is particle physics, but both are on the edge of the experimental abilities. These fields need a brand new principle for the conduction of experiments to reach ever higher limits.

2.1. The nature of cosmic rays

The closest source of the particles hitting the Earth is the Sun, which emits flares containing hydrogen and helium nuclei with energies below GeV [4]. This solar plasma is responsible for the modulation of low-energy cosmic rays originating outside of our solar system [5]. Due to their intense flux these cosmic rays can be measured directly using balloon and satellite based detectors up to PeV energies. The measurements have shown that about 85% of the primaries consists of protons, about 10% of helium nuclei, about 2% of electrons, 1-2% are heavy nuclei, and less than 1% are antiparticles (positrons, antiprotons, etc.). The flux of the primary particles is described by the simple power-law of the form

$$\frac{dN}{dE} = (E/\text{GeV})^{-\gamma}, \quad (2.1)$$

where N is the number of the particles, E is the energy, and γ is the slope index starting from about 2.65 at lowest energies and varies with the energy of primary particles.

The chemical composition of low-energy cosmic-ray primaries is shown in Fig. 2.1. The almost uniform behavior of the slope indicates that the acceleration of all low energy cosmic rays proceeds similarly. Based on this idea the mechanism of relativistic shock-front acceleration was developed [6, 7]. Theoretical calculations and different measurements have shown, that shock fronts generated during supernova explosions (so-called, "supernova remnants") are good candidates for such accelerators [8, 9]. Moreover, the estimations have shown that in our galaxy, the Milky Way, the number of supernovae is sufficient to produce the measured flux of cosmic rays at energies below PeV [10].

The situation changes dramatically at higher energies. First of all, cosmic rays with energies higher than PeV cannot be detected directly. Thus, we can measure them only by using air-shower techniques (see Fig. 2.2). These techniques are not able to provide

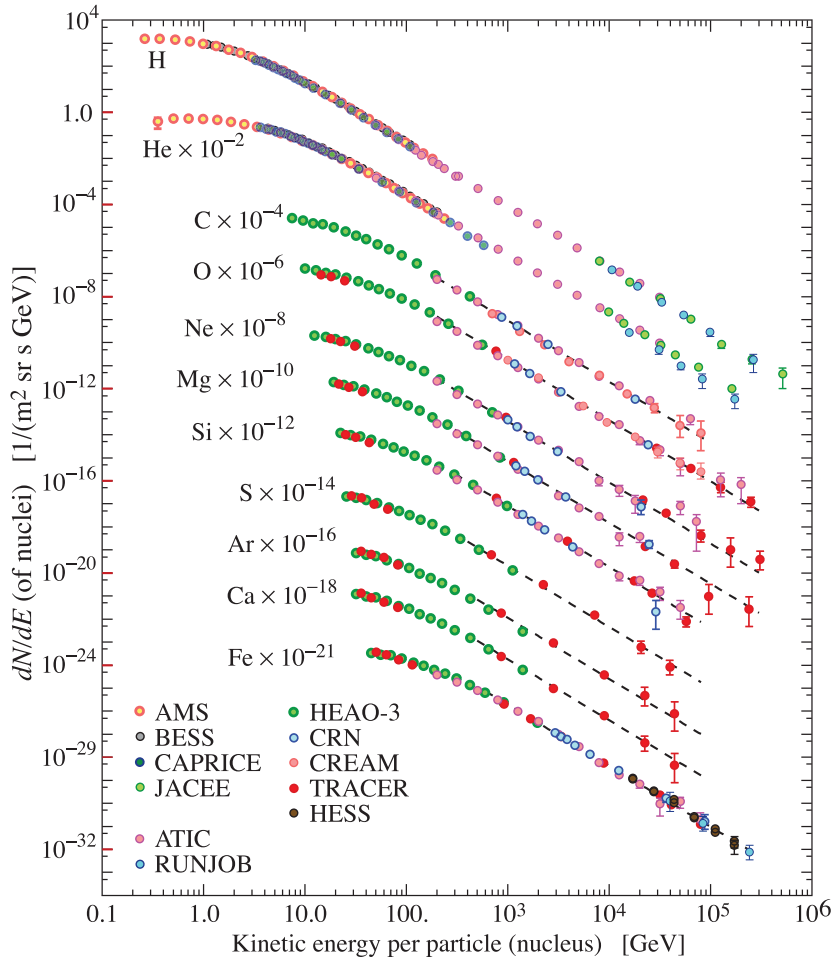


Figure 2.1.: Fluxes of the primaries of low-energy cosmic rays. Colors indicate different experiments. The figure is taken from PDG review [11].

the chemical composition as accurately as direct measurement. Next, the spectral index changes with the energy, and several features appear. Between 10^{15} and 10^{16} eV the index changes from about 2.7 to 3.2: the spectrum becomes steeper. This is the so-called “knee” region. Recent results indicate the existence of at least one “second knee” feature in the range $10^{17} - 3 \cdot 10^{17}$ eV [12, 13, 14, 15]. Then, after $4 \cdot 10^{18}$ eV the spectrum becomes flatter again (“ankle”): slope changes back to about 2.7. The very last cut-off at an energy about 10^{20} eV can be explained either by photodisintegration (the GZK effect [2, 3] is a particular case for proton primaries), or by a maximum rigidity scenario [16].

The energy region after the knee is especially interesting due to changes in the ratio between light and heavy nuclei fluxes. The ratio shifts towards heavier nuclei then back towards lighter nuclei with increasing energy [19, 13, 20, 15]. The more detailed KASCADE-Grande study states that in the region around 10^{17} eV the spectrum of heavy nuclei has a knee structure opposite to the spectrum of a light nuclei, which has an ankle [20]. This could point to a change in particle acceleration mechanisms, i.e. transition to a new type of sources. At energies of about EeV, a transition from galactic to extragalactic cosmic ray sources is expected [21]. Distinguishing between galactic and extragalactic sources

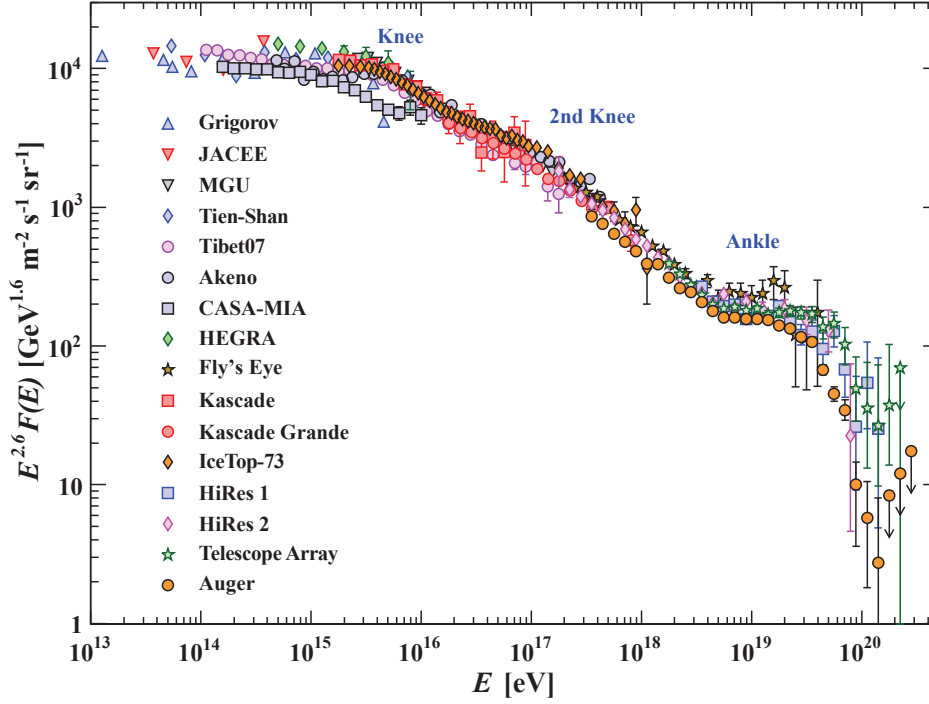


Figure 2.2.: The full particle spectrum measured with various air-shower techniques. Colors indicate different experiments. The figure is taken from PDG review [11].

requires accurate determination of heavy and light nuclei fluxes, as shown by recent composition results from the Pierre Auger Observatory: the dip model for the ankle [22, 23, 24] predicts an almost pure proton composition, which is disfavored by measurements [25].

The resulting maximum energy of an ultra-relativistic cosmic particle is limited by the linear size of the accelerator and the local magnetic field. The simple relation is $E = qBR$, where E is the maximum energy of the particle inside the accelerator, B and R are the magnetic field and extension of the accelerator, respectively. From this relation, Hillas created a plot showing possible accelerators with respect to B and R , which can produce high-energy cosmic rays [18]. Another important aspect are radiative losses during propagation. Taking them into account, the Hillas plot was recently updated [17]. The main result is shown in Fig. 2.3: one can see that restrictions for proton and iron nuclei slightly differ due to the charge and mass of the particles.

To verify models describing the transition from galactic to extragalactic cosmic rays, and the end of the spectra, a high sensitivity to mass composition is required, as well as good statistics. To achieve both, it is necessary to develop a new technique or a hybrid method for air-shower detection with close to 100% duty cycle, low cost and a high composition resolution.

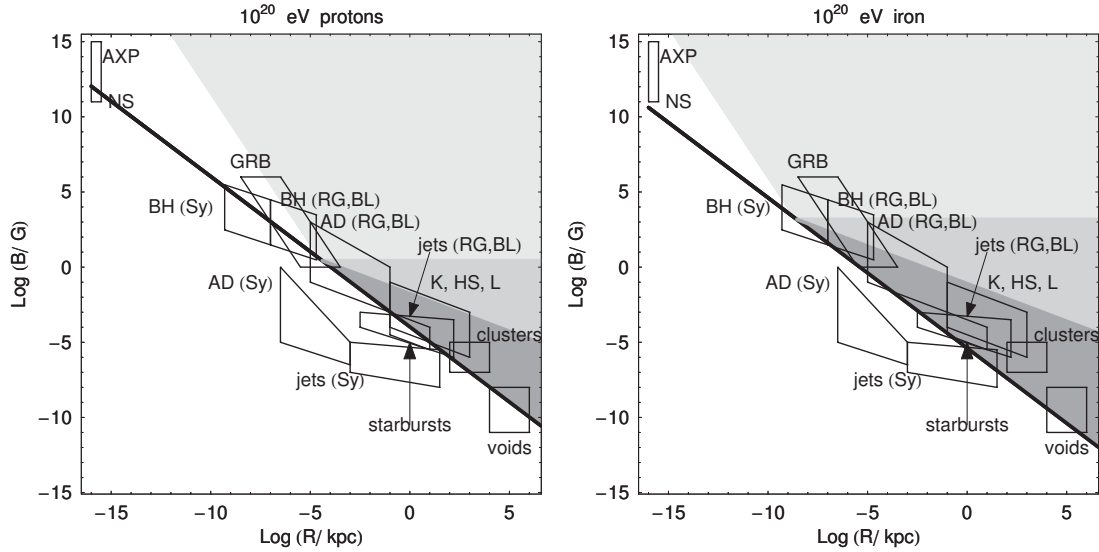


Figure 2.3.: Updated Hillas plot taken from Ref. [17]. Bold line shows the upper limit for the particle energy, given by Hillas [18]. Shaded areas show the exclusion regions given for different acceleration mechanisms with different radiation losses. Left and right plots show the possible accelerators up to 10^{20} eV for proton and iron nuclei, respectively. Due to different charges and masses of the particles, the acceleration and radiation losses differ slightly between particles. The abbreviations used on plot are: *AXP* are anomalous X-ray pulsars and magnetars; *NS* are neutron stars; *BH* are supermassive central black holes of active galactic nuclei; *GRB* are gamma-ray bursts; *AD* are central parsecs of active galaxies. The types of galaxies are given in brackets: *Sy*, *RG* and *BL* are low-power Seyfert galaxies, powerful radio galaxies and blazars, respectively. *K*, *HS*, *L* are knots, hot spots and lobes of powerful active galaxies (*RG* and *BL*), respectively.

2.2. Extensive air-showers

Let us consider the development of extensive air-showers in detail. In the first interaction the primary particle collides with nuclei of the air and produces secondary particles

$$p(^4\text{He}, \dots, ^{56}\text{Fe}) + ^{14}\text{N}(^{16}\text{O}, \dots) \rightarrow p(n) + \pi + K + \text{fragments} + \dots \quad (2.2)$$

The resulting particles, mostly hadrons, neutral and charged pions, continue propagation and produce similar sub-showers. After each interaction the baryons lose about half of the initial energy, and radially deviate from the shower axis in a few meters. Lighter particles (muons, electrons and photons) have larger spread and propagate a larger distance from the shower axis rescattering from atmospheric atoms. The principle interaction scheme of air-shower development is depicted in Fig. 2.4.

In such interactions every hadron can be produced, but heavier hadrons rapidly decay and their fraction is close to zero. This means that only hadrons containing *u* and *d* quarks contribute significantly to the total number of produced particles. Due to large

Gamma quanta produced in π^0 decay intensively interact in the atmosphere and produce electrons and positrons, which, again, can produce gammas. Electromagnetic processes, such as pair production, ionization, Compton scattering and bremsstrahlung take place until a lower threshold interaction energy is reached, at this point particles start to be absorbed. These processes form the electromagnetic component of air-showers including electrons, positrons and gamma quanta. Since these particles are light and stable, they constitute the majority of the total particles produced in air-showers.

A small fraction of the energy is deposited in the air, as Čerenkov or fluorescent light, or emitted during propagation, as radio waves, and can be detected independently of particles from the air-shower.

The air-shower can be described using two important properties: first, the maximum number of particles N_{\max} at the atmospheric depth of the shower maximum X_{\max} . And second, the lateral distribution of particles. The number of particles at deepness X is parameterized by the Gaisser-Hillas function [26]

$$N_{\text{GH}}(X) = N_{\max} \left(\frac{X - X_0}{X_{\max} - X_0} \right)^{\frac{X_{\max} - X_0}{\lambda}} \exp\left(-\frac{X_{\max} - X}{\lambda} \right), \quad (2.6)$$

where X_0 is the point of the first interaction, and λ is the radiation length of the particle. This parameterization describes longitudinal development of the air-shower. The lateral distribution of the charged component is parameterized with the Nishimura-Kamata-Greisen (NKG) function [27, 28]

$$\rho_{\text{NKG}}(r, s) = N_{\text{ch}} C(s) \left(\frac{r}{r_{\text{M}}} \right)^{s-2} \left(1 + \frac{r}{r_{\text{M}}} \right)^{s-4.5}, \quad (2.7)$$

$$C(s) = \frac{1}{2\pi r_{\text{M}}} \frac{\Gamma(4.5 - s)}{\Gamma(s)\Gamma(4.5 - 2s)}, \quad (2.8)$$

where r is the distance to shower axis, s is the shower age, which is determined by the atmospheric depth X with the expression

$$s = \frac{3X/X_0}{X/X_0 + 2X_{\max}/X_0}. \quad (2.9)$$

The other parameters of the NKG parameterization are the Molière radius r_{M} and the number of charged particles N_{ch} with normalization

$$2\pi \int \rho_{\text{NKG}}(r, s) dr = N_{\text{ch}}. \quad (2.10)$$

These parameterizations are used in several analytical models and numerical software packages for the prediction of air-shower behavior under different conditions, as well as for the inverse solution of the air-shower parameters problem: reconstruction of the primary energy and depth of the shower maximum from measured observables. For example, the Gaisser-Hillas parameterization is used in the data analysis of fluorescence telescopes, and the NKG parameterization is used for surface particle detectors. Moreover, these parameterizations are actively used in analytical calculations of the radio signal from extensive air-showers [29].

For indirect determination of the mass composition of the primary cosmic rays statistical approaches are used: one measures the mean of the shower maximum and its standard

deviation. Light particle primaries penetrate deeper in the atmosphere and have a steeper lateral distribution compared to heavy nuclei. Another method uses the measurement of the ratio of the electromagnetic and muonic components, which is sensitive to the type of primary particle: air-showers of heavy nuclei feature more muons.

2.3. Air-shower detection techniques

The present work is focused on the detection of high-energy cosmic rays, thus only air-shower detection techniques are overviewed. A comparison chart of different techniques is given in Table 2.1. Modern satellite experiments measuring directly low-energy primary cosmic rays are described in Refs. [30, 31].

2.3.1. Particle detectors

Surface particle detectors are the oldest technique applied for air-shower detection. They detect the muonic and electromagnetic (electrons and gamma) shower components reaching Earth's surface. The particles can be detected with water-Čerenkov devices by measuring Čerenkov light emitted by water as an energetic particle passes through, or using more compact scintillators. The main advantages of such techniques are the simple and stable construction and the around-the-clock duty cycle. Moreover, the only way to measure the muonic component of air-showers. However, this technique does not provide the full information of an air-shower, it measures only the portion of the air-shower front reaching the surface, i.e. surface particle detectors have limited sensitivity to the shower maximum. Furthermore, the interpretation of the measurement strongly depend on hadronic models used for the prediction of the particle ratios. The sensitivity to the chemical composition of the primary cosmic rays can be improved by e/μ separation, as shown by the KASCADE-Grande experiment [32]. The largest particle detector covering 3000 km² is deployed at the Pierre Auger Observatory [33]. Since 40 years, particle detectors are used not only for cosmic-ray detection, but also for high-energy gamma-astronomy [34, 35].

2.3.2. Imaging techniques

The most precise techniques for air-shower detection are imaging telescopes of two different types: fluorescence and air-Čerenkov. The principle idea of such telescopes is the narrow-angle imaging of a defined part of sky using mirrors to focus light into cameras. The fluorescence telescopes measure light emitted during nitrogen-molecules relaxation, while the air-shower develops in the atmosphere. Detailed descriptions of present fluorescence detectors can be found in Refs. [37, 38]. The other technique, imaging air-Čerenkov, is based on the detection of Čerenkov light emitted by the air when superluminal electrons and positrons propagate through. Since this technique has the lower threshold and can distinguish electromagnetic from hadronic cascades, it is used for TeV gamma detection. More information about modern telescopes is given in Refs. [39, 40]. The advantages of the imaging techniques are the very high precision and direct measurement of the cascade development. To reach such precision, the telescope has to be accurately calibrated and the atmosphere has to be monitored during measurements. The main disadvantage of these techniques is the low duty cycle as the telescopes can operate only during moonless nights with clear atmosphere.

Table 2.1.: Comparison chart of air-shower detection techniques

Detector type	E_{th} (eV)	ΔE_{pr} (eV)	ΔX_{max} (g/cm ²)	Duty cycle	Cost ¹
Particles	$\approx 10^{12}$	$\approx 20\%$	$\log A(N_e, N_\mu)$ ²	$\approx 100\%$	Medium
Fluorescence	$\approx 10^{17}$	$\approx 15\%$	≈ 20	$< 15\%$	High
Imaging air-Č.	$\approx 10^{12}$	$\approx 10\%$	γ/hadron ³	$< 15\%$	High
Non-imaging air-Č.	$\approx 10^{15}$	$\approx 15\%$	≈ 25	$< 15\%$	Medium
Space ⁴	$\approx 10^{19}$	$\approx 20\%$	≈ 100	$> 15\%$	Ultra high
Radio ⁵	$\approx 10^{17}$	$\approx 15\%$	≈ 40	$\approx 100\%$	Low

¹Relative cost including hardware and maintenance.

²Particle detectors are less sensitive to the shower maximum (the best resolution of about 50 g/cm² was reported for very-high-energy events by the Pierre Auger Collaboration [36]). The mass composition is mainly reconstructed using the number of electrons and muons.

³Imaging air-Čerenkov detectors are suited for gamma detection, the reconstruction is tuned for gamma/hadron separation.

⁴Planned properties of air-fluorescent experiment.

⁵Resolution of the Tunka-Rex experiment.

2.3.3. Non-imaging techniques

Non-imaging techniques imply wide-angle measurements of electromagnetic (air-Čerenkov, radio, etc.) emission emitted during the air-shower development. The main difference from imaging techniques is that non-imaging ones can cover the entire sky, but measure only a footprint mapping the integrated emission of an air-shower, therefore the reconstruction of the air-shower must be performed indirectly. Nevertheless, non-imaging techniques can achieve a precision competitive to imaging ones. Modern air-Čerenkov experiments are described in Refs. [41, 42, 43, 44]. An overview of modern radio experiments is given in Chapter 3.3.

2.3.4. Satellites for air-showers

The alternative to surface detection is monitoring of the atmosphere from above: a satellite measuring fluorescence light produced in air by ultra-high energy ($> 10^{19}$ eV) cosmic rays. Currently there are three planned experiments: TUS [45] placed on-board of the Lomonosov satellite, KLYPVE [46] and JEM-EUSO [47] placed on-board the ISS. Unfortunately, due to technical and political reasons, the launch of these experiments has been postponed.

2.3.5. Radio detection

The radio technique for the detection of air-showers was tested more than 50 years ago [48] and brought back to life only in the last decade. It is a non-imaging technique for the detection of radio flashes from air-showers with primary energies greater than 10^{17} eV. Main advantages of this technique include a relative high sensitivity to the shower maximum, a calorimetric measurement of the energy of the electromagnetic component and almost 100% duty cycle. A more detailed description is given in the next Chapter.

3. Radio emission from extensive air showers

Pioneer works related to the radio emission from air-showers were performed in the 1960s. The major contribution to the radio power, namely the geomagnetic deflection of charged particles, was described in the fundamental work by Kahn and Lerche [49]. The second important mechanism, the variation of the charge excess, was described by Askaryan [50]. In the same decade, radio emission from air-showers was discovered [48] and a number of experiments were conducted (see Chapter 3.3). Fruitful results were obtained by Allan performing measurements in Haverah Park, England [51]. The lateral distribution of radio amplitudes was parameterized with a simple exponential function, and the sensitivity of the measured amplitude to the energy of the primary particle was proven.

In spite of the success in qualitative understanding and in quantitative measuring of the radio signals of extensive air-showers, this technique was almost forgotten until the first decade of the next century. The radio technique was disregarded for simple practical reasons: at that time particle detectors satisfied the needs of cosmic-ray physics, and new fluorescence technique was more successful than radio. Other critical arguments were the relatively small footprint of the radio signal and atmospheric background from thunderstorms. Acquiring and analyzing radio data requires very accurate treatment of the background, antenna patterns and spectral transformations, which, in turn, require digital processing and computing power. Due to these factors, radio detection of cosmic rays was non-competitive without modern electronics.

In the 2000-10s the situation reversed. The classical detection techniques began to reach their economical limits. Additionally, success in electronics and digitalization enabled a real-time acquisition of the radio data with very high time resolution. These factors inspired a renewed interest to the radio detection of cosmic rays.

A first generation of digital radio experiments [52, 53] has proven that radio emission from air-shower can be detected and analyzed starting from a threshold of 0.1 EeV. They have shown already that the precision of the energy reconstruction can be better than 20%. Meanwhile, the main emission models have been implemented in a number of simulation codes working together with air-shower simulation software [54, 55, 56]. Several methods of air-shower reconstruction have been developed base on these simulations. In the present Chapter a brief overview of the radio emission mechanisms are given, their properties and the current status of experimental detection of air-showers using the radio technique are discussed.

3.1. Emission mechanisms

Electrons and positrons are the main charged component of extensive air-showers, the radio emission from air-showers is connected to these particles. Radio emission in this case can be calculated in the framework of classical field theory [57]. An interesting question arises from the conditions at which electrons (or surrounding medium) start to emit. For convenience, the emission processes are divided in groups according to the nature of the emission, although most of them is experimentally confirmed to be of relevant strength:

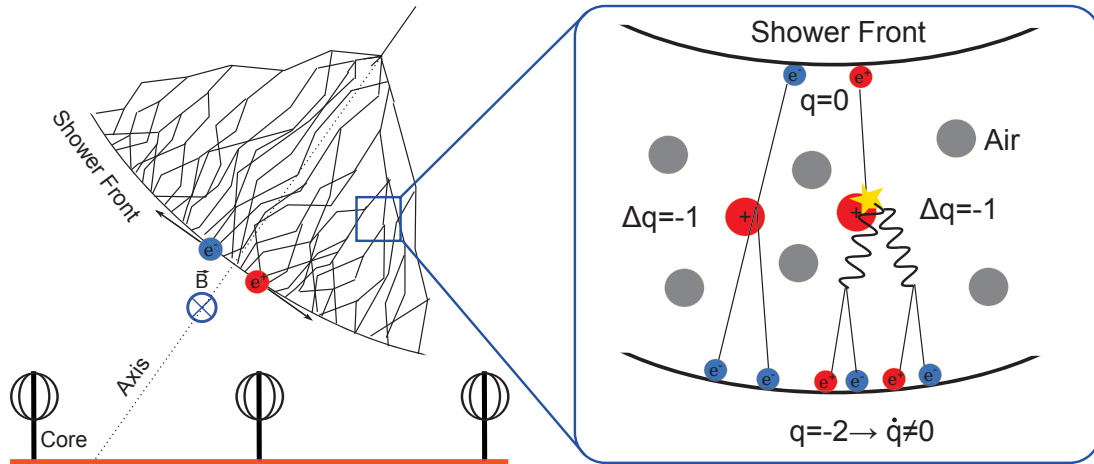


Figure 3.1.: Schematic representation of the main contributions to the radio emission from air-showers (by R. Hiller)

Left: Geomagnetic effect. A current produced by deflection of electrons and positrons emits a radio signal polarized perpendicularly to the magnetic field and shower axis [49].

Right: Askaryan effect. Variation of the net current leads to a changing electrical potential, which produces radially polarized radio emission [50].

emission due to the magnetic field of the Earth (geomagnetic) [49, 58, 59], the acceleration in electrical fields of the atmosphere [60] and the variation of the net charge [50]. Note that there are also some pure quantum phenomena, which could also cause radio emission: radio-Čerenkov [61], transition radiation [62, 63] and molecular bremsstrahlung [64]. The latter was suggested as the main reason for high frequency (in GHz range) emission initiated by air-shower, but the CROME experiment has shown that this is not true [65].

The present work is focused only on the dominant mechanisms of the radio emission from extensive air showers, which are experimentally confirmed: transverse currents [49] and Askaryan (charge excess) effect [50]. The first effect is caused by the deflection of electrons and positrons in the magnetic field of Earth (under Lorentz force). It creates a current in the direction perpendicular to the magnetic field and shower axis. Due to this geometric constraint, the emission is linearly polarized along the axis defined by the vector product of the magnetic field and shower axis. The second effect (charge excess) appears due to ionization of the air and annihilation of positrons. It leads to changing absolute values of positive and negative charges, and consequently, changing potential of the electrical field. The radio emission is polarized in the direction of the shower axis, like for the Čerenkov emission. A schematic representation of those mechanisms is given in Fig. 3.1. In Fig 3.2 one can see the visualization of the components of electrical field obtained with CoREAS simulations.

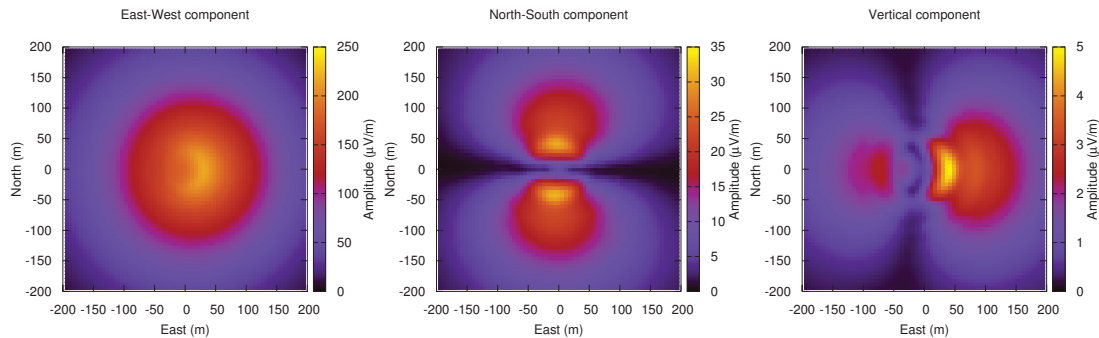


Figure 3.2.: Lateral distribution of components of the electrical field induced by an air-shower on the surface of the detector. The obtained distributions are for a vertical air-shower with geomagnetic field directed to North.

Left: East-West component of radio emission obtained as a sum of geomagnetic contribution and Askaryan effect.

Middle: North-South component of radio emission proportional to the Askaryan contribution normalized by sine of azimuth (since the polarization is directed to shower axis).

Right: Vertical component of radio emission. This effect is visible only on a percent level and usually neglected. The existence of such contribution is qualitatively explained by a non-planar shower front (opening angle of $1-2^\circ$) and its thickness (few meters).

3.2. Models

Since the generation of the radio emission from extensive air-showers is mostly described by classical electrodynamics, the calculation task can be separated from the problem of particle production in the air-shower cascade and solved independently. In other words, to obtain the radio pulse at some location, it is only required to know the propagation of the charged component during the air-shower development. In all modern models the propagation of charged component is taken from air-shower simulation software, such as CORSIKA [66] and Aires [67]. Hence, the calculation comes to the computation of Liénard-Wiechert potentials. One can do this in a straight-forward way, microscopically, by computation of the emission from single particles, or macroscopically from computation of the emission from effective currents.

The macroscopic approach is developed in MGMR [29] and implemented in the EVA simulation software [56], which takes the distribution of charged particles from CONEX [68]. Another macroscopic model was developed in MSU [69]. Of course, the macroscopic approach looks more elegant, but requires fine tuning and introduction of additional parameters. Moreover, the geomagnetic effect and the charge excess are treated separately. On the other side, the microscopic approach requires more computation time and does not allow for separation between emission mechanisms, but it contains almost no free parameters (only the atmosphere is introduced manually) and provides more realistic results.

The microscopic approach is represented in two models: ZHS [70] and the end-point formalism [71]. The ZHS model is implemented in the software ZHAires, in which the trajectories of charged particles are taken from Aires [55]. The end-point formalism is

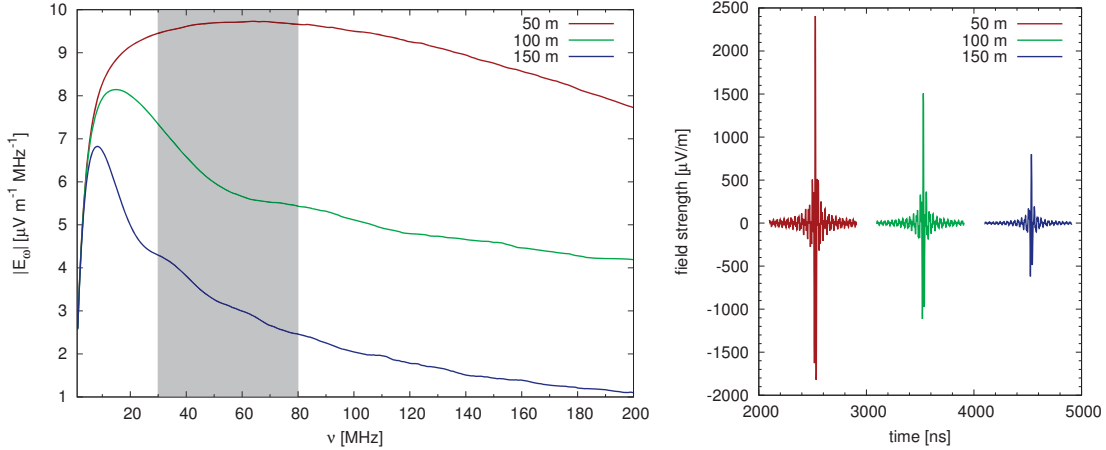


Figure 3.3.: Radio emission from vertical air-shower with primary energy of 1 EeV simulated with CoREAS.

Left: Spectra of radio signals for different observers: 50 m, 100 m and 150 m from the shower axis. One can see, that the maximum power is in the range of tens of MHz. The shaded area indicates the band commonly used by experiments in the MHz frequency range (including Tunka-Rex). The band lower than 30 MHz is disfavored, because of high background (see next section).

Right: Signal obtained from these spectra after rectangular 30-80 MHz filter (shaded area on left side).

implemented in the CoREAS software [54], in which the trajectories of charged particles are taken from CORSIKA. The CoREAS software was developed at KIT, which is the main reason why it was chosen for the present work. Furthermore, it was shown, that CoREAS simulations are in agreement with measured data [72]. Sample signals simulated with CoREAS are given in Fig. 3.3. The comparison of microscopic approaches and their implementations has shown that both formalisms converge to each other [73, 74].

3.3. Detection of the radio emission from air showers

The present section focuses on modern experiments. For pioneer experiments please see references given in this paragraph. First measurements of the radio emission from cosmic-ray air-showers were made by Jelley et al. [48] at Jodrell Bank, England. The main features of the radio emission were experimentally obtained by Allan et al. [51] at Haverah Park facility. There were also several other experiments conducted in the 60s of the 20th century: in Russia [75], Ireland [76], Bolivia [77] and Canada [78].

3.3.1. Modern experiments

All of the modern experiments use fast digital data acquisition, and most of them still rely on particle or optical detectors for trigger and cross-check. There are a several prototypes of self-triggered arrays (see, for example [79]), but they show bad purity and require sophisticated analysis and expensive electronics.

- **LOPES** The LOFAR Prototype Station (LOPES) was a digital experiment measuring radio emission from cosmic rays. It was operated in the years 2003-2013 as extension of the KASCADE particle array [80]. LOPES implements the idea of digital interferometry: knowing the arrival direction of an air-shower, the signal can be reconstructed using beam-forming technology. LOPES has shown the feasibility of interferometric detection in a radio-loud environment. Together with KASCADE, it has proven that radio has sufficient precision for the primary energy reconstruction (around 20%). Additionally, analysis of radio signals show sensitivity of the slope of lateral distribution to the position of the shower maximum [81, 82].
- **CODALEMA** An experiment operating in France since 2002 [83]. Similar to LOPES, it has shown the possibility of the detection of air-showers using digital radio technique, it also demonstrated good sensitivity to the primary energy. CODALEMA consists of several different instruments, one of them is evaluating the self-triggering possibility for radio arrays [84].
- **LOFAR** The LOw-Frequency ARray is a phased astronomical instrument performing radio measurement in the frequency band of 10-240 MHz [85]. This array is distributed over Europe, and has the main scientific aim of radio-astronomical observations. The core of LOFAR is placed in Netherlands and includes a particle detection array, measuring cosmic rays. Triggered by this particle array, LOFAR detects radio emission from air-showers [86]. Exploiting the density of the array, LOFAR has experimentally studied many features of the radio emission from air-showers with high accuracy, particularly, the lateral distribution [87] and polarization [88]. However, its results cannot be independently cross-checked due to the absence of a sophisticated array exploiting another technique of air-shower detection.
- **AERA** The Auger Engineering Radio Array is the largest radio detector for cosmic rays deployed at the Pierre Auger Observatory [89]. AERA checks the possibility of the radio detection of air-showers created by particles with $E_{pr} > 10^{17.5}$ eV. The latest results of the array are the determination of the contribution of the charge excess to the total amplitude [90] and the estimation of the resolution for the reconstructed primary energy (about 17%) [91].
- **Yakutsk** Radio detection of cosmic rays at the Yakutsk observatory has been performed in the years 1987-1989 and started again in 2009. Cosmic rays are jointly measured with the air-Čerenkov array [92]. Using simple methods of air-shower reconstruction, they reported a correlation between averaged shower maxima given by radio and air-Čerenkov setups [93], and give average estimations for the mass composition [94].
- **Tunka-Rex** Tunka-Rex, as AERA and LOFAR, is a second-generation digital array operating in the Tunka Valley [72]. It uses the trigger from the air-Čerenkov array Tunka-133 and consists of simple loop antennas with separation distance of about 200 m. The main technical goal of Tunka-Rex is to prove that such low-cost sparse arrays are feasible for high-energy air-showers detection, and the main physics goal is the cross-check between the radio and air-Čerenkov techniques.
- **SKA** The Square Kilometre Array will be commissioned in the 2020s [95]. This planned electrically dense array consisting of thousands of antennas for radio as-

tronomy operating in broad frequency band. Of course, such a powerful instrument can be also exploited for the purpose of cosmic-ray detection [96], particularly, for radiotomography of air-showers: the simple calculations, presented in Section 5.1.1, show, that the differential structure of air-showers can be deconvolved with a sufficiently dense array and high resolution of the measured frequency spectrum.

3.3.2. Neutrino detection

In addition to a cosmic-ray particle, a neutrino can also induce a nuclear cascade via vector Z^0/W^\pm currents (or through τ -lepton decay, if it is a ν_τ). Having sufficient energy, this cascade produces an air-shower, which can be detected using standard air-shower techniques, but scanning vertical or upward directions. The present Section gives an overview of modern radio experiments focused on neutrino detection.

- **TREND** The Tianshan Radio Experiment for Neutrino Detection is an array consisting of 80 antennas distributed over an area of 4 km^2 [97]. Its main goal is the detection of ultra-high energy neutrinos using a self-triggering technique. Although it is placed in a radio-quiet environment, this technique does not yet allow for detection of air-showers with high purity, which is important for neutrino detection.
- **ANITA** The Antarctic Impulsive Transient Antenna is a balloon borne radio interferometer [98]. It is designed to measure high frequency (200-1200 MHz) radio emission from the cascades created in ice in an effective target volume greater than 10^6 km^3 . Until now it has set only upper limits for the neutrino flux [99] and detected few ultra-high energy cosmic rays [100].
- **Underground detection at the South Pole** The investigation of possible radio detection underground at IceCube started in 1999. The prototype RICE detector was taking data until 2010, but has seen no evidence of high-energy neutrinos [101]. Nowadays, there are different experiments exploiting the same idea [102, 103, 104, 105, 106]. Recently, a new, phased radio array was proposed for IceCube [107].
- **TAROG** Taiwan Astroparticle Radiowave Observatory for Geo-synchrotron Emissions is a new detector for detection of ultra-high energy cascades induced by cosmic rays and neutrinos, including tau [108]. The prototype array consisting of 12 LPDAs with band of 110-300 MHz was deployed in 2014.

3.3.3. Radar methods for the detection of high-energy particles

Measuring the radio echo from high-energy air-showers was suggested more than 70 years ago [109]. Recently, this idea was revisited in a number of works [110, 111]. Still, there is no experimental detection of radar signal re-scattered on air-shower plasma. The Telescope Array RADar (TARA) [112] gives only upper limits for this technique [112]. Furthermore, there is theoretical work criticizing the feasibility of radar detection [113].

However, there are estimations for radar detection of high-energy neutrinos in ice [114]. Ice is not transparent for radio waves, but provided sufficient power, radio waves penetrate on a distance of hundreds of meters. Thus, this technique could be tested in Antarctica at the IceCube experiment [115]. Let us note, that water itself has a very short attenuation length (less than few meters for MHz range), and such techniques can not be used in

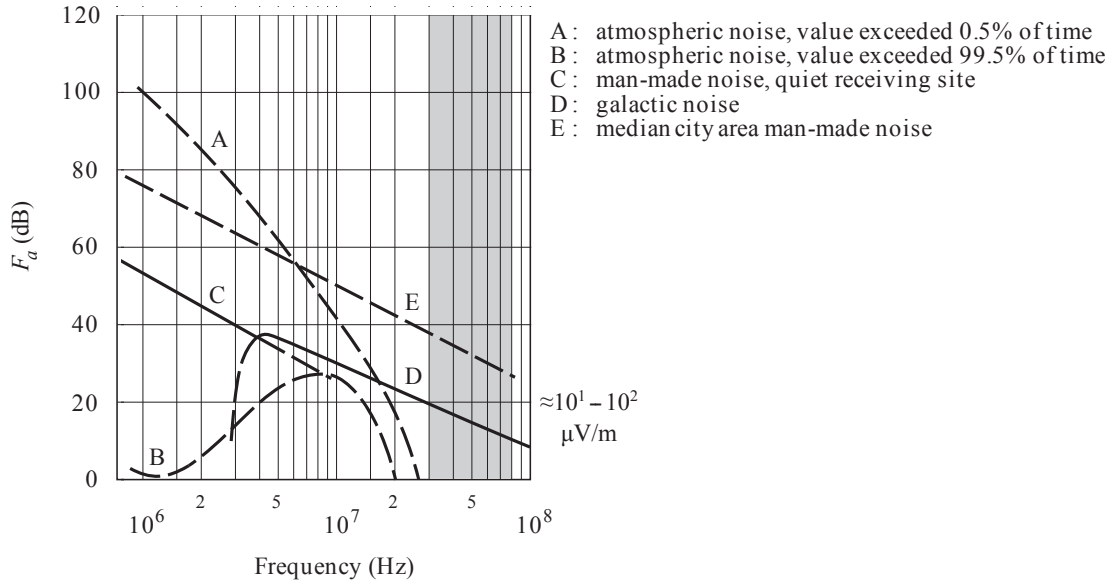


Figure 3.4.: Sources of radio background at MHz frequencies taken from Ref. [118]. The shaded area is the bandwidth of the Tunka-Rex detector. Since Tunka-Rex is placed in a radio-quiet location, the main source of noise is the Galaxy (curve D). Converting noise units into electrical field strength, one obtains values of about $10^1 - 10^2$ $\mu\text{V/m}$ in this band, which corresponds to a threshold for air-shower detection of about 10^{17} eV. The thermal noise at 0°C corresponds to $F_a = 0$ dB, i.e. the bottom line of the plot.

water-bound detectors, like GVD [116]. The feasibility should be carefully estimated for ice-placed experiments due to impurity of ice.

3.3.4. Radio background

In the present Section the typical background for the radio measurements at MHz frequencies is discussed, because they are commonly used in modern experiments. As it can be seen from simulations [117], the main power of the radio emission is in this frequency range of 1-100 MHz with a maximum at tens of MHz. Fig. 3.4 shows that the region below 10 MHz the background is dominated by human-made noise, and above 10 MHz, the main source of noise, in quiet places, is galactic background [118]. Thus, the frequency band from 30 to 80 MHz is a good compromise between radiation power and background. This range is selected by many modern experiments. Higher frequencies are disfavored because of loss of coherence (due to the finite thickness of the air-shower front).

4. Tunka Radio Extension (Tunka-Rex)

Following the great success of the LOPES experiment, a first prototype radio station was installed at Tunka-133 in 2009. First measurements have shown the sensitivity to radio emission from air-showers [119]. Taking into account the geometry of the Tunka-133 host experiment and the background in this environment, the layout of the Tunka-Rex (Tunka Radio Extension) setup was developed, and deployment started in summer 2012.

4.1. Tunka astrophysical facility

The Tunka facility in the Tunka Valley close to Lake Baikal in Siberia has a long history beginning as radio-instruments testing area. The present chapter describes the astrophysical instruments installed there. First investigations began in the 1990s with the air-Čerenkov detector Tunka-13 [120] (later Tunka-25 [121]) consisting of photomultiplier tubes (PMTs) distributed over a square area of 0.1 km^2 (see Fig. 4.1). Later, the modern air-Čerenkov detector Tunka-133 was built [122]. Starting from 2012 several extensions have been deployed. In future all of them will belong to TAIGA, the Tunka Advanced Instrument for cosmic ray physics and Gamma Astronomy [123]. A brief overview on the Čerenkov experiments in the Tunka Valley can be found in Ref. [124].

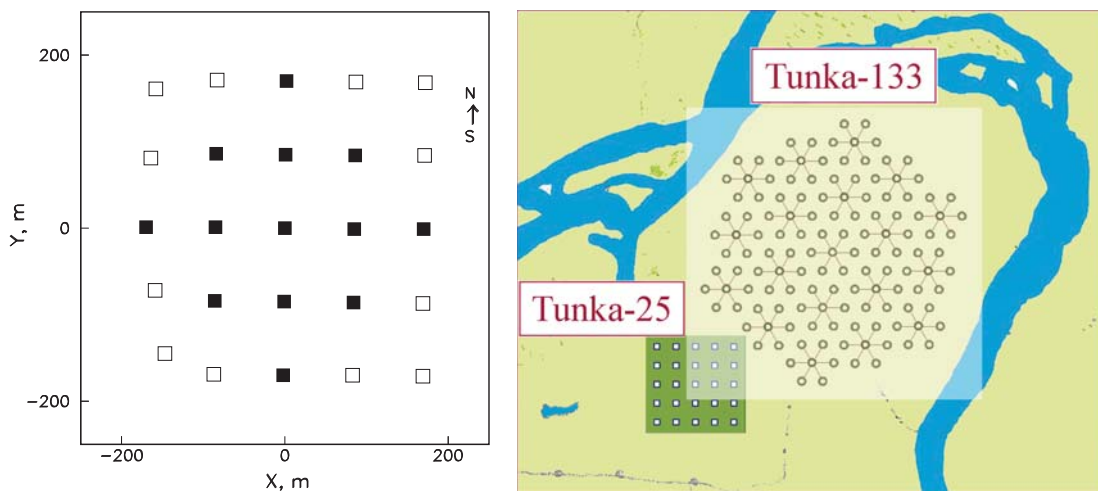


Figure 4.1.: Development stages of the Tunka-133 air-Čerenkov detector.

Left: Tunka-25 detector [121]. Black points are the original Tunka-13 detector [120] triggering Tunka-25.

Right: First stage of the Tunka-133 detector [122] of the year 2009. Six additional satellite clusters were deployed in 2011.



Figure 4.2.: Tunka-133 detector with photomultiplier tube (PMT) inside. Each consists of a large PMT (with diameter of 20 cm) covered by Plexiglas. The distance between detectors is about 80 m.

4.1.1. Tunka-133

Tunka-133 was inaugurated in 2009. It consists of 19 inner clusters, each contains 7 PMTs (see Fig. 4.2) in a hexagonal grid (one in the center). The inner part has a ring structure: one cluster in the center, then seven clusters in the internal ring and twelve clusters in the external ring. The inner part is dense, with a distance between PMTs of 80 m, is covering area of about 1 km². Later the array was extended by six satellite clusters increasing the effective area to 3 km².

Tunka-133 runs during clear moon-less nights from September to April. In summer the array is turned off for maintenance and deployment of new detectors. Thus, the effective time of measurements is about 250-500 hours per year. The array is designed for the energy range from 10¹⁵ to 10¹⁸ eV. The total number of events with $E_{pr} > 10^{17}$ eV is in order of 10³ per year. The precision of the experiment is 15% for the primary energy and 28 g/cm² for the shower maximum [43]. After three years of data acquisition several features in energy and mass composition spectra were found [43], confirming results by other experiments: a hardening at $3 \cdot 10^{16}$ eV and a softening at about 10¹⁷ eV (the second knee).

4.1.2. Tunka-HiSCORE

The Hundred**i* Square-km Cosmic ORigin Explorer (HiSCORE) is a new non-imaging air-Čerenkov instrument for the detection of high-energy gamma rays [125]. Moreover, jointly with Tunka-Rex, the knee and the second knee will be measured with the same technique [126]. The deployment started in 2012, currently about 30 detectors are installed and commissioned [44, 126]. Fig. 4.3 shows a photo of a HiSCORE station. At its final stage the size of the detector will be about 100 km². The sampling rate of Tunka-HiSCORE is significantly larger than one of Tunka-133: 1 GHz versus 200 MHz, i.e. it is interesting for Tunka-Rex to investigate the pulse shape written with such frequency. In addition, it was tested if the radio-beacon technique provides a possibility of direct testing the time resolution of the HiSCORE DAQ (see Appendix A).



Figure 4.3.: HiSCORE station installed at the Tunka facility.

Left: Single station with opened cover. Four Winston cones wrapping PMTs.

Right: General view of the HiSCORE station (left) with electronic box (right).



Figure 4.4.: External and internal view of a Tunka-Grande station.

Left: Tunka-Grande housing with attached Tunka-Rex antenna in front of it.

Middle: Internal view of Tunka-Grande housing: box with electronics, communication lines and on-ground particle detectors.

Right: Underground room of Tunka-Grande station consisting of particle detectors for muons.

4.1.3. Tunka-Grande

Tunka-Grande is one of the extensions recently deployed in the Tunka Valley. It is the one of the most important instruments for performing hybrid detection with Tunka-Rex radio measurements. The scintillator plates for Tunka-Grande came from the former Grande array, the high-energy extension of the KASCADE-Grande particle array [127]. The detector layout has the same structure as the Tunka-Rex array: 19 stations placed nearby the 19 inner Tunka-133 cluster centers. Currently, the core (inner 7 stations) has both electron (on ground) and muon (underground) scintillators installed (see Fig. 4.4). External stations (from 8 to 19) currently have only on-ground detectors, but soon will be also equipped with underground muon detectors. In 2014 the Tunka-Rex array was upgraded with additional 19 antenna stations, each of them connected to the data acquisition of the corresponding Tunka-Grande station. Starting from end of 2015, after commissioning of Tunka-Grande,

the entire Tunka-Rex array (44 antennas) is triggered by the particle array, i.e. enabling measure round-the-clock detection. Preliminary reconstruction of the data acquired with Tunka-Rex jointly with Tunka-Grande will be done at the end of 2015.

4.1.4. Imaging air-Čerenkov telescopes

Finally, for the TAIGA facility, new air-Čerenkov telescopes for high-energy gamma rays are deployed [128]. Together with Tunka-HiSCORE they will study high-energy gamma quanta and search for sources of gamma and cosmic rays. Last, but not least, there are plans for a fluorescence telescope at the Tunka facility.

4.2. Setup of Tunka-Rex

This Section describes the hardware and data acquisition of Tunka-Rex in the configuration of 2012-2014.

4.2.1. Geometry and layout

The present Tunka-Rex layout was determined by the several factors. Since it was planned as an experiment working in a slave mode with Tunka-133 and sharing the common trigger, it exploits free FADC channels at each cluster center. At the time, Tunka-133 had one free slot (i.e. two channels, one channel for each of two antennas per antenna station) at each cluster center. Thus, the maximum number of possible antenna stations is 25 with one antenna station per cluster. The next important consideration for the radio setup is the distance between antenna station and the corresponding cluster center. On the one hand it should be as short as possible to decrease the cost of the cables and reduce cross-talk induced on them. On the other hand, when moving closer to the cluster centers and PMTs, the antennas start to pick up the radio interferences (RFI) from the electronics [129]. Thus, the compromise was to install the antenna stations at distances of about 20 m from any electronics (Tunka-133 cluster centers and PMTs, later Tunka-Grande housing and HiSCORE stations).

Due to technical reasons, not every antenna connected to the Tunka-133 cluster centers was installed in the first deployment, i.e. the development of Tunka-Rex took place in several stages:

- TREX-18 (2012-2013) In the first year, 18 antennas were commissioned. There were two gaps in the internal array: stations 2 and 4 were not deployed, because the FADC channels were occupied by another experiment. Since only a part of FADC boards was installed at the external clusters, only one outer antenna station (23) was taking part in the measurements.
- TREX-25 (2013-2015) In the second year, all antennas connected to Tunka-133 clusters were commissioned and included in the data acquisition.
- TREX-44 (started in 2015) In the deployment of 2014, 19 additional antenna stations, attached to the Tunka-Grande array, were installed. In 2015 the data acquisition was reconfigured in a way, that now all antennas can receive a trigger from the scintillators. In the beginning of 2015 first test measurements were performed, but the entire array started data acquisition in the autumn of 2015.

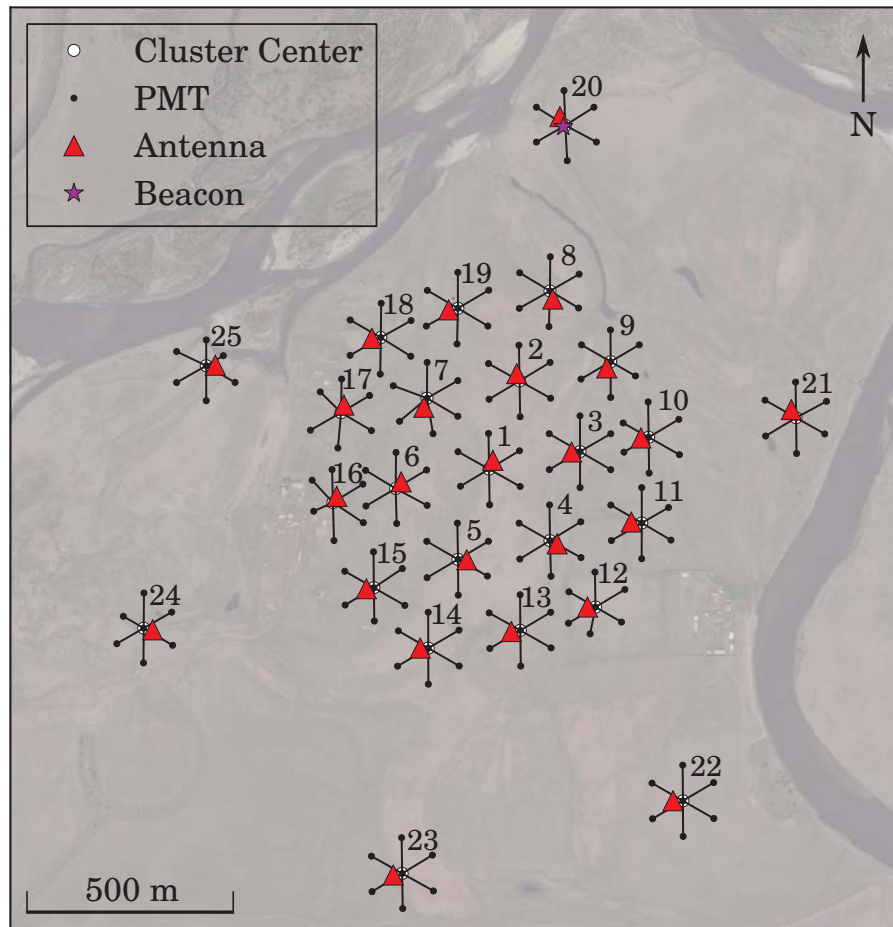


Figure 4.5.: Map of the Tunka facility as of 2013. Triangles show the antenna stations of TRES-25 layout. Antenna stations have the same numbers as the cluster centers of Tunka-133.

- TRES-63 (planned in 2016) The next planned stage of Tunka-Rex is an extension of the array by 19 new antenna stations attached also to Tunka-Grande stations. This means that Tunka-Rex will have a clustered structure with cluster spacing of about 200 m, and each cluster will consist of 3 antennas with spacing of about 30 m. In comparison to radio arrays with regular spacing, Tunka-Rex will measure lateral distributions with higher precision at each point.

Fig. 4.5 shows the layout of TRES-25 in the year 2013. This configuration (one antenna per Tunka-133 cluster) was used for the investigations in the present work. The Tunka-Grande stations are installed in the same grid (one station per cluster), Tunka-HiSCORE will have a regular square grid (not shown).

4.2.2. Hardware properties

Each Tunka-Rex antenna station consists of two orthogonally aligned SALLAs (short aperiodic loaded loop antennas) [130, 131] with 120 cm diameter (Fig. 4.6) mounted on a

wooden pole with a height of about 2.5 m. This height is not optimal in terms of interference between incoming signal and reflection from ground, but saves antennas from the influence of the local fauna (i.e. cows, etc.). Moreover, the sensitivity of the antenna downwards is suppressed by a resistance [130], such that the exact height has only minor influence on the antenna gain. Unlike in most radio experiments, the antennas in Tunka-Rex are not aligned along the north-south and east-west axes, but rotated by 45° , like in LOFAR [85]. At the design stage it was planned to align the antennas in this manner to increase the sensitivity for both polarizations of the radio emission from air-showers, but calculations and measurements have shown that for the Tunka-Rex location and geometry the antenna alignment is not important [132]. The SALLA has been chosen as antenna not only for economic reasons, but also because its properties depend only little on environmental conditions [72], which means lower systematic uncertainties. The antenna arcs are connected at the bottom via a load with impedance of 390 Ohm (from antenna to antenna it varies in the order of 1%). At the top they are connected to a low noise amplifier (LNA). This LNA is connected to a filter-amplifier via 30 m coaxial RG213 cables. A part of these cables are visible at the pole (see Fig. 4.6), the rest are buried underground to decrease the cross-talks between the two cables at one station. For the same purpose they form two loops underground near the pole.

The filter-amplifier is placed inside the electronics box at the cluster center (see Fig. 4.7). It is connected to the Tunka-133 FADC with a short 1 m RG52 cable. The total number of FADC channels is 16 per cluster, two of them are for the antenna station, the rest for the Tunka-133 PMTs (two channels per PMT). The sampling rate of the FADCs are 200 MHz and the length of the trace is 1024 samples with a bit depth of 12 bit (4096 values possible). A schematic presentation of the electronics chain and signal transformation is depicted in Fig. 4.8.

4.2.3. Systematic uncertainties of the setup

The present Section explains the uncertainties of the Tunka-Rex station and summarizes the uncertainties of the Tunka-133 host setup (only high-level uncertainties, i.e. uncertainties of the air-shower reconstruction of Tunka-133; the hardware of it is considered as a black box for this purpose). Only some checks of the Tunka-133 hardware were performed by Tunka-Rex: a FADC amplitude calibration (see Ref. [133]) and a beacon timing analysis.

Since each part of the Tunka-Rex hardware chain has an absolute calibration [72], the entire setup has significant systematic uncertainties due to models, environmental fluctuations and hardware calibration inaccuracies. A small uncertainty comes from the installation inaccuracies: arcs and poles are not ideal, and instruments for the positioning and alignment have some uncertainties. Another uncertainty comes from temperature fluctuations affecting the LNAs: the gain changes with temperature, which varies during measurements by approximately $\pm 20^\circ\text{C}$. The largest uncertainty comes from the absolute scale of amplitude calibration and antenna model uncertainties [72]. Adding all systematic uncertainties the total systematic uncertainty of amplitude measurements at a Tunka-Rex antenna station is 22%. A detailed investigation of each contribution to the total uncertainty is given in Ref. [133].

In the present work it is assumed that the Tunka-133 reconstruction uncertainties are equal for each event. This is a valid assumption since for the later analysis only the high-energy subset of Tunka-133 events was used. Each event of this subset contains many PMTs, i.e. the number of stations varies from event to event change only on the order of 20%. The



Figure 4.6.: A Tunka-Rex antenna station.

Left: Low noise amplifier (LNA) of the Tunka-Rex antenna station. The arcs of the two SALLAs are aligned perpendicularly and connected to the LNA at the top and to load of about 390 Ohm at the bottom (not shown).

Right: Tunka-Rex antenna station in the front of a cluster center electronic box (white box).

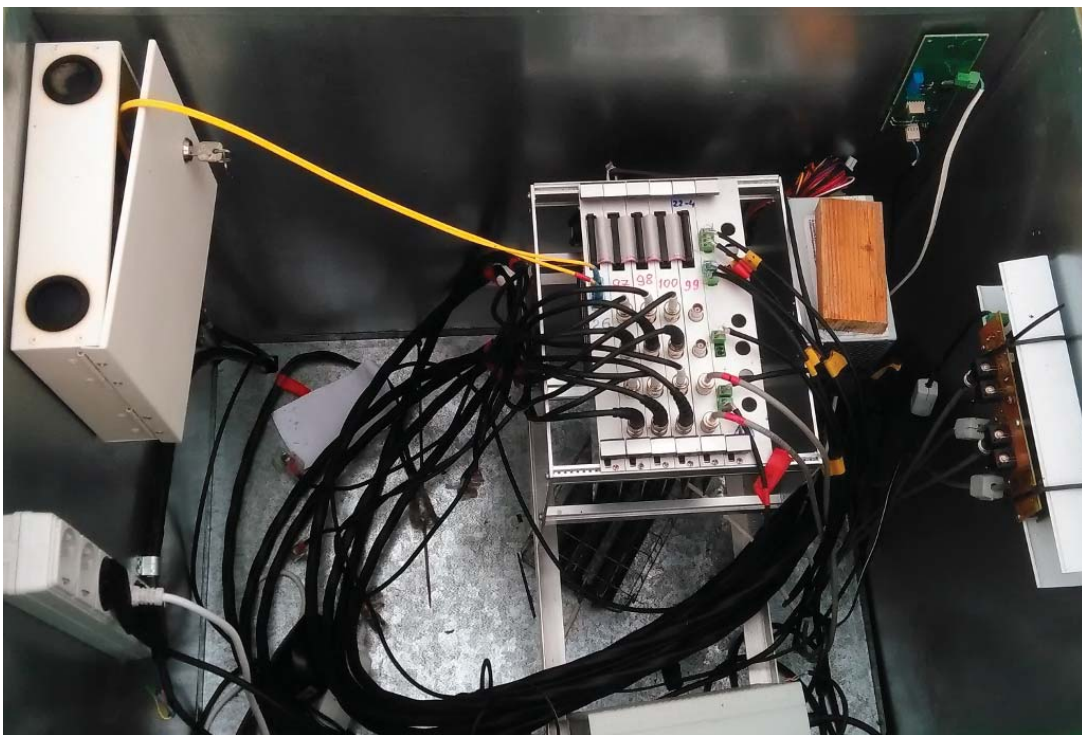


Figure 4.7.: Internal view of Tunka-133 cluster center. FADC boards with 16 channels are placed in the center of the box. Tunka-Rex filter amplifier is attached to the wall (right side) and connected to last channels of FADC.

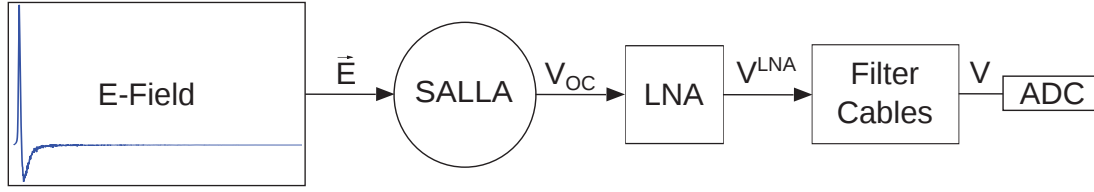


Figure 4.8.: Schematic signal chain of a Tunka-Rex antenna with the corresponding transformations. Each figure represents the transformation of the electromagnetic field. In the selected frequency band (30–80 MHz) the transformations are assumed to be linear. The electrical field of the radio pulse \vec{E} is transformed by the SALLA to an open circuit voltage V_{OC} . Then this voltage is transformed by cables, LNA and filters, and digitized by the FADC with a sampling rate of 200 MHz and a bit depth of 12 bit.

resolution for the events with core outside of the dense array is slightly worse [134], which is also confirmed by Tunka-Rex measurements (see Chapter 6). Table 4.1 summarizes the uncertainties provided by the Tunka-133 collaboration [134].

Table 4.1.: Systematic uncertainties of Tunka-133 [134]. The uncertainties are assumed equal for every high-energy event selected for the cross-check with Tunka-Rex.

Property	Uncertainty
Arrival direction	0.5°
Shower core	5 m
Primary energy	15%
Shower maximum	28 g/cm ²

4.2.4. Signal window determination

Even before obtaining the first list of Tunka-133 events, a simple formula for the signal time window was developed. This formula is based on the knowledge of the cable lengths and hardware properties. The expected arrival time t of the radio signal relative to the trigger time of the PMT signal is

$$t = \frac{N_{FADC}}{2} T_{BW} + \frac{L_R - L_C}{\epsilon c} - \frac{d}{\sqrt{2}c} - \tau \pm \Delta t, \quad (4.1)$$

where $N_{FADC} = 1024$ is the number of FADC records in the trace, $T_{BW} = 5$ ns is the bin width, $L_R \approx 30$ m, $L_C \approx 90$ m are the cable lengths to radio antennas and PMTs respectively, $c \approx 3 \cdot 10^8$ m/s is the speed of light, $\epsilon c \approx (2/3)c$ is the signal velocity in the coaxial cable, $d \approx 80$ m is the typical distance between each cluster center and the surrounding PMTs, $\tau \approx 50$ ns is the PMT signal width and $\Delta t \approx d/(\sqrt{2}c) = 200$ ns is the interval for the radio signal window. The first term in this expression just gives the center of the trace (approximate time of the signal from the third triggered PMT in cluster), the second term is the delay due to the difference in cable length, the third term accounts for possible delays due to the geometry of the detector (for a typical zenith angle of 45°), and the

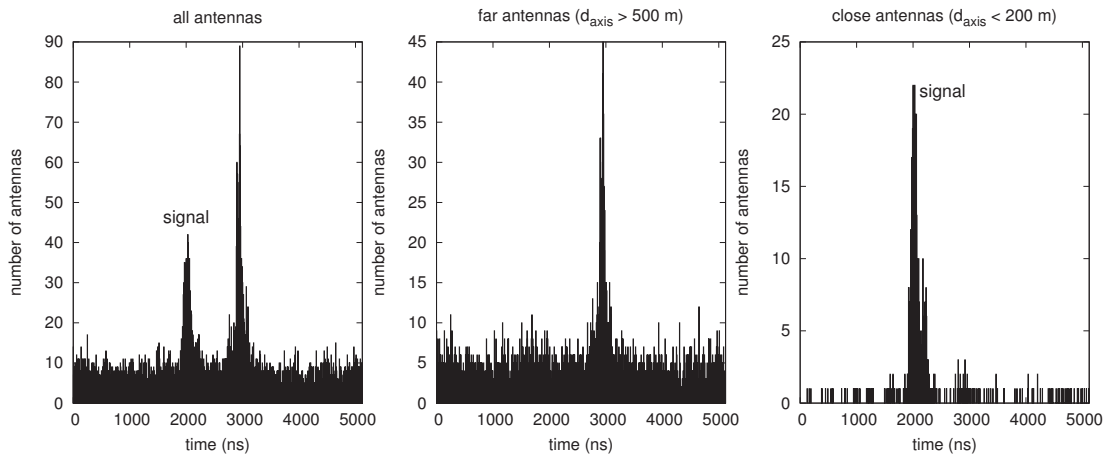


Figure 4.9.: Distributions of peaks in the radio traces (times of maximum amplitude). The distribution was produced using about $\sim 10^4$ high-energy Tunka-133 events (containing about $\sim 10^5$ antenna stations).

Left: Distribution for all antennas. One can see two peaks, one corresponds to the radio signal from air-shower, another is RFI from electronics.

Middle: When selecting antennas far from the shower axis, the first peak disappears, but the second one is still there. This way, one can determine the mean arrival time of background peaks in the traces.

Right: To define the time window for data reconstruction, the closest antennas are selected. An additional small peak appears in the distribution. Its nature is not known, and its treatment is described in Ref. [133]

fourth term describes a possible delay between the shower arrival and trigger times (time of passing an amplitude threshold for the PMTs). Finally, Δt takes into account all possible geometries (for the range of zenith angles from 0° to 70°) of air showers. Thus, the estimated time window of the radio signal is 2000 ± 200 ns. The main uncertainty comes from the Tunka-133 electronics delays, and may have a large impact on the time window. However measurements have confirmed, that this theoretically approximated window is in very good agreement with the final operation window of 2015 ± 135 ns, which was estimated phenomenologically [133].

The phenomenological estimation was performed using the radio traces of the high-energy events. From the radio traces those which have a high probability of radio pulse detection, i.e. traces of antenna stations close to the shower axis, were selected. Using these traces a distribution of the arrival times of the strongest signal was made. Then this distribution was compared with the distribution of traces not containing a radio pulse (for the purpose of rejecting narrow peaks from the electronics, in particular, the trigger). The resulting peak of arrival times was fitted with a normal distribution, and the mean value within three standard deviations was taken as time window, see Fig. 4.9.

4.2.5. Data-acquisition and signal-reconstruction pipeline

Each of the Tunka-133 clusters features its own local DAQ (for an air-shower event a coincidence in at least 3 PMTs of a cluster is required). There, the signal from both, the antennas

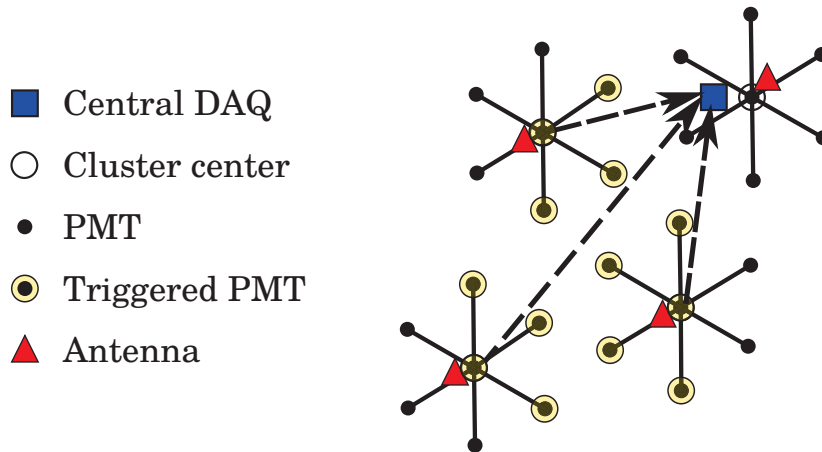


Figure 4.10.: Scheme of the data acquisition of Tunka-133/Tunka-Rex. Each cluster contains a local clock. The time for each single cluster event is calculated as cluster time plus the delay of the optical fiber. We assume that signals from the same air-shower are within a 7000 ns time window corresponding to the time needed by the shower front to cover the entire air-Cherenkov detector.

and the PMTs, are digitized and transmitted to the central DAQ via optical fibers where it is stored on disk (see Fig. 4.10). Then, during the offline analysis, all independent entries from different clusters are merged into hybrid events.

For signal reconstruction Tunka-Rex uses the radio extension of the Offline software framework developed by the Pierre Auger Collaboration [135]. The configuration and module sequence of the standard application are given in Appendix B. Please note, that the designed frequency band for the filter-amplifier is 30–76 MHz, that means before the analysis, measured traces are cut to this band during the first digital Fourier transform. A measured spectrum before processing is shown in Fig. 4.11.

All radio traces are digitally filtered by two types of filters: a narrow-band filter removing frequencies every 5 MHz induced in the coaxial cables connecting the LNA to the cluster center, and a bandstop filter suppressing the band of 30–35 MHz, suffering from background probably coming from the cluster center and induced in the antenna. In summary, the following parts of the spectrum are removed: 30–35 MHz, (35, 40, 45, 50, 55, 60, 65, 70, 75 MHz) ± 1 bin. For narrow-band filtering, one neighboring bin (0.2 MHz) at each side is also removed because of the finite frequency resolution of the spectra (i.e. one frequency can occupy two bins, if it falls between them).

The next step is the reconstruction of the electric field of the antenna station. For this step the arrival direction has to be known in order to apply the antenna pattern. The reconstruction of the arrival direction can be performed independently by the pulse time in every trace (see Fig. 4.12). Using triangulation, it can be done with as few as three antennas. Since with the present reconstruction method using a plane wavefront, Tunka-Rex has poorer angular resolution compared to Tunka-133 ($\approx 2^\circ$ versus $\approx 0.5^\circ$), the angular reconstruction given by the radio detector is used only for quality cuts (see Chapter 6.3). After the transformation of the trace from the FADC counts to the electrical field vector (using the arrival direction of the Tunka-133), the envelope of the signal trace is calculated and its maximum value in the signal window is taken as amplitude of the signal.

The signal-to-noise ratio (SNR) is an important experimental property of the signal. In

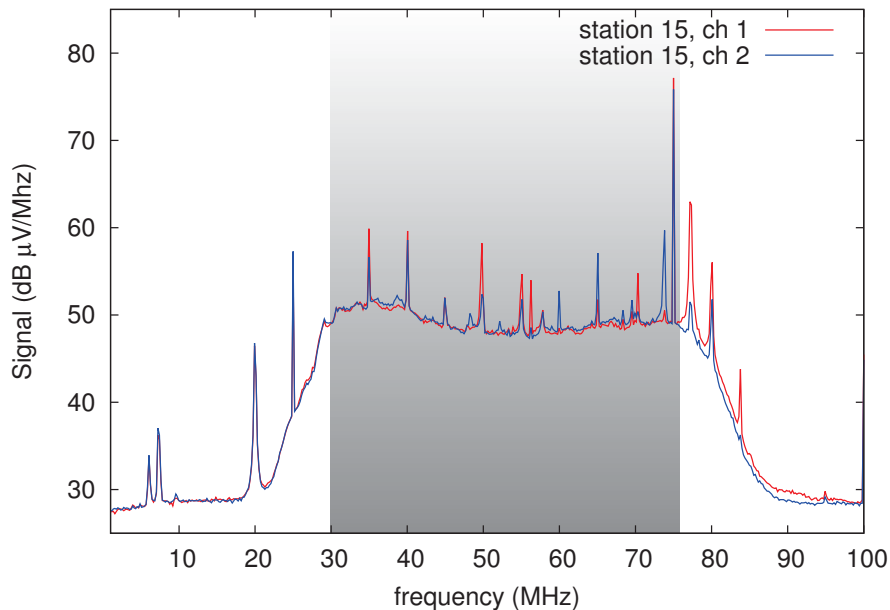


Figure 4.11.: The mean background spectrum in one night of operation, as measured with Tunka-Rex station 15. The shaded area shows the part of the spectrum analyzed digitally, the rest is zeroing during first spectral transformation. One can see narrow peaks each 5 MHz induced on cables (the peak of 75 MHz is the internal clock of the cluster center).

general terms it is defined as ratio (or its square) between measured signal and noise

$$\text{SNR} = \frac{S^2}{N^2}, \quad (4.2)$$

where S is the amplitude of the signal, and N is the amplitude of the noise. The details are in the definition of the signal and noise. For Tunka-Rex it was decided to use the maximum of the envelope within the signal window as signal amplitude S , and the root mean square (RMS) of trace in the noise window as noise amplitude N [72]. This way, a quality cut on the SNR was defined following way: only 5% of the false signals should pass the cut. By phenomenological investigation of the traces, the threshold was defined at the value $\text{SNR}_{\text{th}} = 10$. This is a typical experimental compromise between purity and efficiency. To get rid of artifacts appearing during application of the antenna pattern, the same cut is also applied on the channel level. Knowing the value of the SNR, the average influence of noise on the signal can be estimated and corrected for. Details of this correction are described in Chapter 6.

False positive signals are rejected in two ways. First, using the information of the arrival direction and core position, outliers are removed from the lateral distribution: sorting antennas by the distance to shower axis, after two antennas failing the SNR cut all further antennas are rejected. Then, with the remaining antennas, if more than two are left, the arrival direction is reconstructed and compared with the one reconstructed by the Tunka-133 detector. The difference is required to be less than 5° . This cut was determined from the distribution of angular differences between reconstructions given by both detectors.

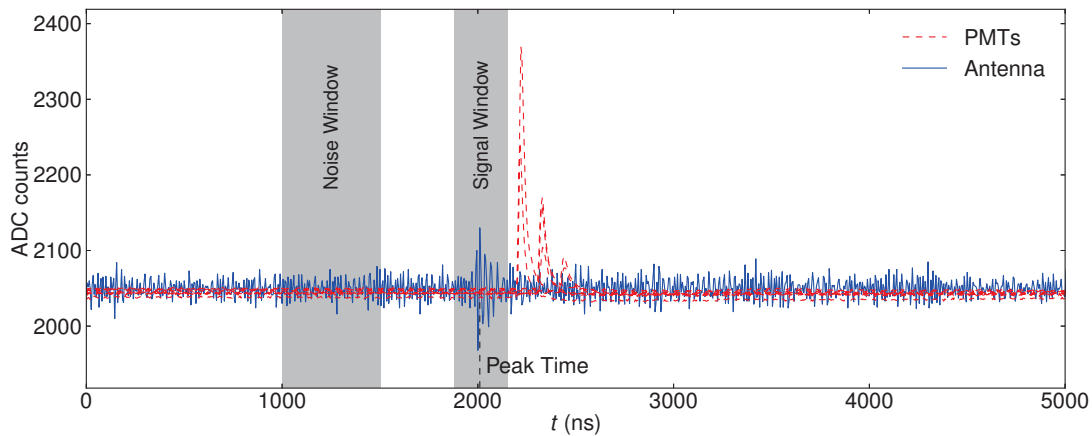


Figure 4.12.: Trace of the radio signal from air-showers before correcting for the antenna pattern. 500 ns from the middle of the trace (left shaded area) are taken for the noise-level estimate. The trace is centered around the third triggered PMT (red dashed lines). This sketch is taken from Ref. [72].

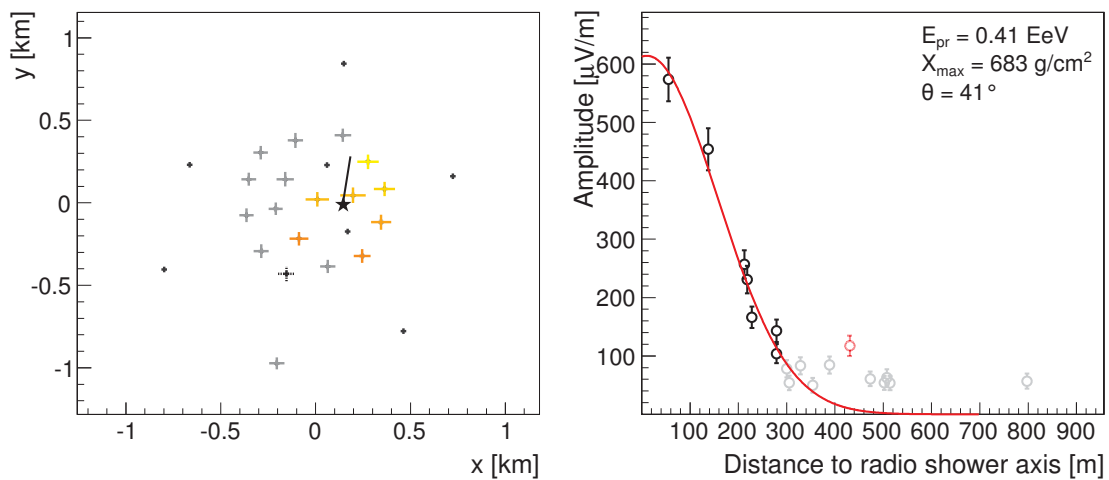


Figure 4.13.: Example event reconstructed by Tunka-Rex.

Left: Footprint of the air-shower. The color code shows the arrival time. Points show clusters without antenna in the 2012/2013 measurement campaigns.

Right: Lateral distribution with fit. Grey points show the antennas not passing the SNR cut, the dotted point is a rejected antenna with false signal.

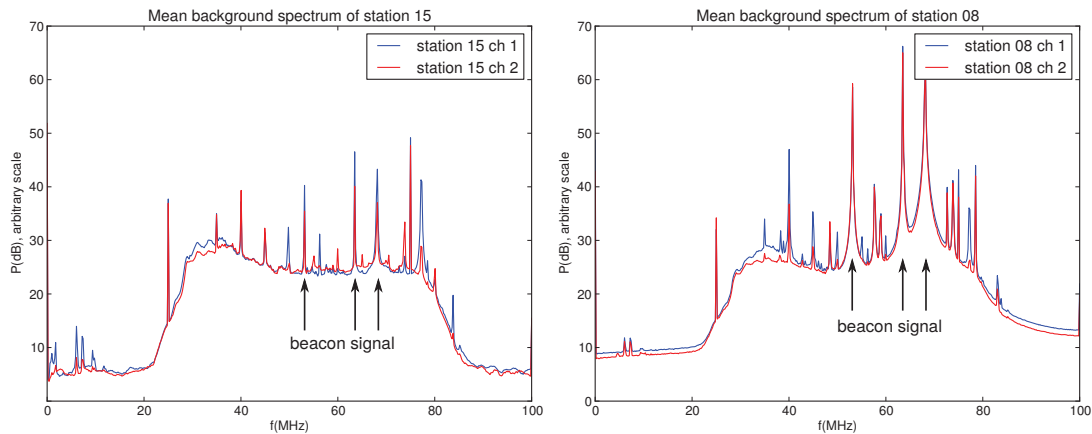


Figure 4.14.: Spectra of Tunka-Rex antennas stations measured with the beacon switched on. The beacon antenna is installed nearby cluster 20. The antenna station installed at this cluster is completely saturated, opposite to the antenna station at satellite cluster 23, which does not see the beacon signal (due to the distance of about 2 km to it). The strength of the beacon signal in the inner part of array also significantly varies with the distance. At distant stations (700 m) the beacon lines is not very high, but well distinguishable (*left*). At the nearest stations (300 m) the beacon saturates the trace (*right*). These spectra show, that permanent measurements with the beacon are not feasible at the moment.

This distribution features a resolution of better than 2° when using a plane wave for reconstruction [72, 133].

The next steps in the event reconstruction pipeline are related to high-level reconstruction. Among these are the fit of the lateral distribution function, the reconstruction of air-shower parameters, and further quality cuts. These steps, the resulting event statistics and the results of the reconstruction are given in Chapter 6. This Chapter described a model-independent event reconstruction later used as input for the high-level reconstruction. The given parameters are hardware-related and obtained with phenomenological approach. An example after all of these steps is presented in Fig. 4.13.

4.2.6. Beacon system

The radio beacon system deployed at the Tunka Valley (in the northern part of the detector, nearby antenna station 20) was originally developed for the LOPES experiment [136]. It consists of an antenna and a sine-wave generator, which emits three frequencies of 51.1, 63.5 and 68.1 MHz. By comparing the phases of these frequencies on receivers with known distances, one can estimate the stability of the timing. Unfortunately, this system can not be exploited with full efficiency due to the following reasons (see example spectra in Fig. 4.14):

- The distance from the beacon to the array should be as large as the diameter of the array, otherwise the nearest antennas will be saturated or far antennas will not see the beacon signal.

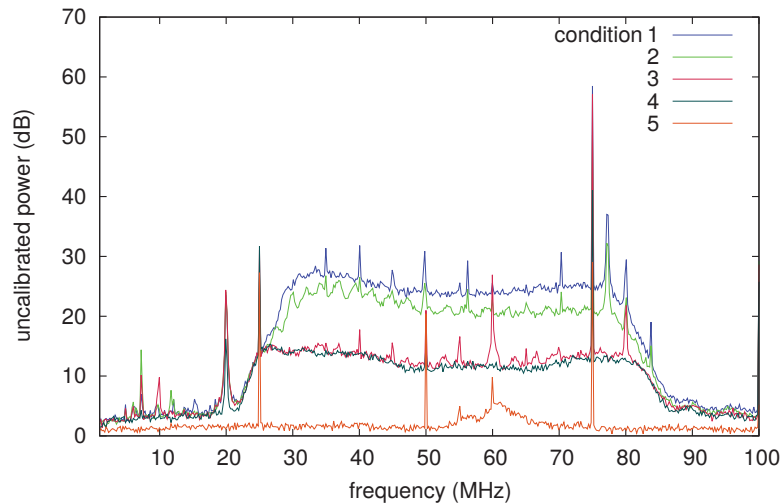


Figure 4.15.: Spectra of background at antenna station 15 measured on January 2013. The measurements were performed in several steps in order to obtain characteristic spectra for several possible conditions of an antenna station.

- 1: Normal condition of an antenna station.
- 2: Antenna station with disconnected arcs (LNA is shortened, but operating).
- 3: Antenna station with disconnected LNA (coaxial cable connecting the LNA with cluster center is starting operates as an antenna, causing narrow peaks in the spectrum).
- 4: Cable connection between LNA and cluster center is broken. e.g. because the connector failed. The behavior is similar to the previous step, but interferences induced in the cable disappeared.
- 5: Filter amplifier is disconnected from the FADC inside the cluster center. Only the internal noise of the FADC board is visible in the spectrum.

- The frequencies were tuned for the LOPES design, and in the Tunka-Rex spectrum they occupy more than one bin (i.e. leakage appears).

Nevertheless, at the beginning of each measurement season the beacon has been sporadically switched on for checking of Tunka-133/Tunka-Rex timing stability. These checks have shown that during each night the timing is stable in the sub-nanosecond order [137]. However, there are jumps in the order of 5-10 ns between nights (due to clock re-initialization) [137].

4.3. Tunka-Rex monitoring and background measurements

Monitoring of the background environment is one of the basic experimental routines, and the Tunka-Rex experiment is no exception. A special software appropriate for hybrid Tunka-133 and Tunka-Rex measurements was developed for this purpose. As the corresponding software for the air-Čerenkov detector, it creates daily reports containing mean and differential spectra of every night. Studying these spectra, a shifter on duty can do hardware diagnostics and fix problems. These problems were systematically studied and classified. As a result, typical spectra characterizing common issues were obtained (see Fig. 4.15). The denoted classification covers almost all of the issues experienced and gives a reliable

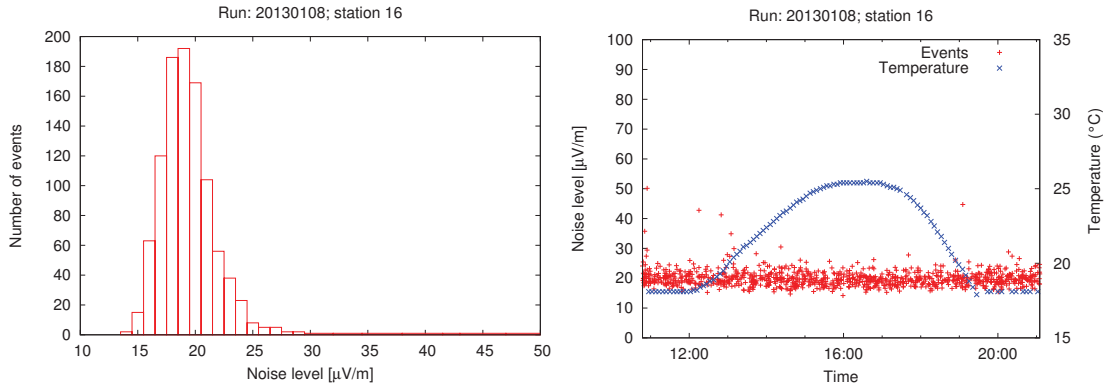


Figure 4.16.: Noise fluctuations and their correlation with the temperature inside the cluster center during a single run (one night).

Left: Distribution of the noise amplitude for all triggered events, which is defined as RMS inside the noise window in the signal trace (see Fig. 4.12). There are no significant features. Other antenna stations show similar distributions.

Right: Variation of the noise amplitude with the internal temperature. A heating controller holds the temperature (blue “x” markers, right scale) within $\approx 15 - 30$ °C: it switches on, when the temperature is lower than 18 °C, and switches off, when it is higher than 25 °C. The noise level (red “+” markers, left scale) is sufficiently stable and does not depend on internal temperature fluctuations.

prediction. On average, about one antenna stations fails per two weeks, and usually can be repaired within a few days.

Another important activity performed in the Tunka Valley in the frame of background investigation was the recording of a noise library. As recording station the antenna at cluster 15 was selected, because it had no specific features in the averaged spectrum. A special trigger of a few Hz was developed in order to get rid of radio or PMT triggering on the background, which causes a possible bias on the measurements. As result, 200 traces per channel were recorded during few minutes. The record was done on 2013.01.17, $\approx 19:00$ local time, the external temperature was about -9 °C¹.

Furthermore, the influence of the temperature inside of the cluster centers was studied. The temperature properties of the LNA and filter-amplifiers are known accurately [72]. However, possible variations of the background with temperature were not previously studied. Heating controllers installed inside each cluster center keep the temperature stable at a level of $\approx 15 - 30$ °C. They do not influence the PMT signal, but for the radio measurements this was not clear since they could emit RFI. Nevertheless, no significant dependence between temperature and internal noise was found (see Fig. 4.16), only occasional RFI appears when heating controllers switch their operation modes. In addition, it was found that the mean background level and its variance are sufficiently stable, so that a constant threshold can be used for the SNR cut.

¹Recorded traces are available on <http://bg.tunkarex.info>

5. Lateral distribution of the radio emission

The lateral distribution of the signals is the one of the main measurables for surface air-shower arrays. Measuring this quantity does not require fast timing or interferometry. At the same time, it gives an almost direct access to air-shower properties, particularly, the primary energy and the shower maximum.

The present Chapter describes the features of the lateral distribution of radio amplitudes at the detector surface. By correcting for special, radio-related features, it is shown, that the radio lateral distribution function (LDF) can be treated as the LDF of the non-imaging air-Čerenkov detector. Moreover, the relation to air-shower parameters is similar for both detectors¹.

5.1. Introduction

To perform calculations in an invariant way, let us introduce the so-called geomagnetic coordinate system, a special version of shower coordinates. The outstanding feature of this system is that the electrical field vector has only two non-zero projections to the axes, the third projection is always close to zero. The basis of this coordinate system takes the form

$$\hat{\mathbf{e}}_x = \hat{\mathbf{V}} \times \hat{\mathbf{B}}, \quad (5.1)$$

$$\hat{\mathbf{e}}_y = \hat{\mathbf{V}} \times (\hat{\mathbf{V}} \times \hat{\mathbf{B}}), \quad (5.2)$$

$$\hat{\mathbf{e}}_z = \hat{\mathbf{V}}, \quad (5.3)$$

where \mathbf{V} and \mathbf{B} are the shower axis and the Earth magnetic field (a hat over a vector denotes a unit vector: $\hat{\mathbf{B}} = \mathbf{B}/|\mathbf{B}|$), respectively. Let us also define useful angles: the geomagnetic angle between shower axis and magnetic field $\alpha_g = \angle(\mathbf{V}, \mathbf{B})$ and the geomagnetic azimuth $\phi_g = \angle(\hat{\mathbf{e}}_x, \hat{\mathbf{e}}_y)$. The coordinate transformations used for simulations and data reconstruction are given in Appendix D.

5.1.1. Coherence of the radio emission

Let us consider the lateral distribution and try to understand its formation from the calculations based on the approach explained by Allan [139]. There is assumed, that radio emission from certain altitude is proportional to the number of shower particles at this altitude. This is a good approximation for the strength of the the geomagnetic effect, which depends on the derivative of the induced current. A second approximation treats the shower front as a surface collapsing the thickness to zero, which is valid for the frequencies up to GHz (i.e. thickness should be less than wavelength). Allan gives the following expression for

¹Parts of this Chapter have been published in Astroparticle Physics [138].

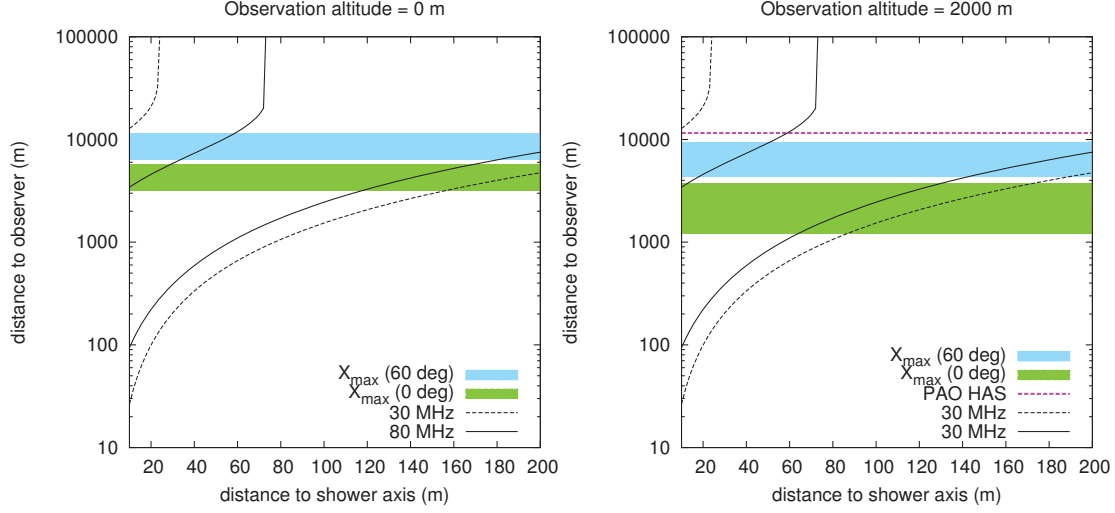


Figure 5.1.: Coherence limits during air-shower development with respect to the observer. This plot marks the altitudes where radio emission is added coherently, when the observer is located at the sea level (*left*) or at higher altitudes (*right*), such as the Pierre Auger Observatory [33] or IceTop [14]. Shaded areas indicate depths of 500-700 g/cm² of vertical (green) and inclined (blue) air-showers calculated using corresponding atmosphere model. In the areas between the lines (dashed and solid for 30 and 80 MHz, respectively) the emission adds coherently (the amplitude is proportional to $N(h)/h$, where $N(h)$ is the number of particles at the altitude h). The line “PAO HAS” indicates the shower maximum of an air-shower with $E_{pr} = 10^{19}$ eV and $X_{max} = 770$ g/cm² with inclination of 80°.

the amplitude of radio emission at the distance r

$$\mathcal{E}(r) = \kappa \int_{h_1^\nu(r)}^{h_2^\nu(r)} \frac{N(h)}{h} dh, \quad (5.4)$$

where $N(h)$ is a number of particles at altitude h (observation level $h = 0$ m), ν is radio frequency in MHz. $h_2^\nu(r)$ and $h_1^\nu(r)$ are integration limits derived from equations

$$\Delta t(r, h_c^\nu) + \frac{1}{2\pi\nu} = \Delta t(r, h_{1,2}^\nu), \quad (5.5)$$

where $\Delta t(r, h)$ is the time delay due to Čerenkov effects, r/h_c is the sine of the Čerenkov angle. The minimum detection delay for an antenna at distance r is at altitude h_c

$$\frac{d}{dh_c} \Delta t(r, h_c) = 0, \quad h_c = f(r, n_r), \quad (5.6)$$

$$\Delta t(r, h) = \cos\left(\arctan\left(\frac{r}{h}\right)\right) \int_0^h \frac{n_r(h')}{c} dh' - \frac{h}{c}, \quad (5.7)$$

where $n_r(h')$ is refractive index at the height h' . In vacuum ($n_r(h') = 1$) the solution gives $h_{1,2}^y(r) = \pm\infty$, i.e. coherence is conserved everywhere. If one takes a more realistic atmosphere into account, for example, the standard U.S. atmosphere from CORSIKA, one obtains the integration limits $h_{1,2}^y(r)$ defining the radio emission from the air-shower developing in the atmosphere. The integration limits for the frequencies 30-80 MHz against the distance to the shower axis are given in Fig. 5.1. One can see that close to the shower axis ($r < 50$ m) an observer antenna receives emission only from a part of the air-shower, especially for higher frequencies (see areas between solid and dashed lines). On the lateral distribution of amplitudes the region of 50-150 m looks makes a bump (or plateau, when $h_{\max} \gg h_c \cup h_{\max} \ll h_c$). One can conclude, that for the estimation of the primary energy it is sufficient to measure an amplitude at one single distance r chosen from the relations $h_1^y(r) \ll h_{\max} \cap h_2^y(r) \gg h_{\max}$, where $\hat{\nu} = (\nu_{\min}, \dots, \nu_{\max})$ is the frequency domain of the detector. On the other hand, measurements at distances with $h_{1,2} \approx h_{\max}$ indicate the location of the shower maximum, the latter can be probed by the slope of the spectrum of the lateral distribution.

5.1.2. Lateral distribution beyond the Čerenkov effects

From previous calculations one can see that $h_1(r) \sim h_a(r/r_0)^\alpha$, and at large r and $h_1 > h_{\max}$ one has the relation

$$\mathcal{E} \sim \frac{N(h_{\max})}{h_{\max}} \int_{h_a(r/r_0)^\alpha}^{\infty} \exp(-h/h_{\max}) dh = \frac{N(h_{\max})}{h_{\max}} \exp\left(\frac{h_a}{h_{\max}} \left(\frac{r}{r_0}\right)^\alpha\right) \quad (5.8)$$

This formula explains the exponential nature of the lateral distribution of radio amplitudes at distances larger than about 100 m from the shower axis. First work on exponential LDF was done by Allan et.al [51]. This way, the radio lateral distribution can be approximated by the general exponential parameterization

$$\mathcal{E}_N(r) = \mathcal{E}_{r_0} \exp[f_\eta(r - r_0)], \quad \text{with } f_\eta(x) = \sum_{k=1}^N a_k x^k, \quad (5.9)$$

with parameters a_k depending on the characteristics of the specific air-shower. The parameter r_0 is a technical parameter not determining the shape of the function, and can be set to a defined, arbitrary value when fitting the lateral distribution function (LDF). In the Section 5.4 it is shown, that $\mathcal{E}_2(r)$, i.e. $N = 2$ (Gaussian) provides a good and sufficient description of the radio lateral distributions measured with sparse arrays, in particularly with Tunka-Rex.

5.1.3. “Tomography” with a dense array

Exploiting the information about the coherence, one can perform so-called tomography, with a dense radio array. Lets consider a case when $h_2^y(r) > h_0$, where h_0 is the altitude of the first interaction

$$\mathcal{E}(r) = \kappa \int_{h_1^y(r)}^{\infty} \frac{N(h)}{h} dh \quad (5.10)$$

Let us vary $\mathcal{E}(r)$

$$\frac{d}{dr} \mathcal{E}(r) = \frac{d}{dr} \kappa \int_{h_1^{\nu}(r)} \frac{N(h)}{h} dh = -\kappa \frac{N(h_1^{\nu}(r))}{h_1^{\nu}(r)} \frac{dh_1^{\nu}(r)}{dr} \quad (5.11)$$

Thus, the difference of the amplitudes at the antennas behind the Čerenkov ring can be sensitive to a “slice” (number of particles at a certain altitude) of air-shower

$$N(h_1^{\nu}(r)) = -\kappa^{-1} \frac{d\mathcal{E}(r)}{d \log(h_1^{\nu}(r))} \quad (5.12)$$

It is worth noting, that a similar idea is exploited in the spectral slope approach [140].

5.2. Simulation of radio pulses

As discussed in Chapter 3.2, there are a number of different software packages for simulation of extensive air-showers and the calculation of the radio emission. In case of Tunka-Rex, the CoREAS [54] software was chosen because it gives a good description of experimental data, and both CORSIKA [66] and CoREAS are developed in KIT. Moreover, CoREAS and ZHAires are in good agreement [73]. For a high-energy hadronic interaction model it was selected QGSJET-II.04 [141], and FLUKA [142] for low-energy interactions. The standard atmosphere configuration (U.S. standard atmosphere)² is used. Combining these packages allow realistic simulation of measurable radio pulses at the surface of the detector.

5.2.1. Shower maximum determination

Apart from the parameters of the air-shower, such as primary particle and direction, which are directly defined at the initial point, the shower maximum is derived from a complex combination of chemical composition, primary energy and atmospheric properties. This property has a stochastic nature, which is defined by the first interaction of the primary particle with atmosphere.

Later in the shower development it could be interpreted in terms of cross-section. From the other side, one measures the concrete value following the given distribution.

CORSIKA, a Monte Carlo software, uses a random number generator to calculate particle cross-sections. This generator is initialized by user-specified random seeds. In other words, one can determine an entire air-shower by fixing the initial random seed. That means, one obtains the required shower maximum by tuning initial seeds, until the simulation agrees with measurement.

The main issue with this task is that calculations of the air-shower development and, especially, its radio emission are very resource-intensive. In order to find the appropriate air-shower simulation in a reasonable time, one should find a way to estimate the shower maximum. The solution to this issue comes from an optimized semi-analytical hybrid software, called CONEX [68]. This software numerically solves one-dimensional cascade equations and predicts the distribution of secondary particles, i.e. can give an estimation for the shower maximum.

²See details in user guide on <https://www.ikp.kit.edu/corsika/>

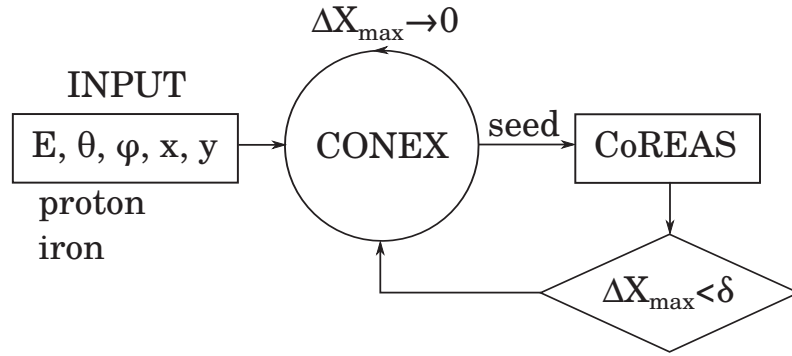


Figure 5.2.: Schematic representation of the shower-maximum fitting procedure. CORSIKA steering cards with two different primaries (proton and iron nuclei) are run in CONEX mode with different initial random seeds until the difference between the targeted and CONEX shower maxima, ΔX_{\max} , is less than the defined value δ . Then, the full CoREAS simulation runs using this random seed.

Taking all the foregoing into account, the simulation sequence has the following form: assuming that two boundary cases, proton and iron nuclei, can produce a cascade with wide-range distribution of X_{\max} , CONEX is run with different random seeds. When X_{\max} calculated by CONEX is obtained sufficiently close to the measured event, a CoREAS simulation runs with full precision (see Fig. 5.2). It is worth noticing, that shower maxima from CONEX and CoREAS can slightly differ from each other. Moreover, in some cases this procedure can converge for both primary particles, proton and iron nuclei. An additional software, called SiMM³ has been developed by me in the frame of the present work [143] (more detailed description is given in Appendix B).

5.2.2. Reproducing Tunka-133 events

The simulations made for the analysis described in the present work aim at several points: a theoretical study of the radio detection at the Tunka-Rex experiment, the development of the methods of reconstructing air-shower parameters, and a comparison between theoretical predictions and measured data. The last point is especially interesting because of the high precision of the hosting Tunka-133 experiment, i.e. the measured events can be reproduced with high accuracy, and, consequently, low systematic uncertainty. The selected events satisfy the condition $E_{\text{pr}} \sin \alpha_g > 0.05$ EeV. Tunka-133 reconstructs only air-showers with zenith angles $\theta < 50^\circ$ due to design restrictions. That way, the initial parameters, the energy of the primary particle E_{pr} , the arrival direction (θ, ϕ) , and the core coordinates (x_0, y_0) in the detector plane are used. The shower maximum was fitted using the CONEX and SiMM softwares, the uncertainty for ΔX_{\max} was set to 30 g/cm^2 , which is close to the precision of Tunka-133 [43]. For this study the detector setup of the Tunka-Rex experiment of 2012/2013, i.e. TREX-18 (see previous Chapter) is used, with an altitude of 675 m a.s.l. The strength of the geomagnetic field was set to $\approx 60 \mu\text{T}$, with inclination and declination of about 72° and -3° , respectively. One can see the exact parameters of the site in Table 5.1.

Following the concept of semi-blind analysis (see Chapter 6.1), measured and recon-

³Available on simm.tunkarex.info

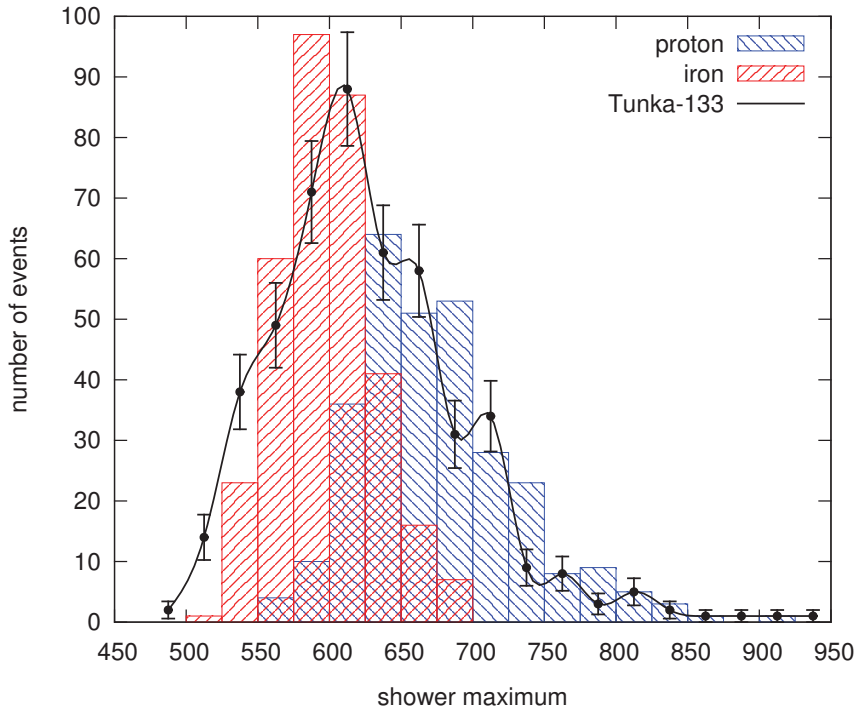


Figure 5.3.: Shower maximum reconstructed by Tunka-133 in comparison with CORSIKA simulations made for Tunka-Rex. The blue and red bars show the proton and iron simulated events, respectively, with the smallest deviation from Tunka-133 shower maximum reconstruction (black curve).

Table 5.1.: Geometrical properties of the Tunka site

Coordinates	$51^{\circ} 48' 35''$ N, $103^{\circ} 04' 02''$ E
Altitude	675 m
Magnetic field strength	$60.32 \mu\text{T}$
Magnetic field declination	-2.76°
Magnetic field inclination	71.76°
Atmospheric depth	955 g/cm^2

structed Tunka-133 events from 2012/2013 were used as the input dataset. The total number of Tunka-133 events with $E_{\text{pr}} \sin \alpha_g > 0.05$ is 1044, approximately half of them (405) have been fully simulated, which provides sufficient statistics. The number of proton-like and iron-like events are 296 and 332, respectively (for some events only the proton or iron shower have X_{max} close to Tunka-133 X_{max}). Thereafter this set is named R-SET. The distribution of shower maxima for the Tunka-133 detector and CORSIKA simulations is given in Fig. 5.3. Detailed description of the simulation sets and some examples are given in Appendix B.

Signal transformation and event selection on the detector level are made with the `Offline` software framework [135]. The reconstruction method for measured Tunka-Rex signals is

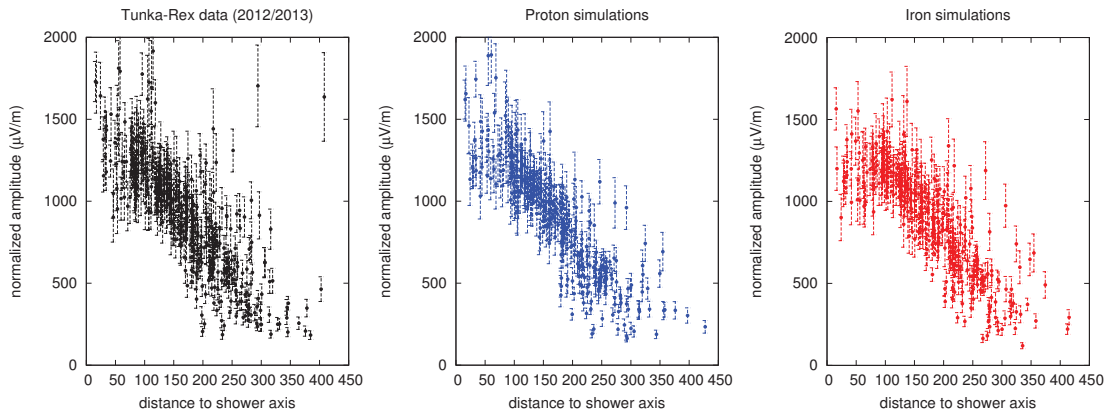


Figure 5.4.: Comparison of lateral distributions of Tunka-Rex events from 2012-2013, and simulations using proton and iron primaries. The lateral distributions of Tunka-Rex events (*left*), normalized by the factor $(E_{\text{ev}}/E_{\text{pr}})$, where E_{pr} is the primary energy, reconstructed with the standard Tunka-Rex pipeline. The lateral distributions for simulated events with primary proton (*middle*) and iron (*right*) were also reconstructed with standard pipeline after adding noise samples. There is a significant difference between the lateral distributions of proton and iron events due to the depths of shower maximum (here the cut of $\Delta X_{\text{max}} = 30 \text{ g/cm}^2$ is not applied, i.e. the true X_{max} of simulations may differ from the measured X_{max}).

also used for the analysis of simulated events, without noise: at the first point the noise was not added. It can be imported to simulated events independently during later analysis, and used for the realistic estimation of detector properties.

A detailed comparison of simulated and measured amplitudes is done in Ref. [133], here only the general illustration is given: in Fig. 5.4 one can see the normalized lateral distribution of the Tunka-Rex amplitudes measured in 2012/2013 and the distribution of the amplitudes of the same events obtained in simulations and reconstructed using the standard Tunka-Rex methodology and procedure.

5.2.3. A three-dimensional simulation of the radio emission

Traditional simulations that reproduce a set of air-showers measured by a static detector can help in developing a phenomenological methodology of air-shower reconstruction and estimate systematic uncertainties of such methods. However, it is hard to look closer to fine structures of air-showers using these simulations. What if one moves detector along the shower axis and see how the picture of the development changes? This three-dimensional method allows one to obtain a radio image of the air-shower in contrast to non-imaging traditional simulations, which show the integrated lateral distribution. This way, one can study fine features of the radio emission from air-showers and their dynamics with atmospheric depth. There the focus is on proving the principle concepts, thus, the present three-dimensional study is not as detailed as it could be. Additional studies will further define the method and results.

A three-dimensional simulation was performed with the following strategy: the same

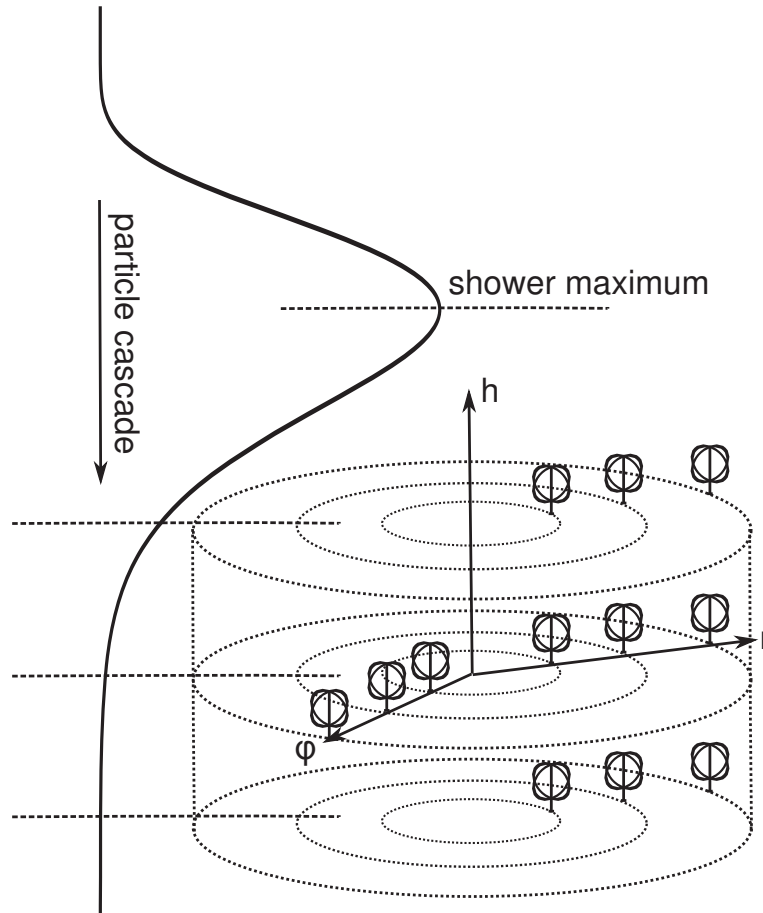


Figure 5.5.: Schematic representation of a three-dimensional simulation. In comparison with statistical studies with a static detector and a set with different air-showers, the single shower tomography was performed. The detector planes were placed at different observation levels; one can see how air-shower develops with the varying depth. From this one can predict some fine structure characteristics of the air-shower development, for example, asymmetry features (see next sections).

vertical air-shower induced by a proton with initial energy 0.1 EeV was simulated several times for different observers. The geomagnetic field was set to a strength of about $60 \mu\text{T}$ (similar to the strength at the Tunka Valley) with geomagnetic angle $\alpha_g = 45^\circ$. The CoREAS simulated shower has its maximum at an atmospheric depth of about 630 g/cm^2 . Each simulation includes an observer plane, where observation layers change from 800 to 1000 g/cm^2 with steps of 10 g/cm^2 . Each layer consists of concentric rings with radii from 20 to 300 m with steps of 10 m. Each ring consists of 36 antennas placed with azimuthal steps of 10° . Thereafter for this set the name T-SET is used. A visual representation can be seen in Fig. 5.5 and antenna statistics are given in Table 5.2. Obtained footprints by layer are given in Appendix E.

Table 5.2.: Configuration of the tomographic simulation. The primary particle is a proton with $E_{\text{pr}} = 0.1 \text{ EeV}$, the maximum of the air-shower is $X_{\text{max}} \approx 630 \text{ g/cm}^2$. The air-shower has the vertical direction ($\theta = 0$) and the magnetic field with strength of about $60 \mu\text{T}$ has an declination to shower axis of 45° .

Observation depth	800 – 1000 g/cm^2	... with step of 10 g/cm^2
Radial coordinates	20 – 300 m	... with step of 10 m
Angular coordinates	$0^\circ - 350^\circ$... with step of 10°
		21924 antennas
		1044 per layer

5.3. Asymmetry

Presently, several air-shower radio-emission mechanisms are suggested by theorists. In the present work only two contributions, which have been proven experimentally are considered: geomagnetically induces transverse currents [49] and Askaryan effect [50]. The geomagnetic-like contribution was proven by historic experiments [51], the precise measurements of the Askaryan contribution to the radio emission from air-showers were done only in recent works [90, 88]. Nevertheless, thanks to collider experiments, it was shown, that these two terms describe the radio emission from cascades in a magnetic field with very good accuracy. At least, contributions from other effects are smaller than experimental and model uncertainties [144, 145].

The complexity of combining these two contributions arises from the different mechanisms of emission. If the electrical field of geomagnetic emission is obtained by the integration of $N(h)$ and lies along the $\mathbf{v} \times \mathbf{B}$ vector, the Askaryan emission is mostly defined by the derivative $N'(h) = dN/dh$ and polarized along $\mathbf{v} - \mathbf{V}$. Here $N(h)$ is the number of charged particles at altitude h ($h = 0$ at observation level), \mathbf{B} is the vector of Earth's magnetic field, \mathbf{V} is the shower axis, \mathbf{v} is the position of the observer in the air-shower plane. Here it is assumed that the total polarization is simply sum of two linear polarized contributions with unknown amplitudes. In other words this assumption implies equal distance to the main source of the emission for different mechanisms, which is only a first-order approximation [54, 146].

5.3.1. Introduction

The total electrical field at an antenna at distance r can be represented as vector

$$\mathcal{E} = \mathcal{E}_g + \mathcal{E}_{\text{ce}} + \mathcal{E}_v, \quad (5.13)$$

where \mathcal{E}_g is a geomagnetic contribution, \mathcal{E}_{ce} is a contribution from Askaryan effect and $\mathcal{E}_v \approx 0$ is a vertical contribution to the signal. The contribution from the vertical component is negligible, since the angle between the shower plane and radio wavefront is $1 - 2^\circ$ only [147]. The signal has following components in the introduced geomagnetic coordinate system

$$\mathcal{E}_g = (\mathcal{E}_g, 0, 0) = (\mathcal{E}_0 \sin \alpha_g, 0, 0), \quad (5.14)$$

$$\mathcal{E}_{\text{ce}} = (\mathcal{E}_{\text{ce}} \cos \phi_g, \mathcal{E}_{\text{ce}} \sin \phi_g, 0), \quad (5.15)$$

where $\mathcal{E}_g = \mathcal{E}_0 \sin \alpha_g \sim E_{\text{pr}} \sin \alpha_g$ and $\mathcal{E}_{\text{ce}} \sim E_{\text{pr}}$, and E_{pr} is the energy of the primary particle. The strength of the radio emission depends linearly on the electromagnetic component (and, consequently, on the total energy) of the air shower. Thus, the total amplitude takes the form

$$\mathcal{E} = \mathcal{E}_g + \mathcal{E}_{\text{ce}} = (\mathcal{E}_0 \sin \alpha_g + \mathcal{E}_{\text{ce}} \cos \phi_g, \mathcal{E}_{\text{ce}} \sin \phi_g, 0) \quad (5.16)$$

The squared amplitude has the form

$$\begin{aligned} \mathcal{E}^2 &= (\mathcal{E}_0 \sin \alpha_g + \mathcal{E}_{\text{ce}} \cos \phi_g)^2 + \mathcal{E}_{\text{ce}}^2 \sin^2 \phi_g \\ &= \mathcal{E}_0^2 ((\sin \alpha_g + \varepsilon \cos \phi_g)^2 + \varepsilon^2 \sin^2 \phi_g), \end{aligned} \quad (5.17)$$

where asymmetry is defined as $\varepsilon = \mathcal{E}_{\text{ce}}/\mathcal{E}_0$. As one can see, the one-dimensional LDF transforms itself to a two-dimensional expression when taking into account the contribution from the charge excess phenomena: $\mathcal{E}(r) \rightarrow \mathcal{E}(r, \phi_g)$. To reduce the number of dimensions a special operator \hat{K} eliminating the azimuthal dependence is defined

$$\hat{K}\mathcal{E}(r, \phi_g) = \mathcal{E}_{\text{corr}}(r). \quad (5.18)$$

Assuming $\mathcal{E}_z = \mathcal{E}_v = 0$ one can measure the two significant components of the electrical field

$$\begin{cases} \mathcal{E}_x = \mathcal{E}_0 \sin \alpha_g + \mathcal{E}_{\text{ce}} \cos \phi_g \\ \mathcal{E}_y = \mathcal{E}_{\text{ce}} \sin \phi_g \end{cases}. \quad (5.19)$$

By solving this system the asymmetry ε is obtained

$$\varepsilon = \frac{\mathcal{E}_{\text{ce}}}{\mathcal{E}_0} = \frac{\mathcal{E}_y / \sin \phi_g}{\mathcal{E}_x - \mathcal{E}_y \cot \phi_g} \sin \alpha_g \quad (5.20)$$

From Eqs. (5.17) and (5.18) it is obvious that \hat{K} takes the form

$$\hat{K} = (\varepsilon^2 + 2\varepsilon \cos \phi_g \sin \alpha_g + \sin^2 \alpha_g)^{-\frac{1}{2}}, \quad \hat{K}\mathcal{E}(r, \phi_g) = \mathcal{E}_{\text{corr}}(r) \Big|_{r=\text{const}} = \mathcal{E}_0. \quad (5.21)$$

In the geomagnetic limit ($\mathcal{E}_g \gg \mathcal{E}_{\text{ce}}$) thus

$$\hat{K} = \frac{1}{\sin \alpha_g}, \quad \mathcal{E}_{\text{corr}} = \mathcal{E} / \sin \alpha_g. \quad (5.22)$$

5.3.2. Asymmetry behavior

For the asymmetry reconstruction, the formulas given in Eq. (5.19) are used. The distribution of the asymmetry values for different showers is broad, thus, it is useful to create a profile distribution for the asymmetry values (see Fig. 5.6). The results for proton and iron are similar within about 10%.

From this picture one can conclude that the strength of the asymmetry varies not only from shower to shower, but also with distance to the shower axis. Similar results were obtained in Ref. [146]. There it was shown that the asymmetry has a complicated structure; since geomagnetic and charge excess emission have their maxima at different altitudes, combining these effects leads to non-trivial addition of these components. Taking the longitudinal development of the air-shower into account, de Vries states that the behavior in

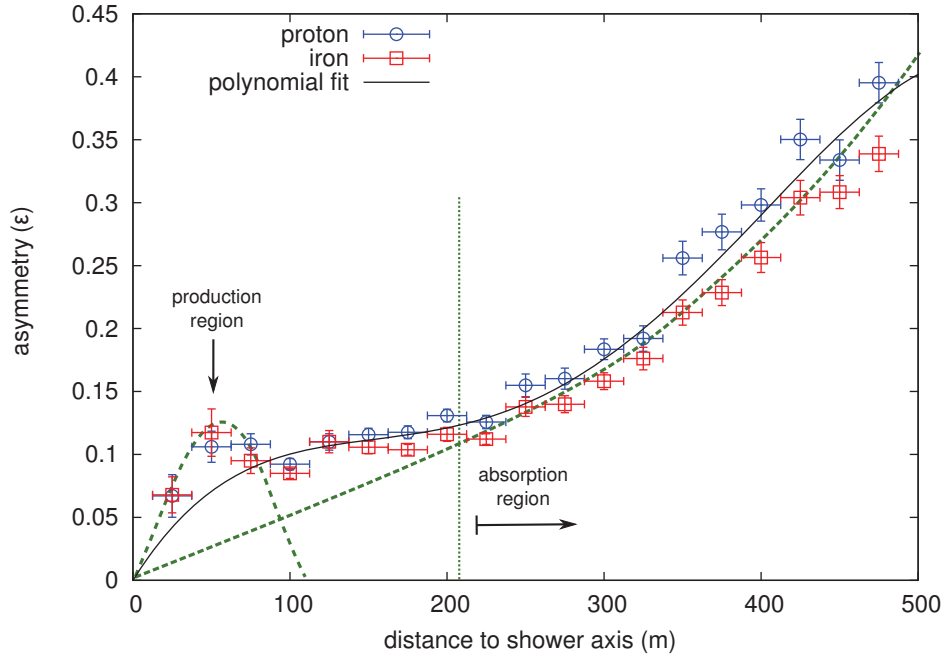


Figure 5.6.: Averaged asymmetry profile of the radio lateral distribution for protons and iron nuclei.

the near region (up to 150 m from the shower axis) is mostly caused by Čerenkov-like effects. His statement does not explain the peak in the asymmetry appearing in this region. One can give a potential explanation considering the lateral structure of an air-shower. The existence of two sources for the charge excess contribution: intensive particle production and inelastic scattering close to the shower axis with particle absorption at distances far from the shower axis (the latter generally agrees with de Vries). In other words, in this peak we see the radio emission from the charge excess arising from very intensive particle interaction (like in the classical Askaryan effect in dense media). The behavior of the production and absorption regions could also depend on the distance to the shower maximum.

To prove this statement the simulated radio profile of an air-shower is made with dataset T-SET. The obtained results show that the behavior of the asymmetry in the absorption region does not depend on the shower maximum. But the position and height of the peak in the production region has a clear correlation with distance to the shower maximum (see Fig. 5.7). As one can see, it has the opposite behavior than expected from the Čerenkov-like explanation given by de Vries [146]. In the case of a Čerenkov-like nature, the peak should move further away from the shower axis with increasing observation level, but the opposite trend is observed. Possibly, this indicates that after shower maximum the lateral extension of the shower region relevant for Askaryan emission shrinks closer to the shower axis.

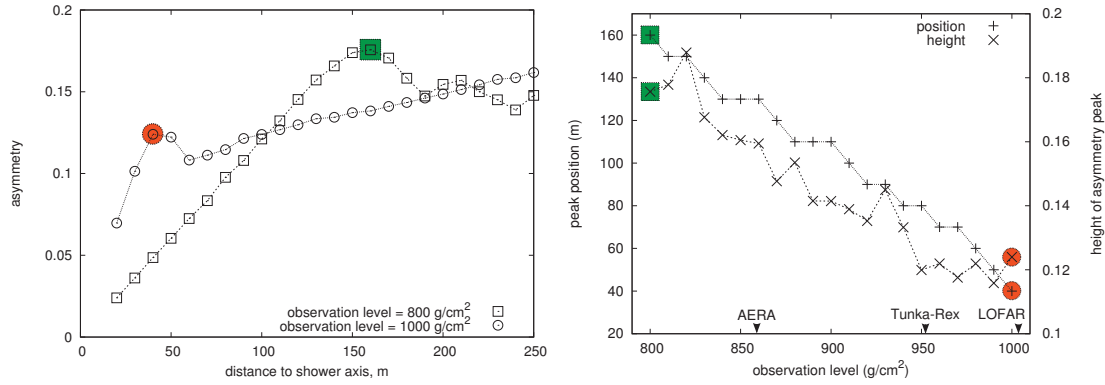


Figure 5.7.: Distribution of the asymmetry against the distance to the shower axis for different observation depths.

Left: The distribution of asymmetry against distance to shower axis for two boundary observation levels: 800 g/cm² and 1000 g/cm². Highlighted points indicate peaks and show correspondence between left and right plots.

Right: Correlation between height and position of the asymmetry peak in the production region as function of the observation level of the shower. The observation levels for several modern experiments for vertical showers are marked: AERA, Tunka-Rex and LOFAR. The results are obtained for one exemplary vertical CoREAS shower with a primary energy of 0.1 EeV. The lines connect the points to guide the eye.

Table 5.3.: Global fit values for the asymmetry-profile fit in Fig. 5.6 of averaged CoREAS simulations (from the T-SET).

Parameter	Value
a_1^ε	$(2.00 \pm 0.10) \cdot 10^{-3} \text{ m}^{-1}$
a_2^ε	$(-1.37 \pm 0.12) \cdot 10^{-5} \text{ m}^{-2}$
a_3^ε	$(4.10 \pm 0.46) \cdot 10^{-8} \text{ m}^{-3}$
a_4^ε	$(-3.67 \pm 0.56) \cdot 10^{-11} \text{ m}^{-4}$

5.3.3. Parameterization of asymmetry

The peak in the production region depends on the shower geometry. Nevertheless, the relative height of the peak is small, especially for observatories located deep in the atmosphere like Tunka-Rex (see Fig. 5.7), and, therefore, can be neglected in first order. The absorption region has negligible dependence on the shower geometry, therefore the asymmetry is described as a function $\varepsilon_p(r)$ of distance to the shower axis r with fixed point $\varepsilon_p(0) = 0$

$$\varepsilon_p(r) = \sum_{k>0} a_k^\varepsilon r^k. \quad (5.23)$$

For simplification, higher orders of the polynomial are set to zero, $a_{k>4}^\varepsilon = 0$, and fitted for both types of initial particles. The fit values are given in Table 5.3.

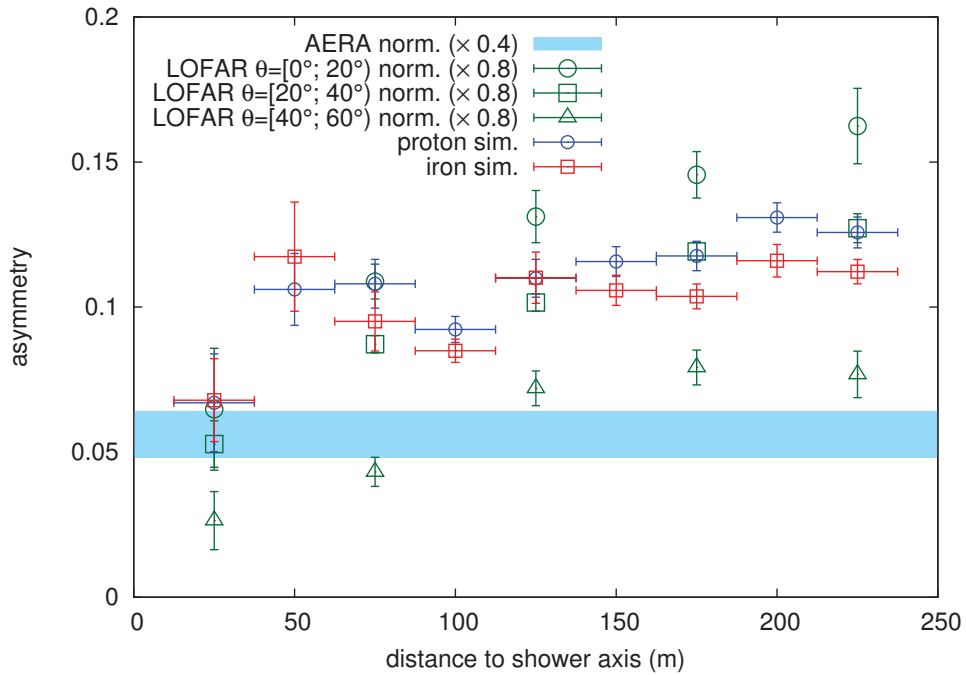


Figure 5.8.: Comparison between experimental observations [90, 88] of the asymmetry and their theoretical prediction made for Tunka-Rex. Experimental points have been normalized to the strength of the magnetic field in Tunka Valley.

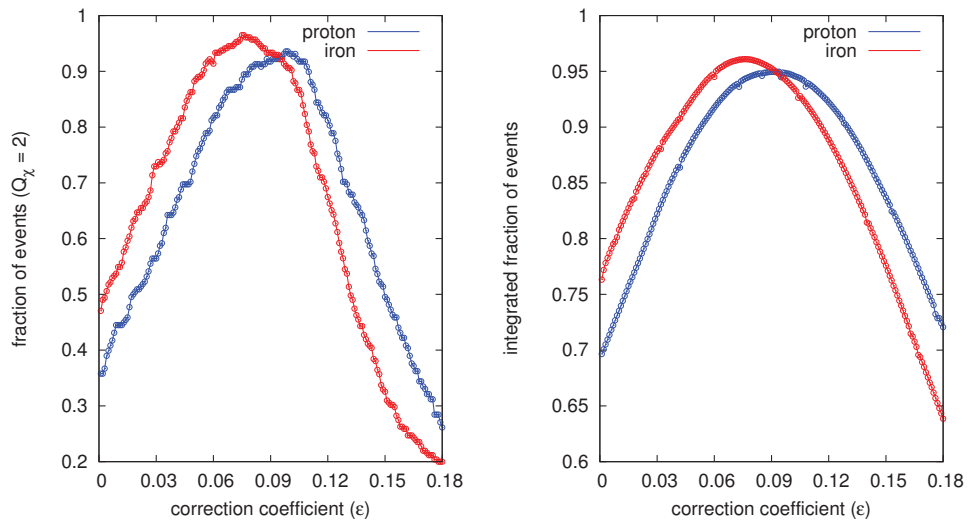


Figure 5.9.: Quality of the correction presented in Eq. (5.24).

Left: Differential quality $N_\chi(Q_\chi, \epsilon)$.

Right: Integral quality $\int N_\chi(Q_\chi, \epsilon)$ for $Q_\chi = 0, \dots, 16$. One can see clear peaks, which are the solutions of Eq. (5.24).

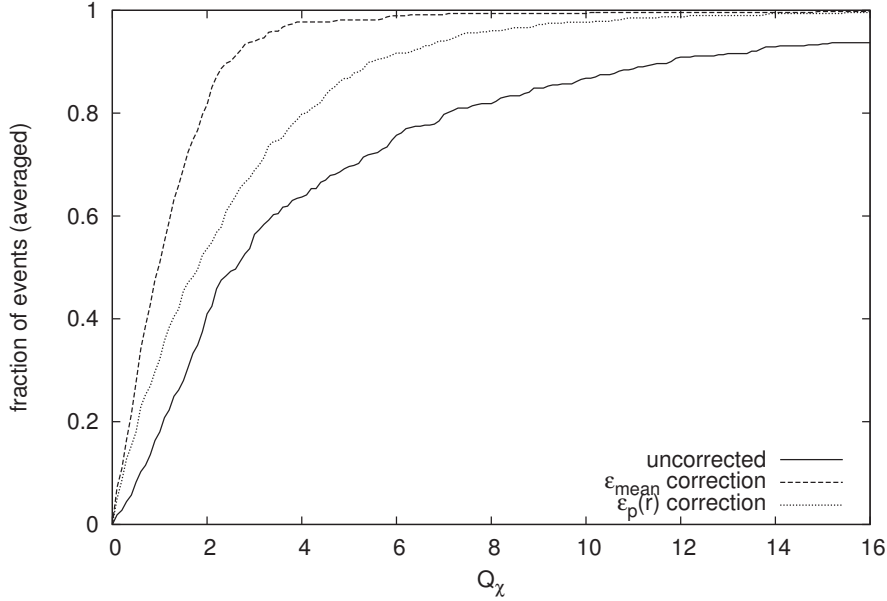


Figure 5.10.: Comparison between different methods of correction for about 300 simulated showers. The fraction of accepted events $N_\chi(Q_\chi, \varepsilon)$ is calculated for the different forms of LDF $\hat{K}(\varepsilon)\mathcal{E}_2(r)$: uncorrected ($\varepsilon = 0$), constant correction ($\varepsilon = \varepsilon_{\text{const}} = 0.085$), correction with parameterization ($\varepsilon = \varepsilon(r)$). Using a constant value for the correction of the azimuthal asymmetry provides the best quality when fitting a one-dimensional LDF.

One determines the approximate mean asymmetry value by solving the equation $\varepsilon_p''(r) = 0$. It is worth noting that the statistical mean depends on the choice of the integration range, which can depend on the shower geometry. To obtain a more stable value it was decided to take the point of inflexion. This point is at distances of 100-200 m from the shower axis, where typically most antennas with signal are located, and where ε is roughly constant. The asymmetry obtained in this way at $r \approx 150$ m is $\varepsilon_{\text{mean}} = 0.11 \pm 0.02$. This value is in agreement with previous observations [90, 88], where the dependence of ε over distance to shower axis and zenith was experimentally studied [88]. It is important to note that in spite of the geometric invariance of ε it still depends on the strength of the magnetic field \mathbf{B} , since $\mathcal{E}_g = \mathcal{E}_g(\mathbf{B})$. That means, that the fraction of charge excess ε should be roughly antiproportional to $|\mathbf{B}|$. Consequently, the value of ε for the situation of Tunka-Rex is slightly smaller than the value found by the AERA and LOFAR experiments [90, 88]. A comparison between different results is given in Fig. 5.8. The asymmetry values are normalized by $|\mathbf{B}|$.

The next question to be studied is: what is the most simple function for describing the asymmetry, ε , sufficiently for a satisfactory description of the LDF after correction with $\hat{K}(\varepsilon)$? A chi-square test was used to determine the quality of the correction. For this purpose the quality of the correction is defined by the quantity $N_\chi(Q_\chi, \varepsilon)$ in the following way: the fraction of events passing the cut $\chi^2/\text{NDF} \leq Q_\chi$ when the LDF is fitted with $\hat{K}(\varepsilon)\mathcal{E}_2(r)$.

Let us start with the most simple function, a constant value of the asymmetry. To find

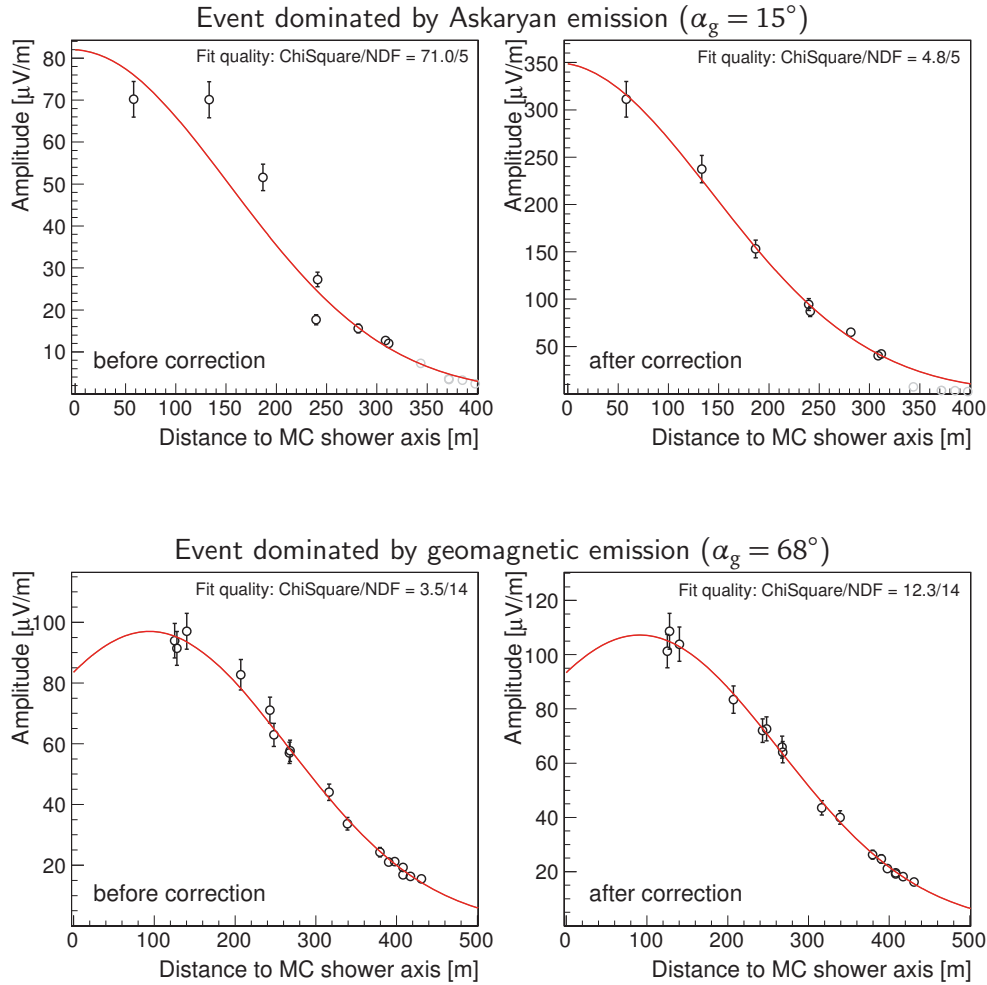


Figure 5.11.: Example events before and after asymmetry correction. This plot compares the quality of the LDF fit before (*left*) and after (*right*) asymmetry correction for two opposite cases: when the Askaryan effect dominates (*top*) and when the geomagnetic mechanism dominates (*bottom*). It is obvious, that this correction is more important for the first case, moreover, it enables the reconstruction of events when $\alpha_g \rightarrow 0$ (which is not possible with other methods, cf. Ref. [91]). For the second case, the asymmetry correction does not improve the reconstruction of the shower maximum using the LDF method and leaves it practically unaffected.

the optimal value $\varepsilon_{\text{const}}$ one solves the simple equation

$$\frac{d}{d\varepsilon} \int N_\chi(Q_\chi, \varepsilon) dQ_\chi = 0 \quad (5.24)$$

The behavior of the quality of the fit at different Q_χ and ε is presented in Fig. 5.9. Although Eq. (5.24) is in a non-trivial two-dimensional form, it has a simple meaning and only one solution.

The numerical solution of this equation gives the following values: $\varepsilon_{\text{const}}^{\text{proton}} \approx 0.095$ and

$\varepsilon_{\text{const}}^{\text{iron}} \approx 0.075$. If we compare the quality of the correction made with this constant asymmetry and the parameterized one (see Fig. 5.10), we can see that the simple constant function gives a better result. This can be explained by neglecting the peak close to the shower axis in the polynomial parameterization. The other important factor concerns the large deviations between individual simulated events at distances far from the shower axis (the spread at this distance is indicated by the larger error bars in Fig. 5.6), i.e. an effect of shower-to-shower fluctuations. A quantitative overestimation of the asymmetry can even decrease the quality of the correction.

The result that a constant value of ε yields, on average, an even better correction of the asymmetry than a polynomial makes the practical application of the correction approach very simple. Consequently, a correction by a constant value $\varepsilon = 0.085$ will be used for the further analysis.

In conclusion, it is important to note, that asymmetry correction is very important for reconstruction of the events with small geomagnetic angles. At the location of the Tunka-Rex experiment the influence of the Askaryan effect is only about 10% and impact of this correction (which should also be in order of percents) is visible on the larger statistics, for example, in one-antenna energy reconstruction [133]. Examples for the correction for events with small and large geomagnetic angles is given in Fig. 5.11.

5.4. Reconstruction of air-showers using the lateral distribution of radio amplitudes

A first approximation of the lateral distribution function was done by Allan et.al [51]. In his work an exponential-like parameterization was suggested (see Eq. 5.9). Until now, this parameterization was used for the data analysis of the modern experiments, like LOPES [81] and CODALEMA [83]. It is fair to say, that this parameterization is still good enough for the reconstruction of the primary energy [133].

5.4.1. Parameterization of lateral distribution

This Section describes the proper parameterization of the lateral distribution, necessary for the Tunka-Rex experiment. The description of all important features of the amplitude distribution is performed in order of keeping the number of free or arbitrary parameters as small as possible. A successful phenomenological description of the lateral distribution was undertaken by Nelles [148]. The main idea of her description is a two-dimensional fit of lateral distributions using the subtraction of two Gaussians as a fitting function. It was tested on a dense array with large number (> 200) of antennas per event. For sparse arrays with small number of antennas this approach is not suitable. In the approach of the present work, for reducing the number of parameters, one uses the knowledge of the radio emission phenomena. The main idea is that one observes a one-dimensional lateral distribution with azimuthal symmetry, which is broken by the Askaryan effect. This symmetry can be restored with the simple method, described in the previous Section. Thus, the lateral distribution with restored symmetry is implied: $\mathcal{E} \rightarrow \mathcal{E}_{\text{corr}} = \hat{K}\mathcal{E}$.

In the present study the minimal value of N for the Eq. 5.9 is chosen in order to describe lateral distributions of Tunka-Rex better than functions with smaller N . There are a few of alternative parameterizations [149, 150], but they are not considered in the present work. A first obvious feature is the Čerenkov ring due to propagation effects [139, 146]. For

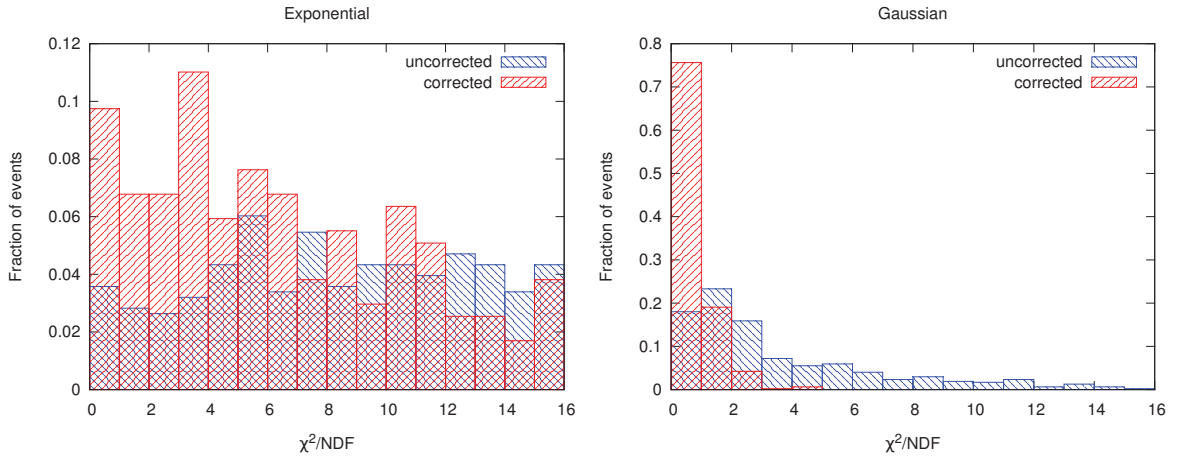


Figure 5.12.: Distribution of the quality of LDF fits for different parameterizations (Eq. 5.9): exponential ($N = 1$) and Gaussian ($N = 2$). The fraction of events with corrected $N_\chi(\chi^2/\text{NDF}, \varepsilon_{\text{mean}})$ and uncorrected $N_\chi(\chi^2/\text{NDF}, 0)$ LDFs is given as average of both primaries (proton and iron).

the geometry defined in Tunka-Rex simulations, the radius of the Čerenkov ring is about 100-150 m (see Fig. 5.13). This radius can be calculated from solving the equation (5.9)

$$\frac{d}{dr} \mathcal{E}_N(r) = 0, \quad r = r(r_0, a_k). \quad (5.25)$$

A solution can be found already at $N = 2$

$$r_{\check{c}} = r_0 - \frac{a_1}{2a_2}. \quad (5.26)$$

A comparison between different parameterizations has shown that for the selected (Tunka-Rex) geometry a Gaussian (i.e. $N = 2$) parameterization after asymmetry correction fits almost all events. For $N = 2$, the quality of fit $N_\chi(Q_\chi = 1) > 70\%$, while for a simple exponential LDF the quality $N_\chi(Q_\chi = 4) \approx 35\%$ (see Fig. 5.12).

The properties of the Gaussian LDF such as mean and width are connected to the distance to the shower maximum (Fig. 5.13)

$$\mu = r_{\check{c}} = r_0 - \frac{a_1}{2a_2} \quad (5.27)$$

$$\sigma = \frac{1}{\sqrt{-2a_2}} \quad (5.28)$$

5.4.2. Reconstruction of energy and shower maximum

Now that a good description for the lateral distribution valid for the Tunka-Rex detector is found, let us test methods for the reconstruction of the air-shower parameters. Let us follow

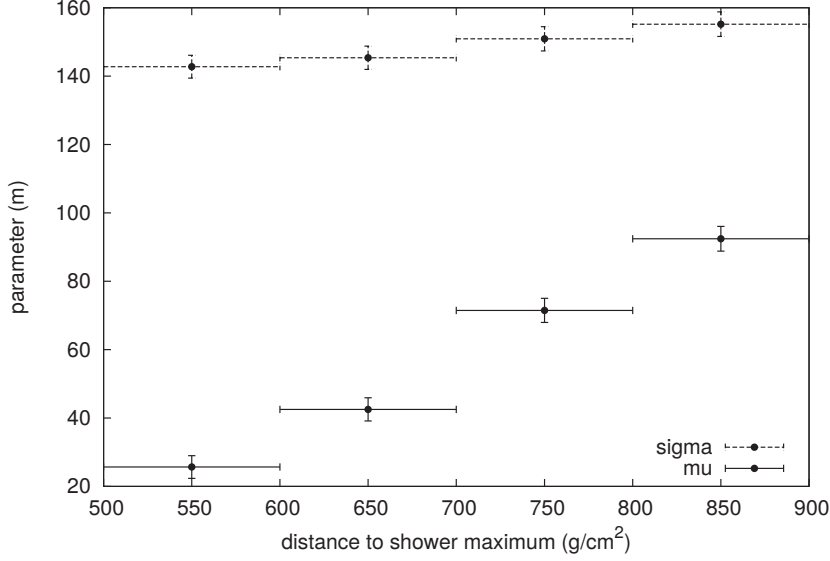


Figure 5.13.: Correlation between Gaussian LDF properties and distance to shower maximum. Definitions of mu and sigma are given in Eqs. (5.28).

the ideas developed for optical air-Čerenkov emission, because after asymmetry correction the radio emission behaves similarly.

The energy can be reconstructed by probing the signal amplitude at a defined distance r_e . Theoretical predictions for the optimal distance are about 50-150 m depending on the mass composition and geometry (see Ref. [51] and later). Therefore, in general, the energy and LDF are connected by the following phenomenological relation

$$E_{\text{pr}} = \kappa \left(\frac{\mathcal{E}(r_0 = r_e)}{\text{V/m}} \right)^b, \quad (5.29)$$

where κ is an amplitude slope parameter and b is a power coefficient. In other words, the energy is proportional to the amplitude at a certain distance r_e . To simplify experimental data analysis, one can set the arbitrary defined parameter r_0 in the fit to r_e and take the fitted value \mathcal{E}_{r_0} with corresponding fitting uncertainty as an energy estimator. To find r_e one looks simultaneously at the correlation between logarithms of energy and amplitude at different r_e and at the precision of the energy reconstruction using Eq. (5.29) (see Fig. 5.14). The maximum of the correlation points to the distance optimal for the energy reconstruction. Since the relative difference between optimal distances r_e^{proton} and r_e^{iron} , and slopes κ^{proton} and κ^{iron} is only about 10%, the median values for the energy reconstruction are selected.

$$r_e = 120 \text{ m}, \quad (5.30)$$

$$\kappa = 422 \frac{\text{EeV}}{\text{V/m}}, \quad (5.31)$$

$$b = 0.93. \quad (5.32)$$

The precision of the energy reconstruction using these averaged parameters is better than 10% for both particle types (see Fig. 5.16). It is worth noticing, that since energy resolution of Tunka-Rex is similar to resolution of Tunka-133 (it was obtained already during

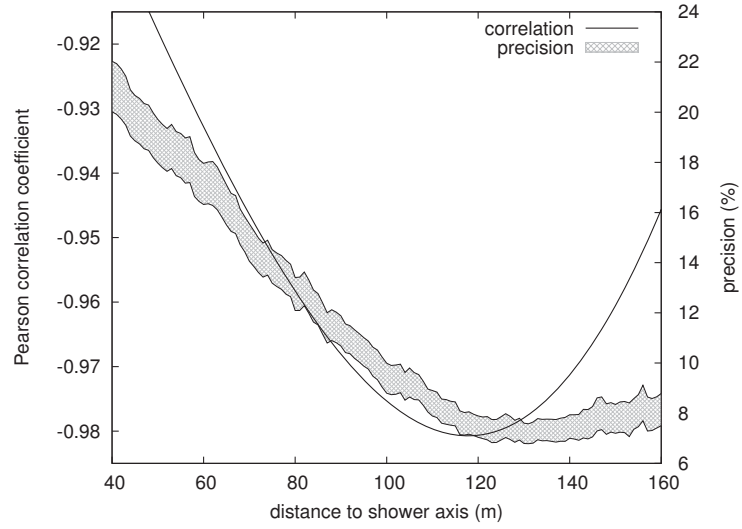


Figure 5.14.: Correlation between logarithms of amplitude and energy, and precision of the energy reconstruction using Eq. 5.29 at distances from 40 to 160 m. This range is chosen in order to keep the analytical behavior of $E_{\text{pr}}(\mathcal{E}_0)$.

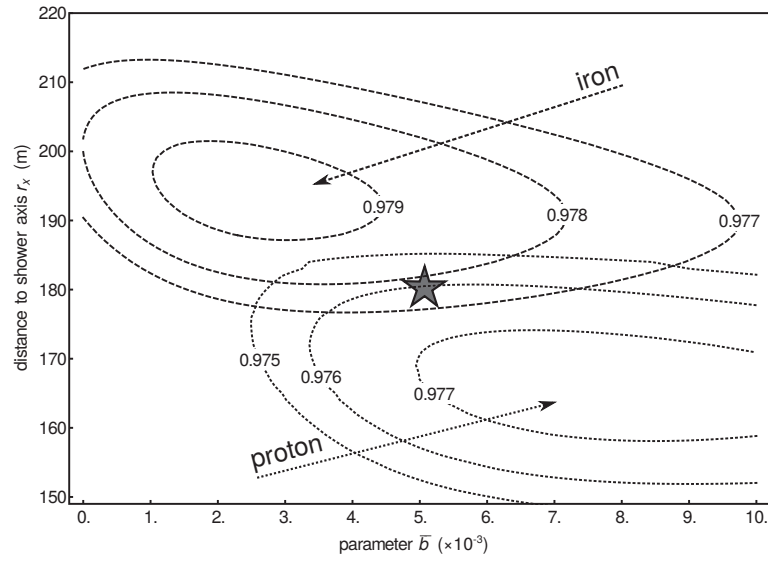


Figure 5.15.: Contour plot of the correlation between LDF slope η and true X_{max} depending on the LDF parameter r_x and the free parameter \bar{b} . By fixing \bar{b} , one obtains a distribution similar to Fig. 5.14. Adding \bar{b} as free parameter one obtains the two-dimensional dependence on (\bar{b}, r_x) . In the chosen range of this two-parametric space, the correlation function behaves analytically and converges around $(\bar{b} = 0.003 \text{ m}^{-1}, r_x = 195 \text{ m})$ and $(\bar{b} = 0.008 \text{ m}^{-1}, r_x = 165 \text{ m})$ for iron and proton primaries, respectively. The average point $(\bar{b} = 0.005 \text{ m}^{-1}, r_x = 180 \text{ m})$ was chosen for further analysis, marked as star on the plot.

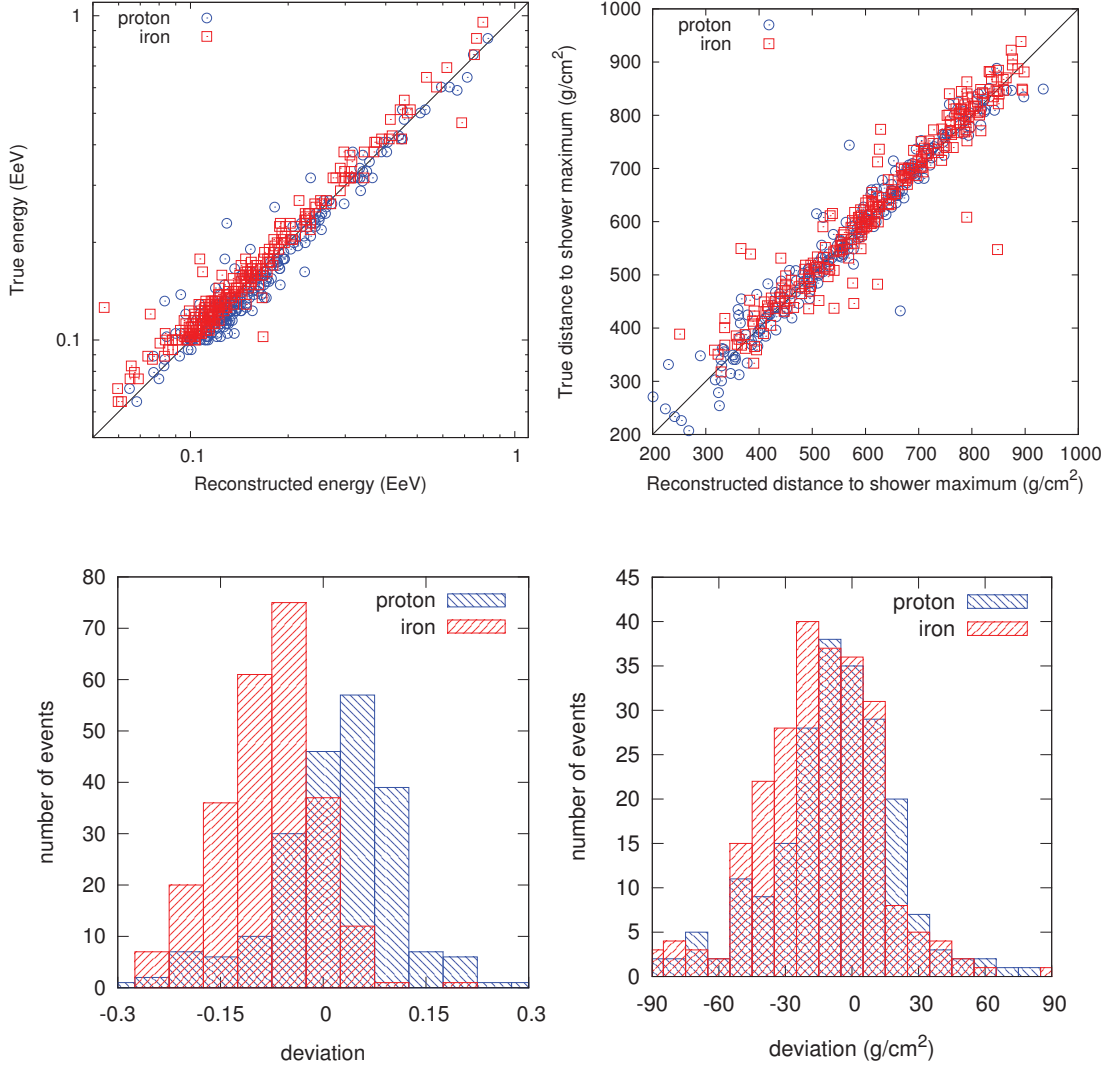


Figure 5.16.: Comparison between true and reconstructed primary energy and shower maximum of the CoREAS simulations.

preliminary analysis [151]), it was decided to simplify energy reconstruction in order to reduce the number of arbitrary parameters: parameter b was set to unity and the slope coefficient was redefined for linear case $\kappa \rightarrow \kappa_L = 844 \text{ EeV}/(\text{V}/\text{m})$ [152].

For the reconstruction of the atmospheric depth of the shower maximum (X_{max}) one can use a method where the slope parameter is defined as

$$\eta = \frac{df_\eta}{dr} = \frac{\mathcal{E}'}{\mathcal{E}} = 2a_2(r - r_0) + a_1. \quad (5.33)$$

η is the slope parameter a_1 when evaluating the Gaussian LDF at the distance $r = r_0$. In other words, to obtain the slope η of the lateral distribution, the fitted value a_1 was taken after setting $r_0 = r_x$, since the optimum distance for X_{max} reconstruction r_x is different from the distance r_e for energy reconstruction. In Refs. [153, 146] a similar method was presented using the slope of the LDF. For X_{max} reconstruction the parameterization suggested

in Ref. [43] is used

$$X_{\max} = X_{\text{det}} / \cos \theta - (A + B \log(a_1 + \bar{b})). \quad (5.34)$$

This formula is more complicated than the one chosen for energy reconstruction. It has two free parameters A and B which are obtained from a fit to the simulated showers, one distance-dependent parameter $a_1 = \eta(r_x)$, and one correction parameter \bar{b} . Let us follow the same procedure as for the energy reconstruction: find the best correlation between the reconstructed and true shower maximum depending on the point (r_x, \bar{b}) in the two-dimensional space. One can see the correlation in a contour plot (Fig. 5.15).

As for the energy reconstruction, parameters in Eq. (5.33) have about 10% dependence on the particle type. After averaging the parameters and applying the formula, the relative difference between true (simulated) and reconstructed X_{\max} values is smaller than 30 g/cm² (see Fig. 5.16). The averaged parameters are

$$r_x = 180 \text{ m}, \quad (5.35)$$

$$A = -1864 \text{ g/cm}^2, \quad B = -566 \text{ g/cm}^2, \quad (5.36)$$

$$\bar{b} = 0.005 \text{ m}^{-1}. \quad (5.37)$$

5.4.3. Systematic uncertainties

In the present study the mass of the primary particle is assumed as unknown, which leads to systematic uncertainties. The parameters for the absolute energy and shower maximum reconstruction were derived by averaging two boundary cases: protons and iron nuclei, which differ in the order of 10%. Tunka-Rex operates in a limited energy range (about one decade) and quite narrow solid angle. Thus, it is expected, that systematic effects should be small.

The analysis has shown that the reconstructed energy is not shifted systematically against the true energy except in cases, when the air-shower is clipped or very inclined (see Fig. 5.17). In the first case the air-shower is not fully developed when it reaches the ground, i.e. only a part of the possibly emitted energy is received by the antennas. The second case is less clear, and a possible explanation could be that the emission region ($\approx X_{\max} \pm n\lambda_e$) is squeezed, and the radio emission is less coherent than for vertical air-shower. Another reason could be that the intensity of the radio emission falls approximately as $1/d^2$, and the energy for a distant source can be underestimated, since this is not taken into account by the present method for energy reconstruction.

The reconstruction of the shower maximum does not depend on the primary particle and on the energy and zenith angle of the arrival direction of air-shower (see Fig. 5.18).

Concluding this study, one can state, that for the Tunka-Rex setup, which measures in a zenith angle range of about 30–50° and energy range of 0.1–1.0 EeV, the systematic uncertainties of the averaged parametrization are not larger than other uncertainties.

5.4.4. Influence of background

Due to the absolute calibration of the Tunka-Rex antenna stations, it is possible to add realistic noise samples to CoREAS simulations. This is done to estimate the influence of the background on the reconstruction resolution. The dataset described in the present Chapter and a library of noise measured by Tunka-Rex were used as input. For reconstruction, the process and quality cuts described in next Chapter were used, as well as the LDF treatment.

5. Lateral distribution of the radio emission

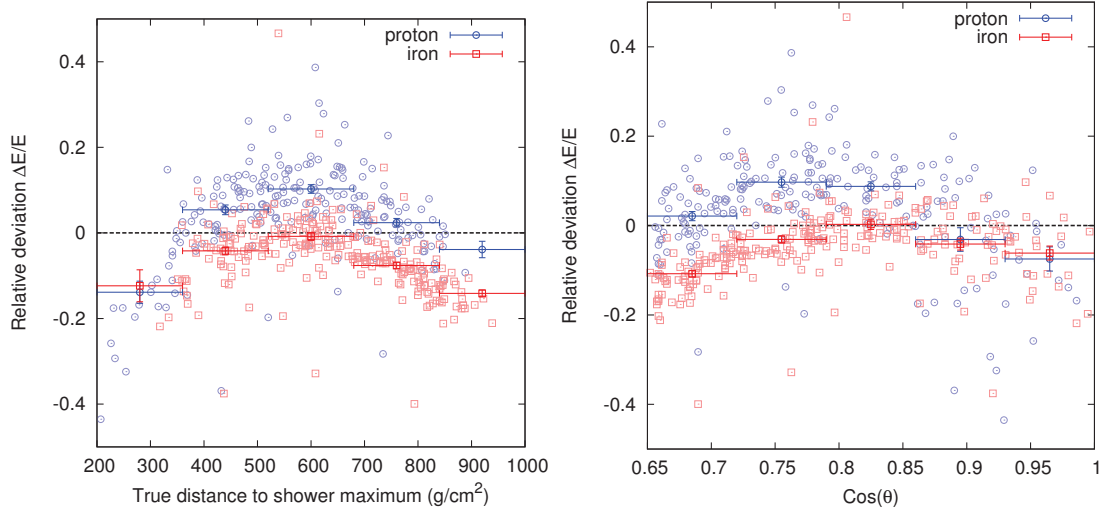


Figure 5.17.: Dependence of the primary-energy reconstruction on the distance to shower maximum (*left*) and zenith of arrival direction (*right*). One can see that the energy is underestimated for air-showers very close or very distant to the observer (i.e. with small or large geometrical distance to the shower maximum). The shift between proton and iron primaries is explained by the different energy content in the electromagnetic shower component.

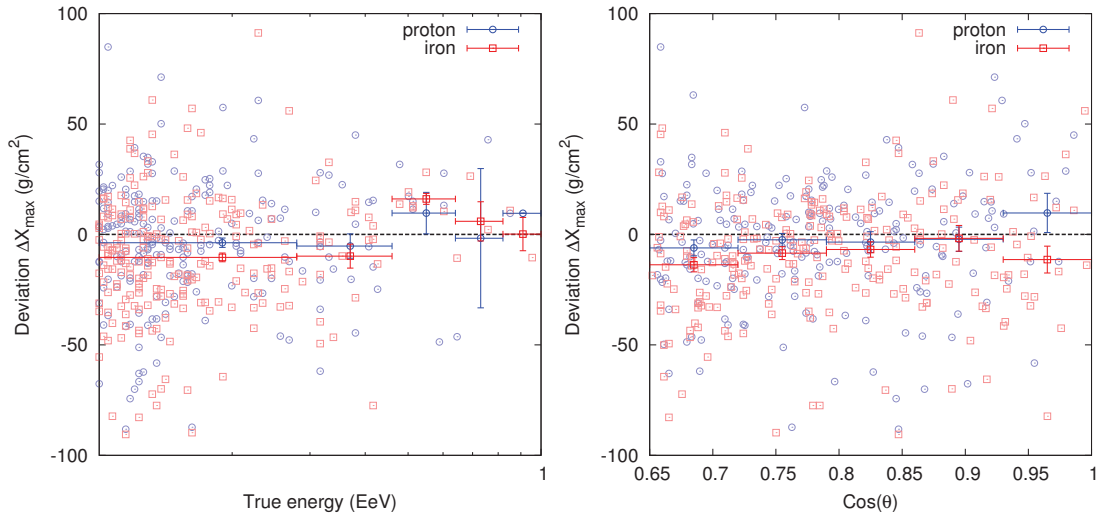


Figure 5.18.: Dependence of the shower-maximum reconstruction on the primary energy (*left*) and zenith of the arrival direction (*right*). One can see, that there is no difference between primaries, and no other correlation.

The obtained results show that noise has small influence on energy reconstruction after usual quality cuts. The average precision is about 10–15% compared to < 10% without background. However, these quality cuts have significant impact on the shower maximum reconstruction. First, almost all low-energy events are deselected decreasing the statistics

Simulations with realistic background

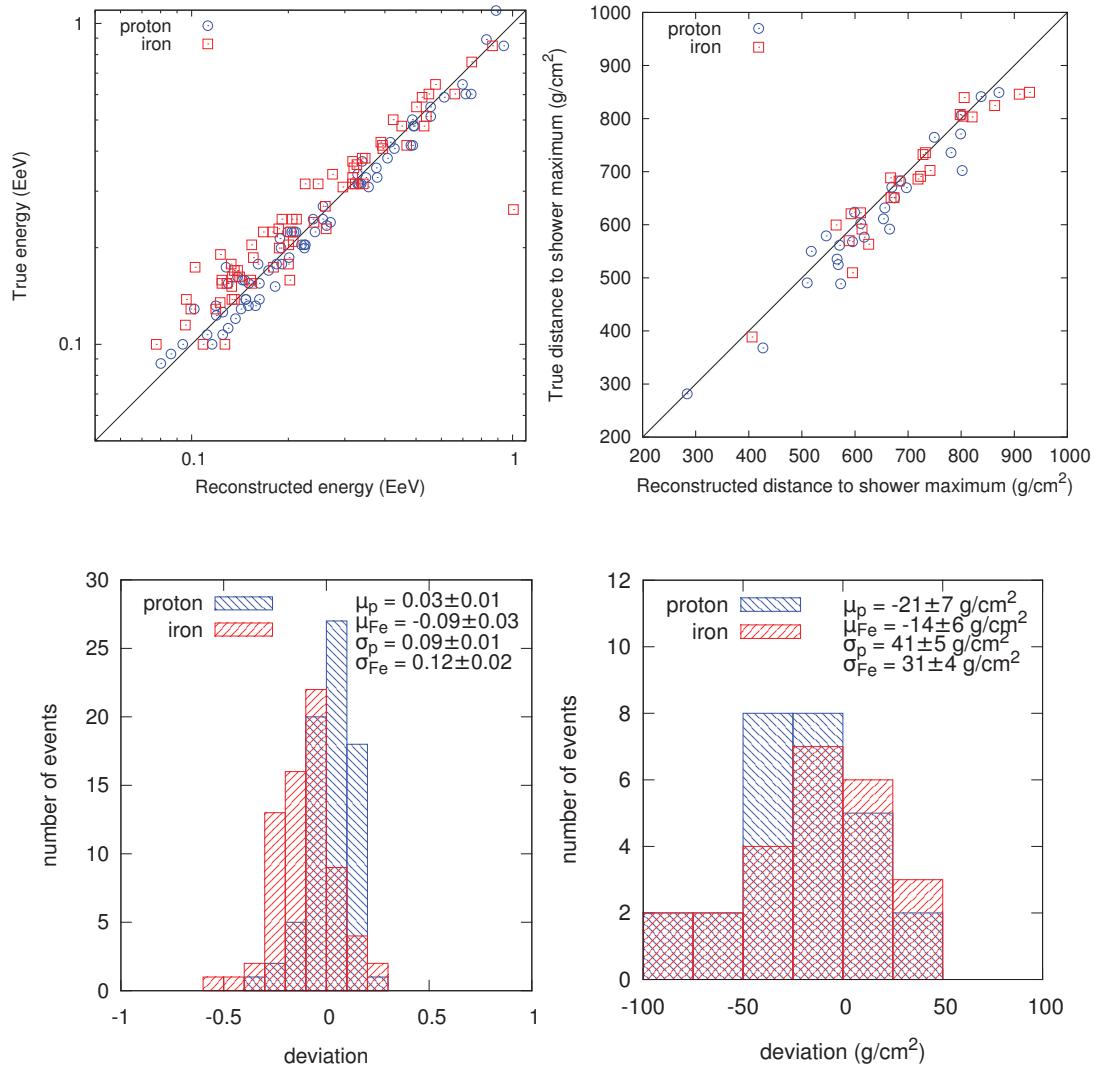


Figure 5.19.: Comparison between true and reconstructed primary energy and shower maximum of the CoREAS simulations after adding background samples.

of the dataset. Second, the resolution of the shower maximum reconstruction is slightly worse, 30–40 g/cm² instead of 25 g/cm². These values are in reasonable agreement with measured data. The results are shown in Fig. 5.19.

6. Measurement of energy and shower maximum

The data reconstruction procedure consists of two different parts: a mostly hardware-related part (data acquisition, signal reconstruction, rejection of false positives, etc.) and a high-level part for quality cuts and reconstruction of air-shower parameters. The hardware part is described in Chapter 4. The air-shower reconstruction is based on the model described in Chapter 5. One of the important parts of this procedure, which is not described in the present work, is the absolute calibration of the Tunka-Rex antenna stations. Details on the calibration are described in Refs. [72, 133].

The present Chapter describes additional steps necessary for the reconstruction of air-shower parameters for measured data. The influence of the background is investigated, and methods for background reduction are developed and discussed. Then, the quality cuts necessary for this low-statistic (i.e. small number of antenna stations per event) analysis are defined.

The data acquired in 2012-2014 is analyzed and discussed. The summary and conclusion of the analysis results are given in the end of the present Chapter. An important difference between the Tunka-Rex analysis and results of other experiments performing hybrid measurements with different detector systems on ground is adherence to the paradigm of a semi-blind analysis.

6.1. Concept of semi-blind analysis

From the very beginning the Tunka-Rex collaboration decided to follow a semi-blind analysis concept: at least two different datasets with sufficient statistics should be measured. Naturally, the first (2012/2013) and second (2013/2014) seasons of Tunka-133/Tunka-Rex measurements were chosen as Tuning and Prediction seasons, respectively.

For the Tuning season the full reconstruction provided by Tunka-133 was open: a list of events with air-shower coordinates (arrival direction and core position) and the reconstruction of energy and shower maximum were available. This data of the Tuning season was used for

- Checking the performance of the Tunka-Rex detector and estimate its efficiency.
- Tests of the hardware and antenna calibration.
- Performing realistic simulation and comparing measured amplitudes with theoretical predictions.
- Definition of reconstruction parameters, which can not be predicted theoretically due to instrumental uncertainties (e.g. threshold SNR, time windows, etc.), and have to be determined by studying the measured traces.
- Developing and testing methods for rejection of false positive signals and events.

The Tunka-133 reconstruction of the Prediction season was partly hidden, namely the energy and the shower maximum reconstruction, in order to prevent implicit tuning of the

Table 6.1.: Open and hidden parameters for the Tuning and Prediction seasons: list of parameters given by Tunka-133. The main air-shower parameters defining the primary particle (i. e. primary energy and shower maximum) are hidden for the Prediction season.

Property	Tuning season	Prediction season
Raw data	open	open
List of event timestamps	open	open
EAS arrival direction	open	open
EAS Core position	open	open
Energy reconstruction	open	hidden
Shower maximum reconstruction	open	hidden

Tunka-Rex methods and guarantee an independent cross-check of the developed methods. The geometrical properties of air-showers (i.e. core direction and position) are still important, because they are used for performance tests and troubleshooting. A summary of the open and blinded properties is presented in Table 6.1.

6.2. Pre-reconstruction improvements

The main issue making real data different from simulations is background. Tunka-Rex is faced with three main difficulties arising from the influence of various background sources:

- The energy content of noise is estimated by the SNR (signal-to-noise ratio). In addition, noise carries unknown random phase, i.e. the phases of the signal are distorted by it. This means, signal is changed non-linearly, and gains uncertainty, which leads to uncertainty of the reconstruction of air-shower properties.
- On the other hand, the SNR cut $\text{SNR}_{\text{th}} = 10$ removes only 95% of the false positive signals, which means, that some disturbances can pass the SNR cut and are treated as true signal.
- Below the SNR threshold the signal becomes indistinguishable from background, and, consequently, antenna stations with these signals are rejected. This reduces the number of the antennas per event, especially when the detector operates near the lower threshold. For events with a small number of points in the lateral distribution, the possibility of the LDF fit converging to a false minimum is increased.

For these reasons one has to take into account the noise. Corrections for the noise and restrictions to the lateral distribution were developed.

6.2.1. Amplitude correction for noise

As mentioned before, noise introduces additional power to the signal depending on the SNR. By adding measured noise to simulations, it was found, that at the threshold $\text{SNR}_{\text{th}} = 10$ the measured signal differs in order of 20% from the signal of the simulations. This means, that an amplitude adjustment is necessary in this low amplitude regime. To parameterize

the necessary amplitude adjustment, the simulation set R-SET (see Section 5.2) was used. Noise samples measured by the Tunka-Rex detector were used to study the noise influence (the description of noise measurements can be found in Section 4.3). The standard Tunka-Rex reconstruction procedure was run several times for each simulated primary particle (proton and iron) to obtain two different datasets:

- The first dataset contains events reconstructed without adding a noise, but all filters still have been applied.
- The second dataset contains events reconstructed after adding noise samples and using the standard Tunka-Rex reconstruction procedure.

The amplitudes from the first dataset are considered as true amplitudes A_t . The amplitudes of the second dataset can be considered like measured amplitudes, and are named A_m . After the reconstruction events of the first dataset have been selected, which coincide with the events of the second dataset, and the fractions A_m/A_t are calculated as a function of SNR.

$$A_t = f(x)A_m, \quad (6.1)$$

Here $x = \text{SNR}_{\text{th}}/\text{SNR}$, i.e. the definition domain of $f(x)$ is $(0; 1]$. The zero value of the function is $f(0) = 1$, because it corresponds to infinity high SNR and negligible noise influence.

The general form of the amplitude and phase of the signal after adding noise is

$$A_m e^{i\varphi} = A_t e^{i\varphi_t} + A_n e^{i\varphi_n}, \quad (6.2)$$

where A_m, A_t, A_n are the amplitudes of the measured signal, true signal, and noise, respectively, and $\varphi_m, \varphi_t, \varphi_n$ are their phases. Consequently, the power of the amplitude takes the form

$$A_m^2 = A_t^2 + A_n^2 + A_t A_n (e^{i(\varphi_t - \varphi_n)} + e^{-i(\varphi_t - \varphi_n)}) \quad (6.3)$$

Averaging the left and the right part of the equation, one obtains

$$\langle A_m^2 \rangle = \langle A_t^2 \rangle + \langle A_n^2 \rangle, \quad (6.4)$$

assuming random, uncorrelated noise the expectation value of the interference term is zero

$$\langle (e^{i(\varphi_t - \varphi_n)} + e^{-i(\varphi_t - \varphi_n)}) \rangle = 0. \quad (6.5)$$

The same assumption was used by Allan [154] and in a LOPES analysis [155] (except for very low SNRs).

To correct for the power introduced by noise, a common relation is [155]

$$f(x) = \sqrt{1 - kx}. \quad (6.6)$$

Since the amplitude of the signal and noise can be defined differently, in the general case, and in particular for Tunka-Rex, $k \neq 1$. The parameter k is extracted from a fit to simulations. The values for proton and iron are within the fitting uncertainties and the average value is $k = 4.10$. The corresponding distribution is shown in Fig. 6.1.

It is interesting to note that until recently, Tunka-Rex used a sliding median filter [156] for the suppression of narrow peaks in the frequency domain instead of directly setting the amplitude at some fixed frequencies to zero. On the one hand, the median filter is more flexible when the background spectrum is not well-known, and when there is a high probability of transient narrow-band noise. On the other hand, the median filter affects the signal in a non-linear way. The correction for this is non-trivial, and the behavior is not well explained at the moment. For these reasons, it was decided to abandon this filter.

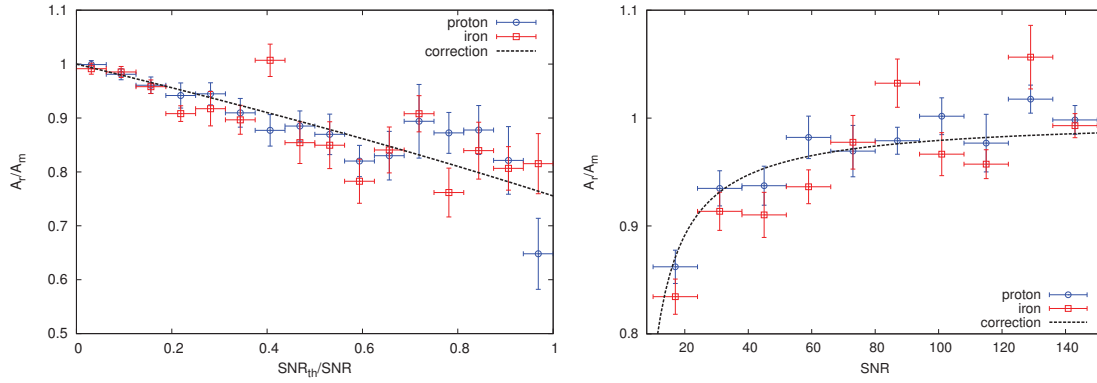


Figure 6.1.: Fraction between true (A_t) and measured (A_m) amplitudes after adding noise. The dotted line shows the correction function developed for Tunka-Rex. Both plots show the same information, but in different domains, a domain described in the present Section, $x = \text{SNR}_{\text{th}}/\text{SNR}$ (left), and a linear domain, $x = \text{SNR}$ (right).

6.2.2. Rejection of false positive signals

The threshold value $\text{SNR}_{\text{th}} = 10$ was defined in order to have less than 5% of false positive signal at antenna stations passing this cut. In the present Section another cut, which rejects false positive signals exploiting the information of the lateral distribution, is described. Since for the data analysis of Tunka-Rex the core reconstruction given by the air-Čerenkov detector Tunka-133 is used, in the first step a pre-reconstruction directly using the arrival direction and core position of Tunka-133 is performed: the lateral distribution of the radio amplitudes against distance is checked for outliers. Sometimes this distribution contains so-called “gaps”: antenna stations not passing the SNR cut can appear between two antenna stations with signal. If the size of this “gap” is larger than 1 station, then all antennas stations with signal beyond the “gap” are considered as false positives (see Fig. 6.2). This cut is based on a simple feature of the lateral distribution of radio amplitudes: after the Čerenkov-like bump (≈ 150 m from the shower axis), the signal strength falls approximately exponentially, at least after correction for the azimuthal asymmetry, which is applied here (cf. Section 5.3).

6.2.3. Optimization of the lateral distribution function

As mentioned, due to the refractive index the lateral distribution of radio amplitudes has Čerenkov-like features. The simplest function describing this features, in particular the possible bump at $r \approx 150$ m has the form (see Chapter 5)

$$\mathcal{E}_2(r) = \mathcal{E}_{r_0} \exp(a_1(r - r_0) + a_2(r - r_0)^2), \quad (6.7)$$

where r is the distance to shower axis, and the parameters a_1 and a_2 describe the steepness of the LDF slope and the width of the Čerenkov bump, respectively. The position of this bump is given by combination of a_1 and a_2 (see Eq. (5.28)).

A problem arising from this parameterization is connected to the number of antenna stations per event (histogram of this distribution in Fig. 6.3). Half of the events contains only

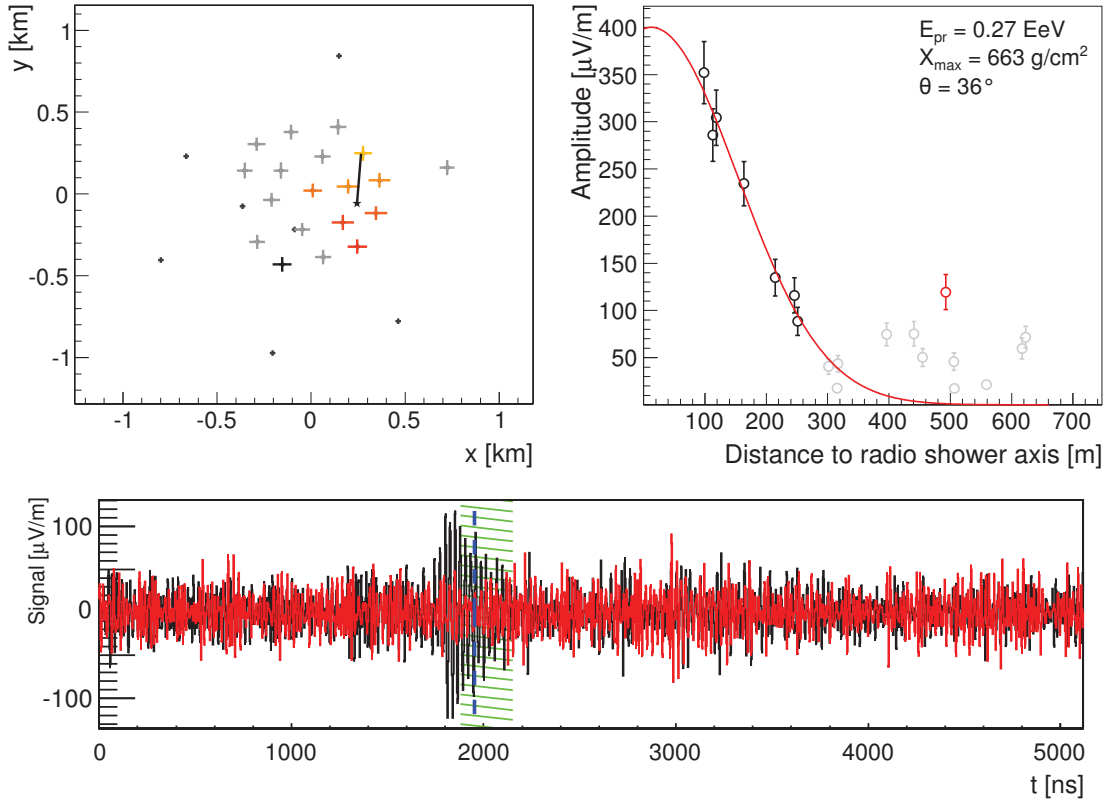


Figure 6.2.: Example event with rejected antenna station.

Left: Tunka-133 array with highlighted antenna stations. Color and size indicate arrival time and amplitude, respectively.

Right: Lateral distribution of signals with respect to the distance to the shower axis. The antenna station in red color is rejected as outlier, since before it at least two antenna stations with signal did not pass the SNR cut.

Bottom: Signal trace of rejected antenna station. One can see that RFI accidentally appeared in the signal window (green shaded area) and is misrecognized as a true signal (blue dashed line). Since the current data analysis does not feature sophisticated signal recognition, the rejection of outliers in the lateral distribution is an effective method to increase the purity of the data.

3 antenna stations, which means that these events cannot be used for $\mathcal{E}_2(r)$ fitting, because fitting of three free parameters requires at least four stations. The reason for the large number of 3-station events is not only the threshold, but also the geometry: high energy events detected on the border of the array contain also a small number of antenna stations. Even if deselecting all events with number of antenna stations less than 4, one collides with the next problem: a strong correlation between the parameters a_1 and a_2 . When the number of fitted points is close to the number of fit parameters, and the uncertainties of the single points in lateral distribution are large, the fit can converge to false minima, or give large uncertainties for the resulting parameters with strong correlation, like for the parameters a_1 and a_2 . Unfortunately, most of the Tunka-Rex events satisfy these conditions.

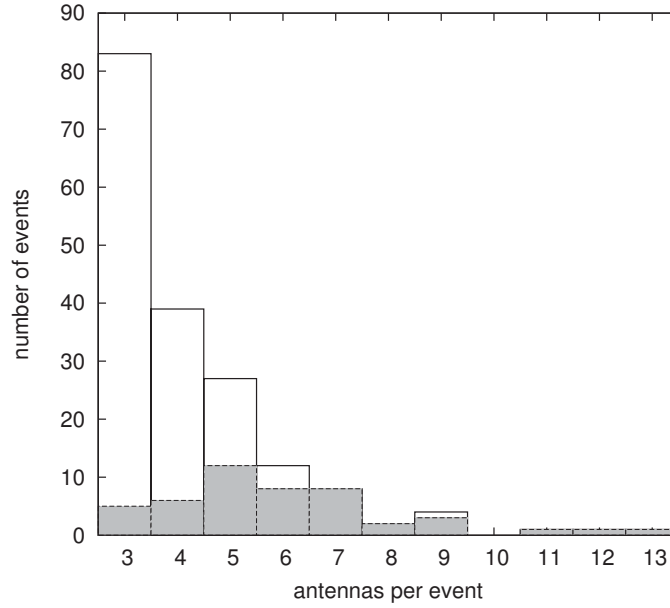


Figure 6.3.: Distribution of the antennas per event for the Tuning and Prediction seasons. The shaded area shows events surviving all quality cuts described in the present Chapter.

Let us return again to Eq. (5.28) and Fig. 5.13. From the plot one can see, that the width of the Gaussian (σ) depends only weakly on the distance to shower maximum. The distance to the shower maximum depends on the the shower maximum itself, the zenith angle of the arrival direction (namely $D_{\max} = H_{\max} / \cos(\theta)$, where H_{\max} and D_{\max} are the geometrical height of the shower maximum and the distance to it in meters, respectively, and θ is the zenith of the air-shower arrival direction), and, in second order, of primary energy (high-energy air-showers penetrate deeper to the atmosphere).

Of course, one has no information on the shower maximum before fitting the lateral distribution function Eq. (6.7), but still one can probe with simulations the correlation with other air-shower properties, particularly, the zenith angle of the arrival direction. These correlations are shown in Fig. 6.4. From this Figure one can learn, that a_1 correlates with zenith as expected (due to the correlation with distance to shower maximum), and a_2 shows no strong correlation. Therefore, one can try to fix or somehow parameterize a_2 as function of primary energy and zenith angle: these are the two parameters possible influencing the lateral distribution function. Thus, events from the R-SET were binned by primary energy, and mean values of a_2 were calculated for each bin. Due to low statistics, a_2 was parameterized with the following simple form

$$a_2(\theta, E_{\text{pr}}) = a_{20}(E_{\text{pr}}) + a_{21}(E_{\text{pr}}) \cos \theta, \quad (6.8)$$

$$a_{20} = a_{200} + a_{201} E_{\text{pr}}, \quad a_{21} = a_{210} + a_{211} E_{\text{pr}}, \quad (6.9)$$

where the parameters a_{200} , a_{201} , a_{210} , a_{211} were obtained from the profile fit (see Fig. 6.5). Their values are given in Table 6.2. The primary energy E_{pr} for this parameterization is estimated with a simple exponential LDF $\mathcal{E}_1(r)$ after correction for the azimuthal asymmetry, since it was shown, that the simple exponential function provides a good energy estimator (almost as good as the one presented here, c.f. Appendix C) [72].

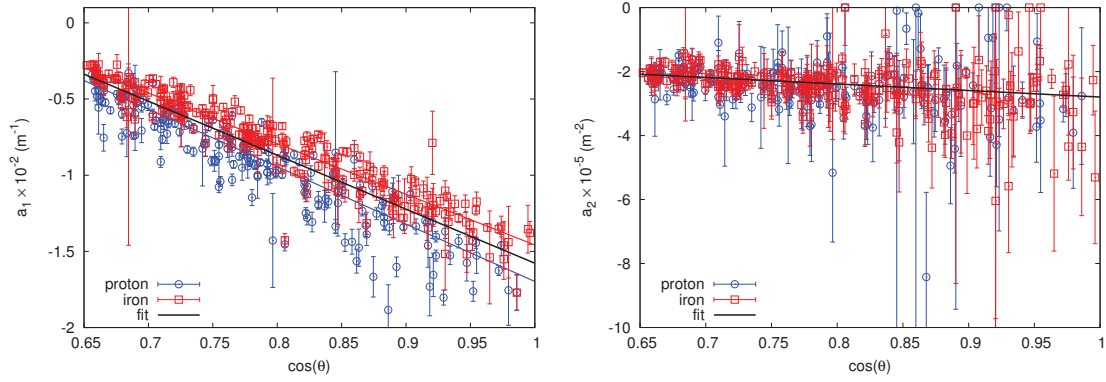


Figure 6.4.: Correlation of LDF parameters with cosine of the zenith angle of the arrival direction for CoREAS simulations

Left: One can see a strong correlation between a_1 and $\cos(\theta)$, caused by the correlation of a_1 with the distance to the shower maximum, which is antiproportional to $\cos(\theta)$.

Right: Since the parameter a_2 depends only weakly on the distance to the shower maximum, one does not expect any strong correlation with $\cos(\theta)$, as confirmed by the plot.

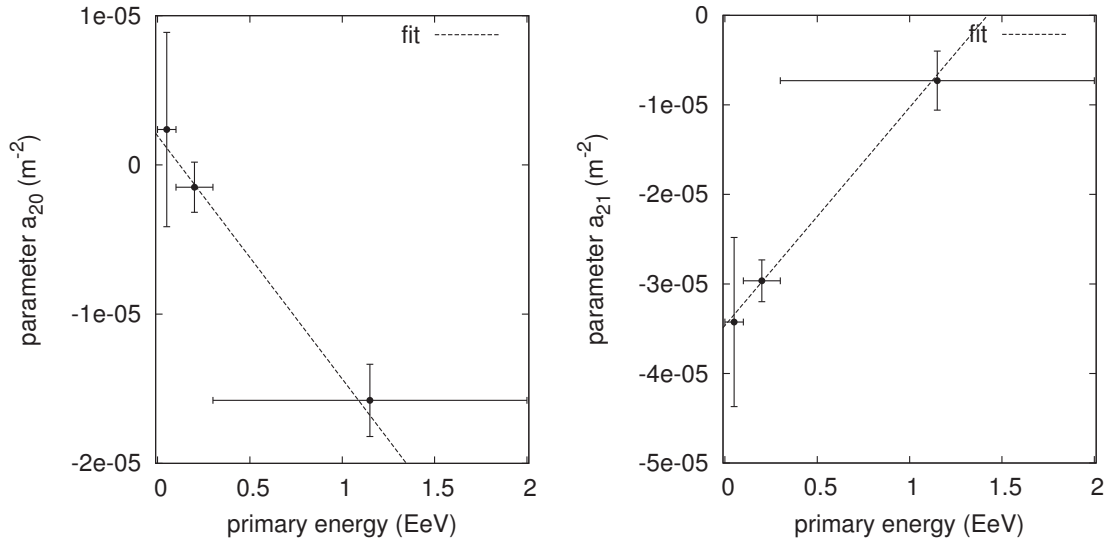


Figure 6.5.: Dependence of the parameters a_{20} (*left*) and a_{21} (*right*) in the primary energy. Since simulations are done in a limited energy interval, the range was divided in three bins only, whose width is the size of the horizontal bars.

Table 6.2.: Parameters for Eq. (6.9) for a_2 coefficient in LDF

Parameter	Value
a_{200}	$0.19 \cdot 10^{-5} \text{ m}^{-2}$
a_{201}	$-1.63 \cdot 10^{-5} \text{ m}^{-2}/\text{EeV}$
a_{210}	$-3.45 \cdot 10^{-5} \text{ m}^{-2}$
a_{211}	$2.44 \cdot 10^{-5} \text{ m}^{-2}/\text{EeV}$

6.2.4. Concluding remarks

Summarizing the methods for improvement of the data quality discussed in the present Section, the following statements can be made: generally, only the most important features were taken into account, however, they already give a significant increase in the purity of data. There are also additional hardware-related routines, e.g. rejection of broken or saturated antenna station not explained here. Still there are several improvements which can be implemented further to increase the purity and statistics. A brief description of some ideas is given below, which can be tested in future:

- Floating noise window. Since not all of the RFI is filtered by the applied bandstop filter, some RFI can accidentally be present in the noise window. Thereby, the RMS in the noise window gets higher, and antennas do not pass the SNR cut because of the threshold for this event becomes too high. Probing noise in different windows (of the same size) could lead to elimination of these cases.
- Narrowing the signal window. Knowing the arrival direction of the air-shower, one could narrow the time window by one third, which will decrease the detection threshold.
- Polarization cut. A more sophisticated treatment of the radio signal would imply probing of the polarization components. Assuming a constant contribution from the charge excess, the polarization vector with respect to shower axis can be predicted. Comparing predicted and measured polarization, one can define the quality of the signal and reject obvious false positive events. This cut will be applied at Tunka-Rex for the one-antenna analysis in Ref [133].

6.3. Quality cuts

Since the quality of the measured data is reduced by the influence of noise, it is necessary to apply additional cuts deselecting low-quality events. As it was shown many times before, for reconstruction of the energy it is sufficient to have one antenna station close to the shower axis. This automatically means, that this antenna station usually has a high SNR, and, consequently, high quality. Concerning the reconstruction of the shower maximum, one additional antenna station is required at a distance far from the shower axis, which requires the treatment of antenna stations with low SNR.

For this reason additional quality cuts are necessary for the reconstruction of the shower maximum, only. In case of Tunka-Rex, it is not possible to apply very strict quality cuts deselecting many events due to the low statistics. Still, the following two cuts are required to reach a certain precision ($\approx 40 \text{ g/cm}^2$) for the shower maximum.

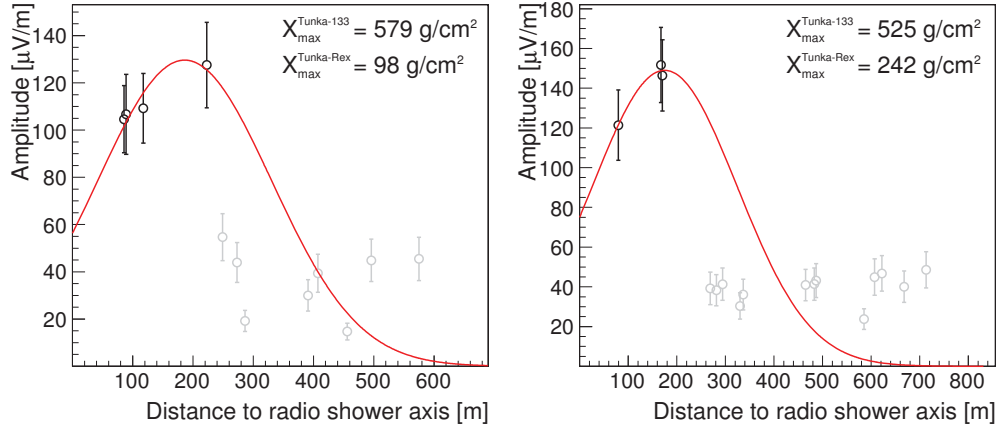


Figure 6.6.: Example events with underestimation of the slope of the lateral distribution. Due to the geometrical situation (all antenna stations are equidistant respect to the shower axis), the fitted parameters were obtained with large uncertainties propagating to uncertainties of shower-maximum reconstruction: $X_{\max} = 94 \pm 159 \text{ g/cm}^2$ (left) and $X_{\max} = 243 \pm 206 \text{ g/cm}^2$ (right). The reconstruction of this class of events could perhaps improved by a likelihood fit exploiting the information about antenna stations without significant signal (i.e. the LDF cannot be much larger than the threshold at a station without signal). Presently these events are deselected by the quality cut on the shower-maximum fit uncertainty.

The first quality cut is related to the slope reconstruction: since the slope of the lateral distribution is probed at the distance of 180 m (see previous Chapter), it requires at least one antenna at a distance further than 200 m from the shower axis. In Fig. 6.7 one can see, that otherwise events mostly have large fitting uncertainties, and the reconstructed shower maximum shows almost no correlation with Tunka-133.

The second quality cut concerns the reconstruction precision of the of shower maximum. Due to the theoretical predicted resolution of 40 g/cm^2 , the predicted difference between Tunka-133 and Tunka-Rex reconstruction is of $\sigma = \sqrt{\sigma_{\text{Cherenkov}}^2 + \sigma_{\text{theor}}^2} \approx 50 \text{ g/cm}^2$, where $\sigma_{\text{Cherenkov}} \approx 30 \text{ g/cm}^2$ [43]. Thus, a quality cut on the Tunka-Rex fitting uncertainty of 50 g/cm^2 was also applied. Moreover, it was found, that events having larger uncertainties, have a trend to underestimate the slope (see Fig. 6.6), which leads to overestimation of the distance to the shower maximum (see Fig. 6.7). A summary of the event statistics after applying selection and quality cuts is shown in Table 6.3. The example events, which survived the quality cuts are given in Appendix E.

6.4. Reconstruction of the full dataset

The first result presents the distribution of arrival directions and cores of the detected air-showers¹. It is important to note that the efficiency of the radio detector strongly depends on the zenith and geomagnetic angles (see Fig. 6.8) and core position (see Fig. 6.9). A

¹Parts of this Section have been published in JCAP [157].

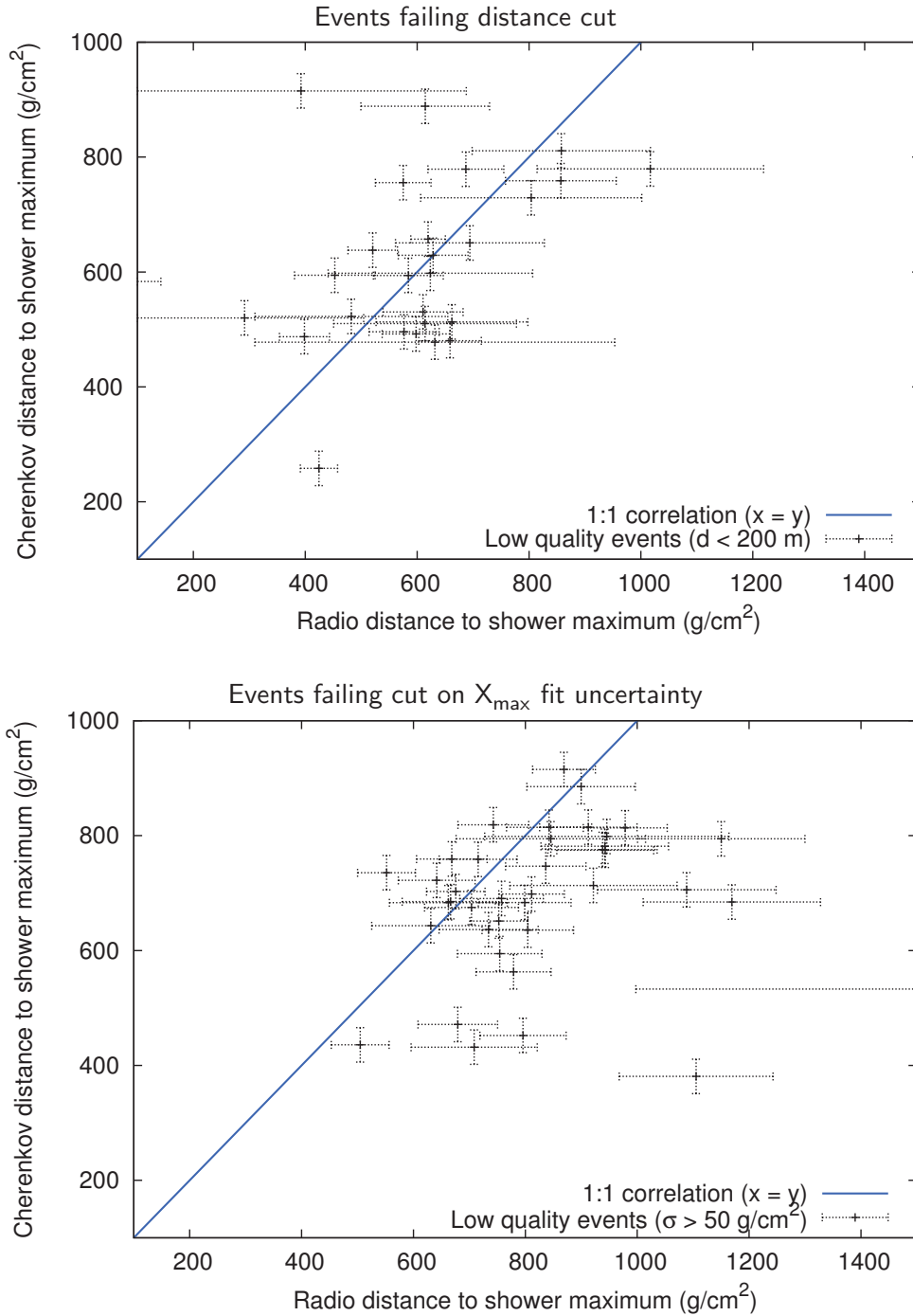


Figure 6.7.: Different types of low-quality events (rejected by quality cuts).

Top: Events without antenna stations further than 200 m from shower axis. The slope of the lateral distribution cannot be reconstructed accurately.

Bottom: Events with large fitting uncertainties. These events are trending to underestimate the slope, consequently, overestimating the distance to the shower maximum. Example events and explanation is given in Fig. 6.6.

Table 6.3.: Statistics of events in both seasons after selection and quality cuts.

Number of events	Tuning season	Prediction season
≥ 3 stations with signal	244	445
rejecting outlier stations in LDF	124	147
\angle (Tunka-Rex, Tunka-133) $\leq 5^\circ$	91	87
Additional cuts for X_{\max} reconstruction		
at least one antenna at $d_{\text{axis}} > 200$ m	64	56
$\sigma(X_{\max}) \leq 50$ g/cm ²	25	22

detailed investigation of the efficiency is done in Ref. [133].

The asymmetry in the arrival distributions are in agreement with the geomagnetic nature of the radio emission. The efficiency of the detector increases with decreasing zenith angles because of a number of geometrical effects. The first effect is connected to the direction of the geomagnetic field in the Tunka Valley: since it is almost vertical, the power of the emission increases for inclined showers due to increasing geomagnetic angle α_g (i.e. the angle between magnetic field and shower axis). The second effect is that the footprint increases with inclination, which is important for sparse arrays with large spacing, like Tunka-Rex. The third effect is connected to the radio emission and propagation: the atmosphere is transparent for the radio waves, and the emission power increases until the electromagnetic component of the air-shower is fully absorbed (horizontal air-showers are not clipped and should produce more radio emission than vertical ones).

The distribution of the shower cores is almost homogeneous inside the inner dense array and has a steep cut-off outside. The small inhomogeneity can be explained by technical artifacts: TREX-18 (18 antennas in the Prediction season) has two gaps at clusters 2 and 4, and the southern part of the detector suffers from slightly stronger background due to infrastructure buildings there.

There are some differences between both seasons, which, as was expected, should not change the reconstruction procedure (of course, if reconstruction methods were developed in a proper way). The first difference is the effective measurement time, which, is almost the same: 280 h and 260 h for the Tuning and Prediction seasons, respectively. The second difference is the geometrical configuration of the detector: TREX-18 has two gaps at cluster 2 and 4, and only one antenna at a satellite cluster. TREX-25 has antennas attached to each cluster center of Tunka-133. As it will be shown later, this difference introduces additional systematic effects and requires additional cuts. Since the effective measurement time and an event rates are very similar for both seasons, one observes similar energy and X_{\max} distributions for them (Fig. 6.10)

6.4.1. Energy reconstruction

Let us consider the air-shower reconstruction in detail. After standard selection cuts, the energy was reconstructed for 91 and 87 events for the Tuning and Prediction seasons, respectively. The mean relative deviations from the Tunka-133 reconstruction are 0.19 ± 0.03 and 0.18 ± 0.03 , respectively. The distributions of the events are shown in Figs. 6.11 and 6.12. The mean value of the histogram indicates that the correlation between energies reconstructed by the air-Čerenkov and radio detectors is close to 1:1. To study reconstruc-

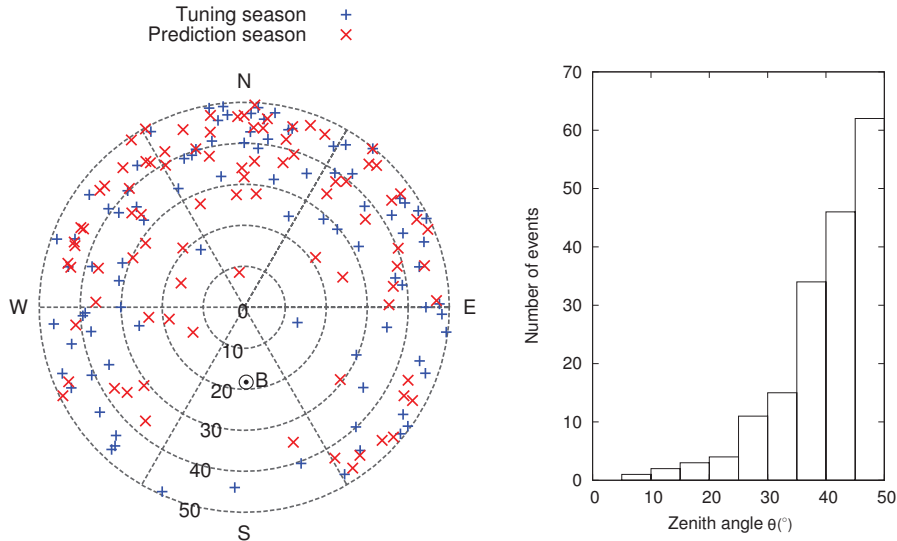


Figure 6.8.: Angular distribution of arrival directions.

Left: Skymap of arrival directions of air-showers. The empty spot around the magnetic field vector (marker **B**) is due to the suppression of the geomagnetic component of the radio emission (i.e. small geomagnetic angles α_g).

Right: Distribution of zenith angles of arrival directions (for both seasons). The efficiency at small zenith angles is suppressed mainly due to small geomagnetic angles and steepness of the lateral distribution.

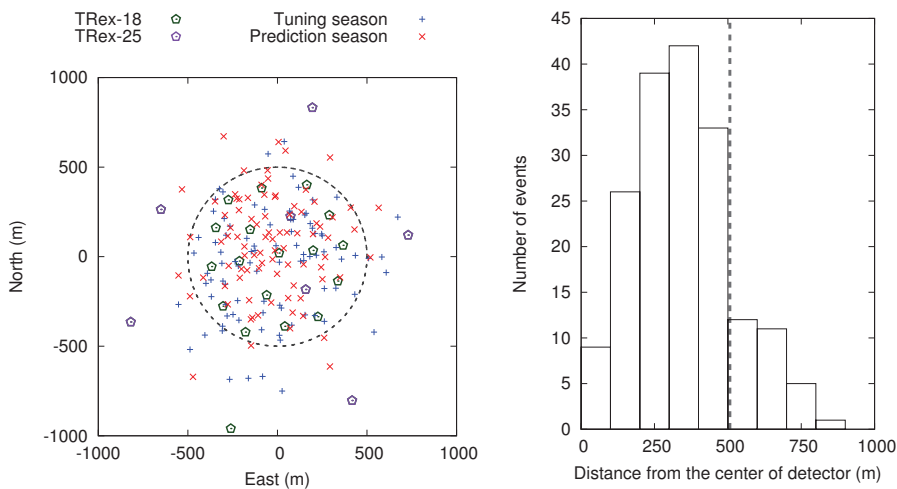


Figure 6.9.: Distribution of shower cores of detected events.

Left: Map of the shower cores. The circle ($r = 500$ m) indicates the border of the dense inner detector.

Right: Distribution of the events against distance to the center of the detector. The number of events increases with the distance (due to increasing area) until about 500 m. Beyond this border of the dense inner detector at 500 m, the number of events falls rapidly.

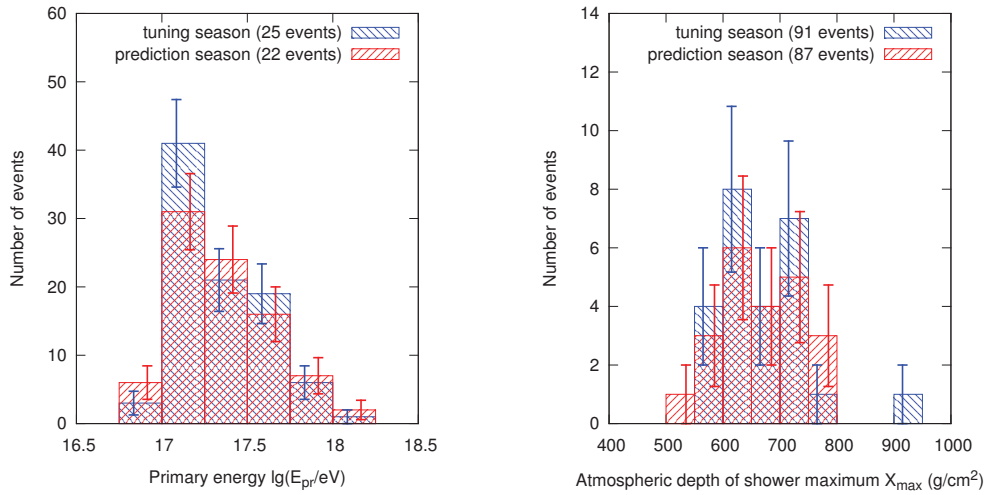


Figure 6.10.: Primary energy (*left*) and atmospheric depth of shower maximum (*right*) distributions reconstructed with Tunka-Rex for Tuning and Prediction seasons.

tion uncertainties, the correlations in the Fig. 6.11 are fitted with a function

$$E_{\text{pr}}^{\text{Tunka-133}} = k_e E_{\text{pr}}^{\text{Tunka-Rex}}. \quad (6.10)$$

The coefficient k_e contains the uncertainty of the correlation propagated from the uncertainties of the energy reconstruction, within the uncertainties, k_e is comparable with 1m which is expected for 1:1 correlation of the Tunka-Rex and Tunka-133 energy reconstructions. The results are summarized in the Table 6.4.

6.4.2. Shower maximum reconstruction

The procedure for the shower maxima is similar to the one for energy reconstruction. Applying the high quality cuts described in the previous section for the Tuning and Prediction seasons, 25 and 22 events were obtained, respectively. The results are presented in Figs. 6.13 and 6.14. The correlations of Fig. 6.13 were fitted with a function

$$DX_{\text{max}}^{\text{Tunka-133}} = k_x (DX_{\text{max}}^{\text{Tunka-Rex}} - \langle DX_{\text{max}} \rangle) + b_x + \langle DX_{\text{max}} \rangle, \quad (6.11)$$

where DX_{max} is the distance to the shower maximum, and the coefficient b_x is a systematic shift between the depths reconstructed by the different detectors at the mean distance $\langle DX_{\text{max}} \rangle = 650 \text{ g/cm}^2$.

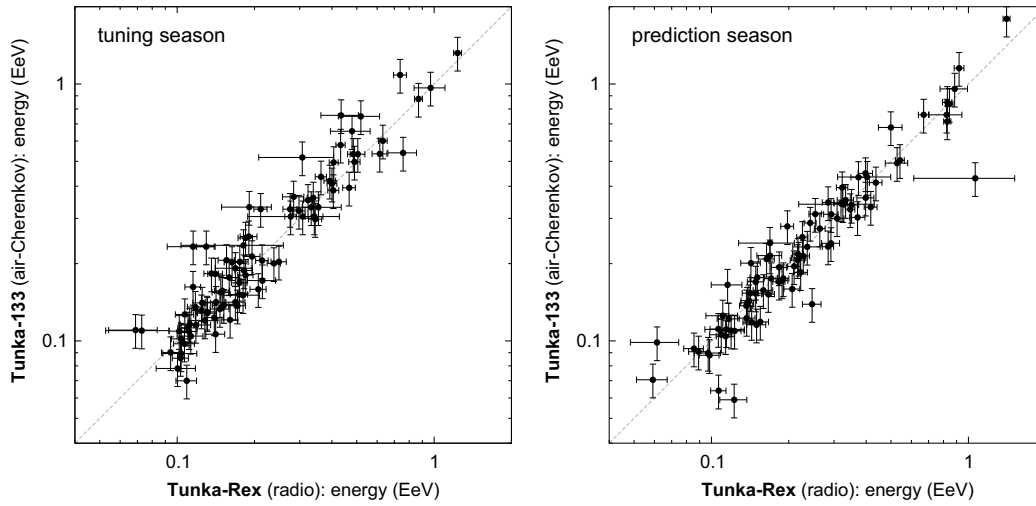


Figure 6.11.: Correlation of the shower energy reconstructed with Tunka-Rex radio and Tunka-133 air-Cherenkov measurements for Tuning and Prediction seasons.

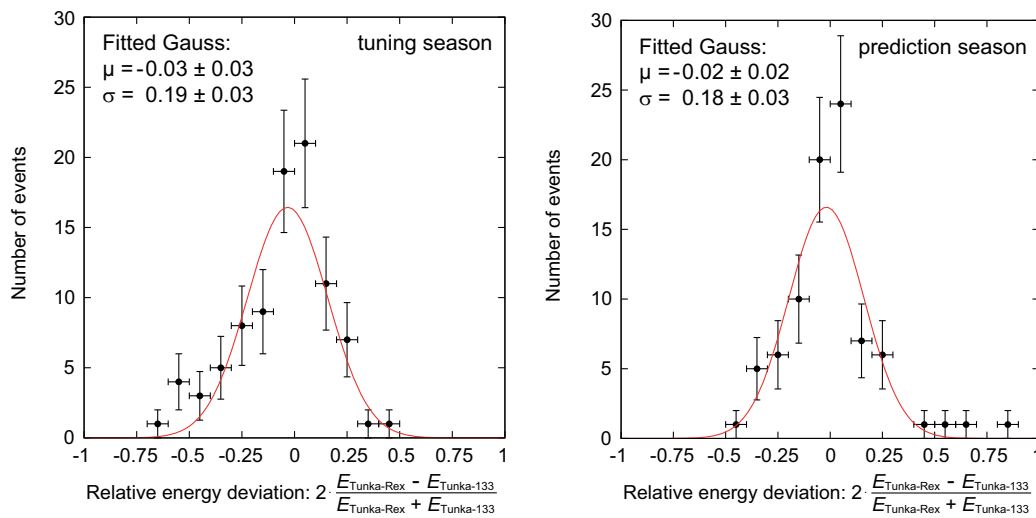


Figure 6.12.: Histograms of the relative deviation (i.e. difference divided by average) between the Tunka-133 and Tunka-Rex energy reconstructions for the Tuning and Prediction seasons.

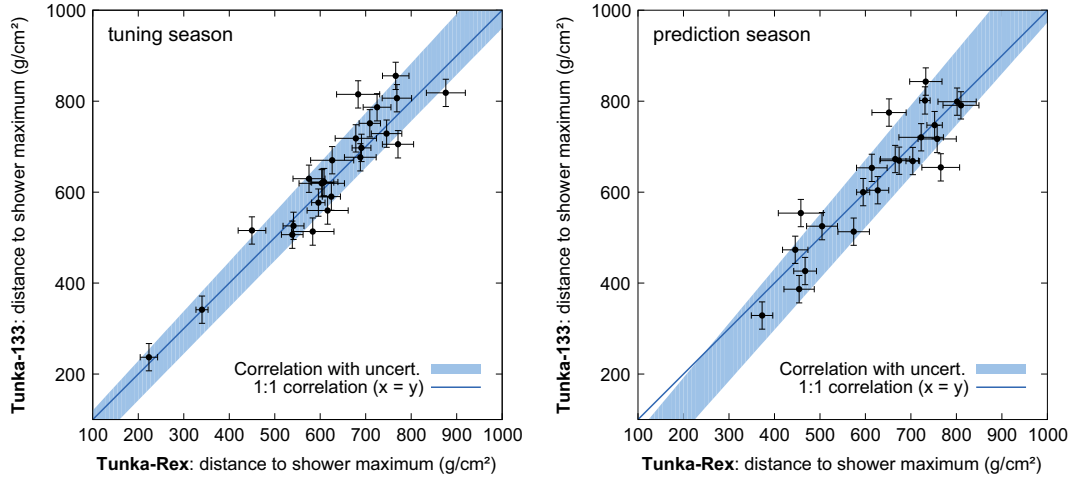


Figure 6.13.: Correlation of the distance to shower maximum as reconstructed with Tunka-Rex radio and Tunka-133 air-Cherenkov measurements for the Tuning and Prediction seasons

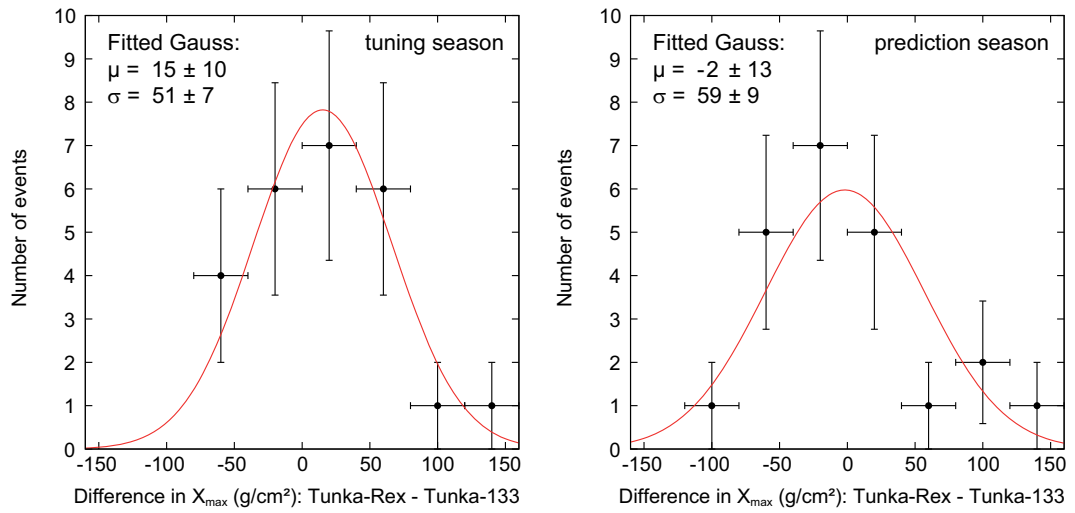


Figure 6.14.: Histograms of the difference between the Tunka-133 and Tunka-Rex shower maximum reconstructions for the Tuning and Prediction seasons.

Table 6.4.: Summary of the cross-check between the air-shower reconstructions of Tunka-133 and Tunka-Rex (measurements in 2012-2014)

Property	Tuning season	Prediction season
Effective time of measurements (hours)	280	260
Number of antennas	18	25
Energy reconstruction		
Number of events	91	87
Standard deviation σ_e	0.19 ± 0.03	0.18 ± 0.03
Mean offset μ_e	-0.03 ± 0.03	-0.02 ± 0.02
Correlation slope coefficient k_e	1.02 ± 0.02	0.96 ± 0.02
Shower maximum reconstruction		
Number of events	25	22
Standard deviation σ_x (g/cm^2)	51 ± 7	59 ± 9
Mean offset μ_x (g/cm^2)	15 ± 10	-2 ± 13
Correlation slope coefficient k_x	1.06 ± 0.06	1.16 ± 0.08
Correlation shift coefficient b_x (g/cm^2)	-11 ± 9	5 ± 9

In contrast to the results of the energy reconstruction, the reconstruction of the shower maximum shows a worse correlation with Tunka-133 data: the mean difference is $59 \pm 9 \text{ g}/\text{cm}^2$ in the Prediction season compared to $51 \pm 7 \text{ g}/\text{cm}^2$ in the Tuning season. As found after unblinding, there is a systematic uncertainty introduced by extending the geometrical layout of Tunka-Rex setup: the upgraded radio detector is more sensitive to events, which are beyond the dense array, i.e. at distances $r_0 > 500 \text{ m}$ from the array center. On the other hand there is no evidence, that Tunka-133 has the same precision for these outer events, especially, for the core position [43]. In addition, if Tunka-133 also has a large uncertainty for the slope of the Čerenkov-light LDF (and, consequently, for the shower maximum) reconstruction, then this could lead to a larger deviation from the Tunka-Rex prediction. Therefore, for the final analysis including the two years of measurements, an additional quality cut deselecting events outside of the inner dense detector was applied to the entire dataset. This analysis is described in the next section.

6.4.3. Merged dataset with additional cut

As described in the previous section, after unblinding a feature not visible in the data of the Tuning season was found: events detected outside of the inner dense array (see Fig. 6.9) have larger deviations of the shower maximum values reconstructed by the radio and air-Čerenkov detectors. The recent results reported by Tunka-133 have shown, that outer events have lower precision and must be excluded from mass-composition analysis [43]. To perform a merged analysis of both seasons, an additional quality cut is applied: events outside the inner part of the array were deselected, i.e. their reconstructed core distance $r_0 = \sqrt{x_0^2 + y_0^2} > 500 \text{ m}$, where x_0 and y_0 are the coordinates of the core in the local Tunka-133 coordinate system with the origin at the central PMT. As seen from the Fig. 6.9, the rate of the events falls steeply beyond the $r = 500 \text{ m}$. Thus, by applying this cut the efficiency of the radio detector is marginally decreased. For the X_{max} reconstruction 42 of 47 events survive this cut. This does not mean, that the satellite antenna stations are

Table 6.5.: Summary of dataset merged of both seasons (2012-2014) reconstruction with additional quality cut excluding outer events

Property	Value for 2012-2014
Effective time of measurements (hours)	540
Number of antennas	18 to 25
Energy reconstruction	
Number of events	148
Standard deviation σ_e	0.19 ± 0.02
Mean offset μ_e	0.00 ± 0.02
Correlation slope coefficient k_e	0.98 ± 0.01
Shower maximum reconstruction	
Number of events	42
Standard deviation σ_x (g/cm^2)	47 ± 5
Mean offset μ_x (g/cm^2)	-2 ± 7
Correlation slope coefficient k_x	1.07 ± 0.05
Correlation shift coefficient b_x (g/cm^2)	2 ± 6
Tunka-Rex precision (after subtraction of Tunka-133 resolution)	
Energy	15% incl. systematics (cf. Section 5.4.3)
Shower maximum (g/cm^2)	38

useless. They are still important for the estimation of different systematic effects and the sensitivity of the detector. Moreover, they could also become more important for inclined events not used in the present analysis.

The corresponding results are shown in Figs. 6.15 and 6.16. A summary of the analysis of two years after applying the core-position quality cut is presented in Table 6.5. It is apparent that the additional quality cut improves the reconstruction, and there is strong correlation for the shower maxima as well as for the energy.

Having unblinded the merged dataset, one can compare the distributions of the energy and shower maximum obtained by Tunka-Rex with the spectra for the same events given by the Tunka-133. The distributions are presented in Fig. 6.17. The energy distributions are in very good agreement. The distributions for the shower maximum have low statistics and are slightly different, but there is no significant discrepancy.

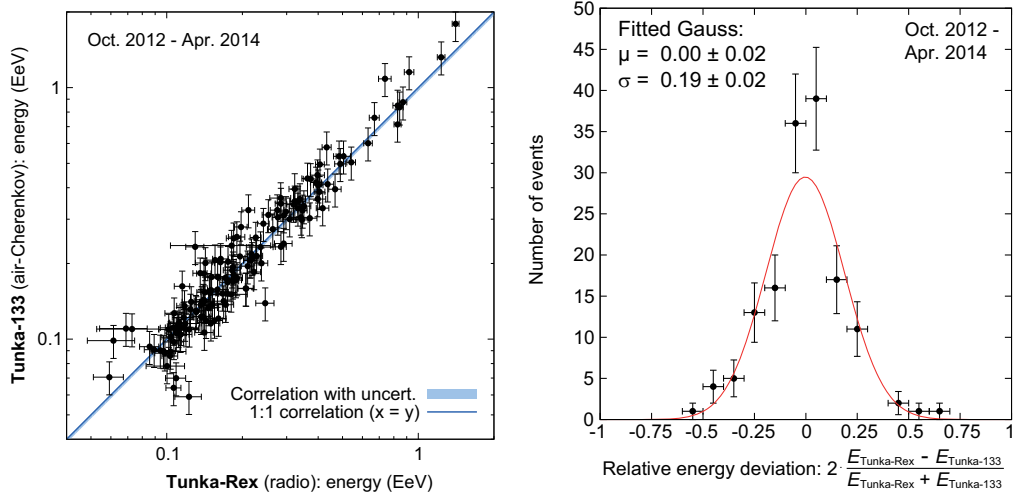


Figure 6.15.: Correlation of the shower energy reconstructed with Tunka-Rex radio and Tunka-133 air-Cherenkov measurements for the merged dataset (2012-2014) after applying additional quality cut excluding outer events.

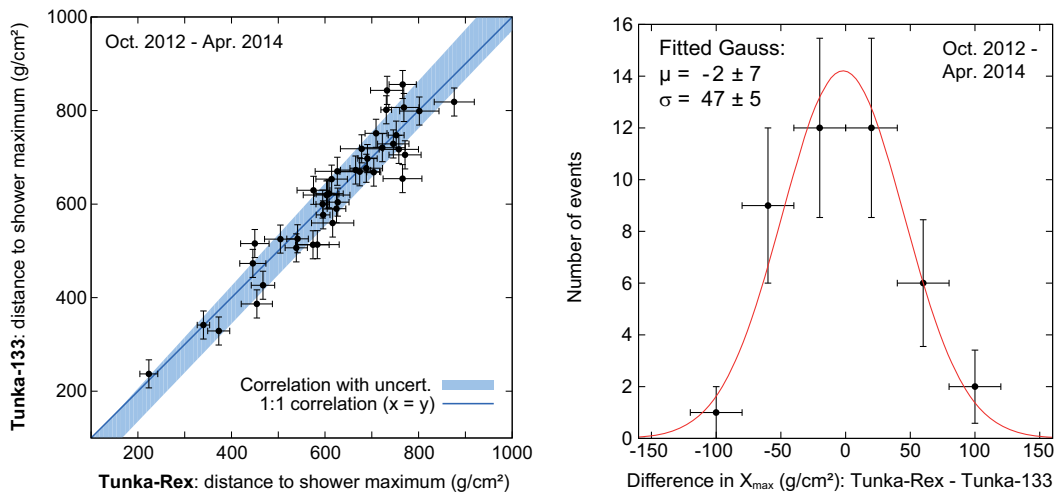


Figure 6.16.: Correlation of the distance to shower maximum as reconstructed with Tunka-Rex radio and Tunka-133 air-Cherenkov measurements for the merged dataset (2012-2014) after applying additional quality cut excluding outer events.

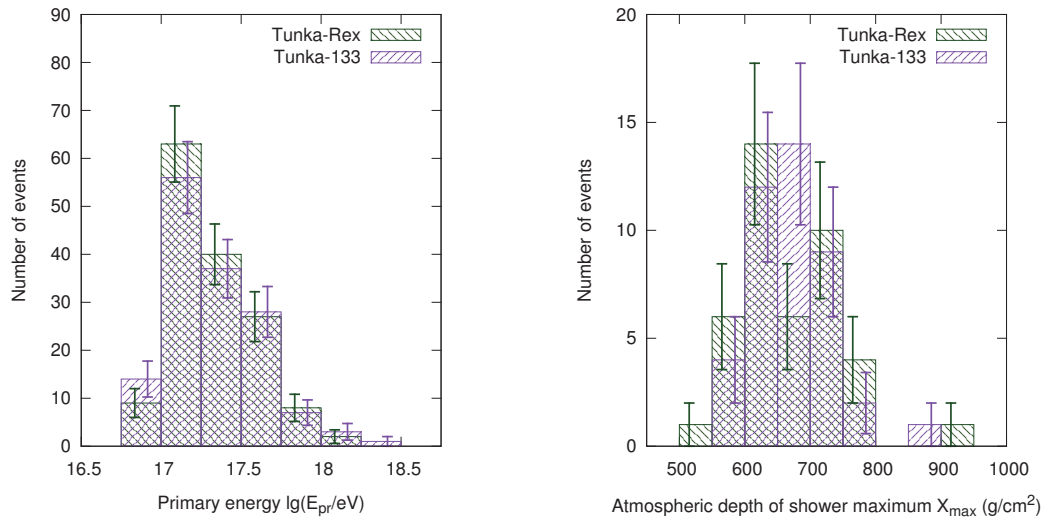


Figure 6.17.: Distributions of the energy and the atmospheric depth of the shower maximum as reconstructed by Tunka-Rex and Tunka-133 for the merged dataset (2012-2014) applying the additional quality cut excluding outer events.

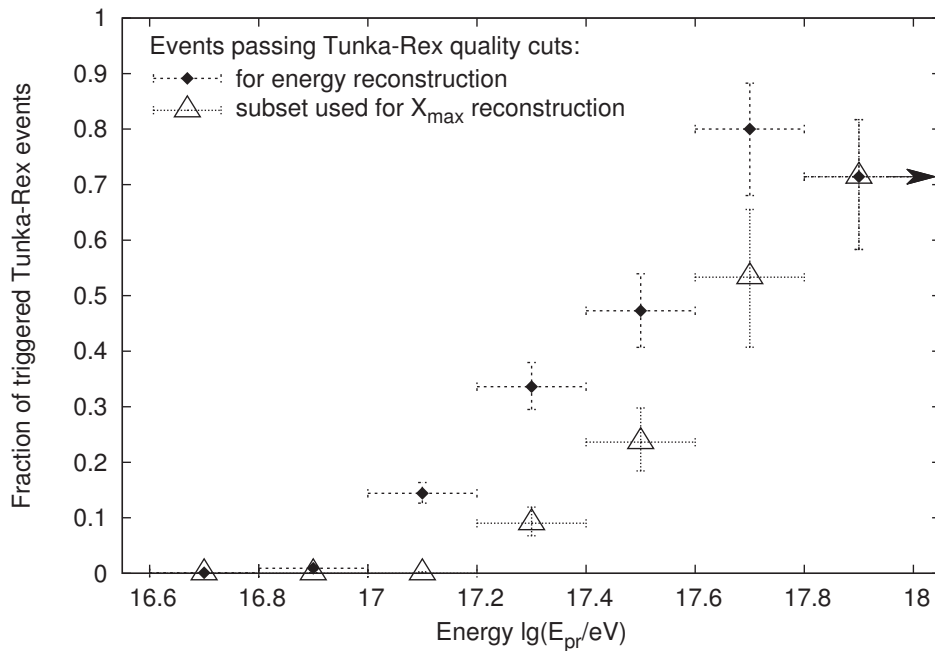


Figure 6.18.: The number of Tunka-Rex events with energy and shower maximum reconstruction to total number of triggered Tunka-133 events. Excluding events with small geomagnetic contribution [133] one can see, that Tunka-Rex can reconstruct the energy starting from $10^{17.5}$ eV, and shower maximum from $10^{17.8}$ eV. Undetected events at highest energies have arrival directions with small geomagnetic angle (i.e. geomagnetically suppressed).

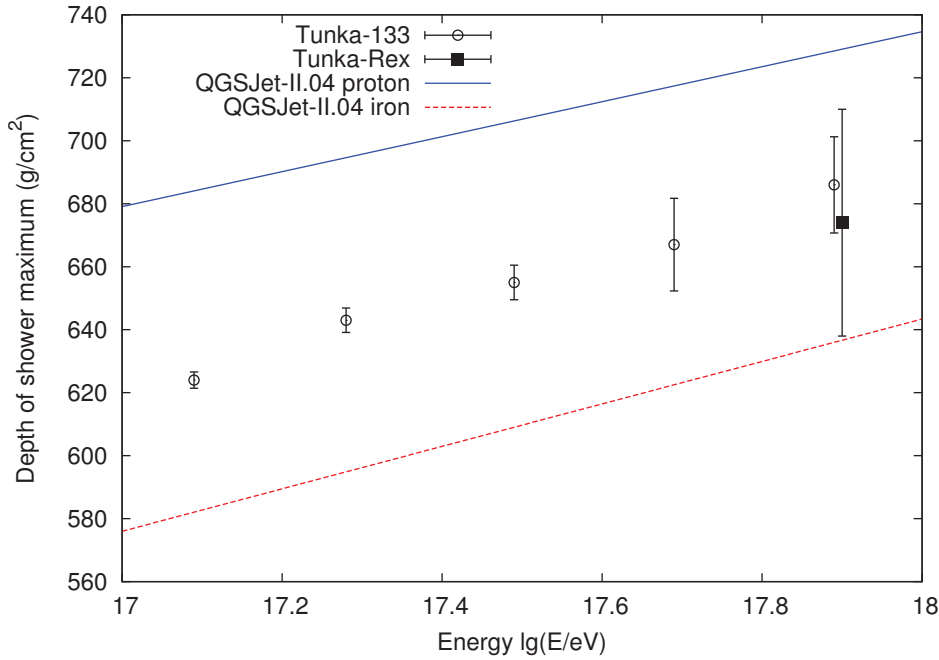


Figure 6.19.: Mean experimental depth of maximum versus the primary energy reconstructed by the Tunka-133 [134] and Tunka-Rex experiments. Uncertainty bars are the statistical uncertainty.

Since the quality cuts for the shower maximum reconstruction reject a significant number of detected events, it is interesting to check how the quality of the reconstruction depends on the primary energy. For this purpose, events were binned by energy, the fractions of triggered Tunka-133/Tunka-Rex events and events passing the quality cuts were calculated. The distribution is presented in Fig. 6.18. Taking into account the low efficiency at small geomagnetic angles [133], one can state, that events starting from $10^{17.8}$ eV have sufficient quality for the shower-maximum reconstruction. By this, one value related to the mass composition can be already estimated by the Tunka-Rex experiment: $\langle X_{\max} \rangle = 674 \pm 36$ g/cm² for $\lg(E_{\text{pr}}/eV) = 17.9 \pm 0.1$ (for 8 events). One can see the comparison of this measurement with the measurements of Tunka-133 in Fig. 6.19. This is another indication that the reconstruction methods for Tunka-Rex are reliable, and shows the potential available when the statistics are significantly increased by the planned day-time trigger.

6.4.4. Further improvements

The methods developed for Tunka-Rex take into account all important properties of the lateral distribution of the radio amplitudes on the surface of the detector. However, some finer features were determined to be negligible or estimated only roughly. Let us briefly discuss a few of them and their influence on the reconstruction:

- Different size of electromagnetic components in proton and iron air-showers: air-showers induced by heavier nuclei have less electrons than those initiated by lighter ones, and the energy estimator has different normalizations for the different particles.

- Geometrical sizes of the air-shower: since the geomagnetically-produced radio emission increases with the distance passed by the electromagnetic component, the total emitted power can change depending on the zenith angle. Moreover, the intensity decreases with increasing zenith angle (since the emission is spread over a large area).
- Azimuthal asymmetry: in the present analysis a constant size of the asymmetry is assumed, but it was already shown, that it can slightly vary with the longitudinal and lateral development of the air-shower.

All of these features have only small influence on the total signal amplitude (less than roughly 10%), and may carry information about mass composition. In addition, more sophisticated treatment of signals (e.g. polarization studies) or more detailed investigation of the lateral distribution (e.g. trying a likelihood fit including stations without signal) can be applied as well. Finally, alternative approaches, for example, the reconstruction of the shower maximum via the shape of the radio wavefront should be investigated [147].

6.5. Conclusion

Operating close to threshold can seriously complicate the measurements. It requires treatment of low-signal antenna stations and prevents the application of very strict quality cuts. Nevertheless, using models and simulations, it is possible to restrict the influence of the background, to increase the purity, and to eliminate additional free parameters in the reconstruction methods. In the case of Tunka-Rex, this has been done while retaining maximum possible statistics: even events containing only three antennas were included for the energy and shower maximum reconstruction. Of course, not all of them can be used for the high-precision measurements, but the proper definition of measurement uncertainties enables rejection of low-quality events, which was successfully implemented for Tunka-Rex.

Finally, after all improvements and quality cuts, the resolution of the Tunka-Rex detector is better than 15% for the energy reconstruction and about 38 g/cm^2 for the reconstruction of the atmospheric depth of the shower maximum (quadratically subtracting the Tunka-133 precision of 28 g/cm^2 from the combined resolution of 47 g/cm^2). These values can probably be slightly improved by applying even stronger quality cuts or through further optimization of the methods.

The results of the Tunka-Rex air-shower reconstruction were compared to Tunka-133 reconstruction event-by-event, and have shown, that there are no discrepancies in the absolute scales. This again proves that radio arrays provide a stable and consistent technique for air-shower detection. The absence of explicit tuning on the existent air-Čerenkov detector shows that radio measurements can contribute to the determination of the absolute scale of the energy spectrum and mass-composition reconstruction.

7. Conclusion

Tunka-Rex, the Tunka Radio Extension was deployed in summer 2012, and started data acquisition in autumn 2012. The experiment was quickly built using existing designs and components. In particular, trigger, DAQ and infrastructure of the existing Tunka-133 setup in Russia were used, and electronics, antenna were designed in Germany based on experience with the Auger Engineering Radio Array. The main problem to solve was the data analysis and interpretation: previously developed methods do not work without adaption for Tunka-Rex, particularly, there was no verified method for the reconstruction of the shower by a radio detector. Thus, Tunka-Rex faced two main challenges: to prove that this hardware configuration is able to detect air-showers, and to develop and test new, optimized methods of air-shower reconstruction using the radio technique.

The main advantage of Tunka-Rex is the precise air-Čerenkov array Tunka-133 at the same site, which provides the trigger and an accurate reconstruction of the shower arrival direction and core position. In addition, Tunka-133 has a high resolution for the reconstruction of air-shower parameters. On the other hand, Tunka-Rex is limited by the duty cycle of the trigger of only about 5%, since the measurements are only possible in moonless winter nights with clear sky. Motivated by promising first measurements, the available dataset (two years of measurements with effective time of about 500 hours) was divided in two parts: the first part was used for the development and test of experimental methods. The second part was used for a blind cross-check of the developed methods. Beside this, a cross-calibration with the air-Čerenkov detector Tunka-133 was planned, i.e. the normalization of coefficients for the reconstruction of the energy and the shower maximum should have been tuned to the values of Tunka-133. However, the values predicted by CoREAS simulation for Tunka-Rex are already in good agreement with the values given by Tunka-133 and have the same scale, i.e. the cross-calibration is not necessary. This indicates that calibration and reconstruction were done properly and it proves, that modern numerical models, particularly, CoREAS and CORSIKA provide a good description for the radio emission generated during the air-shower development. This increases not only the confidence in the radio technique, but also provides an additional verification of the existing Tunka-133 experiment.

The most important property of the performance of the detector is the resolution. For air-shower measurements these are the resolutions of the primary energy E_{pr} and the atmospheric depth of the shower maximum X_{max} . The obtained resolution of 15% for E_{pr} is comparable to modern optical techniques, providing approximately the same resolution. The resolution for X_{max} is about 38 g/cm^2 , a factor of two worse than the resolution of optical methods. It is worth noting that Tunka-Rex is the first and world-unique experiment, which performed a direct comparison of X_{max} reconstruction by radio against the established air-Čerenkov technique for individual events. An open issue for Tunka-Rex is the quality of the events: presently, for X_{max} reconstruction, only high-quality events are selected, most of them at energies of $E_{\text{pr}} > 10^{17.5} \text{ eV}$, several times higher than the threshold. This issue can be solved by improving the data analysis and increasing the density of the array. Generally, there are no known principal limits for further improvements of efficiency and resolution.

In the theoretical part of the present work there are several key points. Different methods for the parameterization of the lateral distribution were revisited, and the most optimal one for Tunka-Rex was selected. For the reconstruction of air-shower parameters, the formulas developed for the air-Čerenkov detector Tunka-133 were successfully optimized for Tunka-Rex. A significant difference between air-Čerenkov and radio emission from air-showers is that the latter is produced by the combination of two different phenomena: by geomagnetic and Askaryan emission. As found in the present work, the asymmetry resulting from this interference can be described by introduction of one parameter, the fraction of the relative strengths of both emission mechanisms, which can be simply estimated or measured. In the approach developed for Tunka-Rex, this parameter is directly put into the lateral distribution function, while in other works the nature of the asymmetry is hidden in more complex functions.

As last point it is worth noticing that a new approach has been tested in the present work: a three-dimensional tomographic simulation of a single air-shower. This simulation has already shown a number of interesting features of the air-shower development, which can be investigated in future.

7.1. Where to go

Let us discuss the plans for the future development of the radio technique at the Tunka facility, and some general prospects of the radio detection of air-showers.

Currently, the Tunka facility is undergoing intensive development. Extensions for lower energies are being built: imaging and non-imaging air-Čerenkov detectors. Additionally, the duty cycle and statistics at higher energies is increased: new scintillators jointly working with radio stations enable to study cosmic rays in the EeV region. In the present work only data of 2012-2014 have been presented and analyzed. This dataset includes measurements obtained with the TREX-18 and TREX-25 configurations, which have been triggered by the air-Čerenkov detector Tunka-133. In 2016, Tunka-Rex will be extended by additional 19 antennas connected to Tunka-Grande. The next obvious step is to analyze data, measured in 2014-2016, with the TREX-44 array, triggered by the scintillator array Tunka-Grande. This allows one to combine radio and muon detection to improve the sensitivity to the mass composition. In addition to this, together with Tunka-133, there will be a unique cross-check between three different methods of air-shower reconstruction: air-Čerenkov, radio, and particle detection.

Currently, the radio technique occupies a niche in cosmic-ray research. It serves as a complementary technique for the detection of air-showers with primary energies starting around 0.1 EeV. Currently, an easy and efficient solution for self-triggering of antenna stations does not exist. The future application of the radio technique needs a simple external particle trigger. For inclined air-showers this trigger also plays an important scientific role: particle detectors measure only the muonic component of inclined air-showers (electrons are absorbed in the atmosphere for inclined showers), this leads, again, to a combined study of the electron-muon ratio in air-showers. If successful, this can be applied for neutrino searches in the atmosphere.

To summarize, one can expect very interesting and fruitful results coming from the radio detection of cosmic rays in the next decade.

A. Antennas connected to HiSCORE stations

One of the side actually goals of the HRJRG was the attachment of the engineering antenna stations to the first HiSCORE detectors. The main difference between hardware installed on Tunka-133 and Tunka-HiSCORE is the sampling rate: 200 MHz and 1 GHz for Tunka-133 and Tunka-HiSCORE, respectively. Due to technical issues with Tunka-Grande data-acquisition hardware, antennas were installed and tested only in autumn 2014.

One of the important goals of the first measurements was the testing of the HiSCORE timing, the design precision of which was declared to beat sub-nanosecond level. The idea was to use the Tunka-Rex beacon for the time calibration. Unfortunately, the time calibration could not be done due to very short signal traces of HiSCORE detectors, with the length of 1024 samples, which corresponds to length of about 1 ms. The beacon frequencies are not sufficiently distinguishable in the spectrum (see Fig. A.1), i.e. one cannot obtain the proper phase of the beacon signals and perform the time calibration using phase shifts.

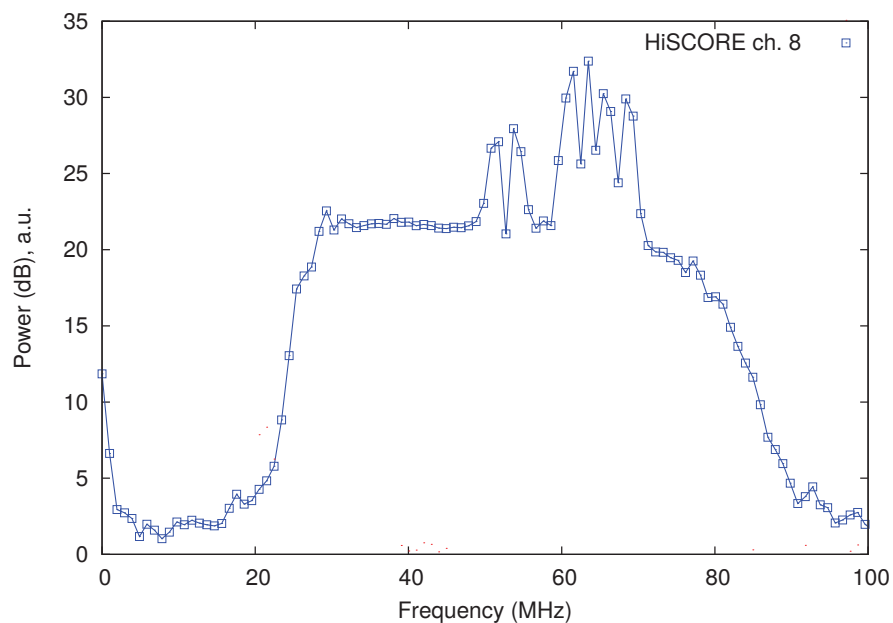


Figure A.1.: Background spectrum measured on the antenna attached to HiSCORE detector. Due to the high sampling frequency (1 GHz) and the short trace (1024 samples) the resolution is too low to distinguish the beacon peaks at 63.5 and 68.1 MHz.

B. Software configuration for Tunka-Rex

This Appendix gives an overview of the software configuration used for the Tunka-Rex analysis, and a brief description of libraries and utilities, which have been developed specially for Tunka-Rex analysis in the frame of this thesis. The following programs have been used:

- **Offline** For the main part of the Tunka-Rex analysis, a software developed by the Pierre Auger Collaboration [135], was kindly shared with the Tunka-Rex Collaboration. Tunka-Rex uses a modified version of `Offline` (branch version 1.0.6 in the Tunka-Rex repository). Several of the modules were developed by me in the frame of this work. The applications developed for Tunka-Rex are placed in `StandardApplications/TRex`; particularly, two main applications used for the reconstruction of simulations and real data: `reco/standard` and `reco/standard_sim`. The module sequence is given in Listing B.1. The modules developed for Tunka-Rex analysis are:
 - **RdGetCherenkovReconstruction** This module extracts and saves the air-shower reconstruction of the air-Čerenkov detector Tunka-133 from a file provided by the Tunka-133 Collaboration. If this module is called after the radio reconstruction, then it compares the direction reconstruction between the radio and air-Čerenkov detectors. In addition, it can apply quality cuts on zenith and direction reconstruction.
 - **RdLDFChargeExcessCorrector** This module corrects the lateral distribution according to the model of the interference between geomagnetic and Askaryan contributions (c.f. Chapter 5). It corrects the amplitude at each antenna station corresponding to its azimuthal coordinate. This module features a parameterization depending on distance to the shower axis. When the asymmetry is set to zero, it corrects only for the geomagnetic angle.
 - **RdCheckFootprint** This module rejects outliers from the lateral distribution. Currently it is configured in order to reject obvious outliers by looping through antenna stations by their distance to the shower axis: if two antenna stations on the lateral distribution do not pass the SNR cut, all further antennas are rejected.
 - **RdLDFMultiFitter** This module fits the lateral distribution with a one-dimensional function. It supports multiple functions (performs several fits per iteration). Currently this module is used for simple exponential and Gaussian functions. One can fix the width of the Gaussian as function of zenith angle and estimated primary energy.
 - **RdAirShowerReconstruction** This module reconstructs air-shower parameters using the models described in the present work (c.f. Chapter 5). It requires the corresponding LDF, fitted by the `RdLDFMultiFitter` module.

- **CORSIKA/CONEX/CoREAS** These software packages simulates air-showers and the radio emission induced by electrons and positrons during air-shower development. All simulations in the present work have been performed using this software set; their description is given in Section 5.2. The typical configuration is given in Table B.1.
- **SiMM** This software controls running the simulations, their configuration and performance. It provides the interfaces between CoREAS and Offline. This software was implemented by me and is used for managing Tunka-Rex and TAIGA-IACT simulations. The principal scheme is depicted in Fig. B.1, the full documentation will be published in Ref. [143].
- **TRexRecoTools** This small package performs the final part of the analysis of Tunka-Rex data. Since Offline works on the event level, TRexRecoTools performs statistical analyses of all reconstructed events, applies high-quality cuts, compares the reconstructions of Tunka-Rex and Tunka-133, and provides visualization of analyzed events. Also this package was developed in the frame of this work and currently is used only internally in the Tunka-Rex Collaboration.

Listing B.1: Offline module sequence used in the standard Tunka-Rex reconstruction

```
<module> EventFileReaderOG </module>
<module> RdEventPreSelector </module>
<module> RdEventInitializer </module>
<module> RdChannelADCToVoltageConverter </module>
<module> RdChannelBeaconSuppressor </module>
<module> RdChannelResponseIncorporator </module>
<module> RdChannelUpsampler </module>
<module> RdChannelBandstopFilter </module>
<module> RdGetCherenkovReconstruction </module>
<module> RdAntennaChannelToStationConverter </module>
<module> RdStationSignalReconstructor </module>
<module> RdLDFChargeExcessCorrector </module>
<module> RdCheckFootprint </module>
<loop numTimes="unbounded">
  <module> RdDirectionConvergenceChecker </module>
  <module> RdPlaneFit </module>
</loop>
<module> RdGetCherenkovReconstruction </module>
<module> RdLDFMultiFitter </module>
<module> RdAirShowerReconstruction </module>
<module> RdEventPostSelector </module>
<module> RecDataWriterNG </module>
```

Table B.1.: Example CORSIKA steering card for proton event with energy of 0.1 EeV. The corresponding CONEX configuration differs only by two parameters: CORSIKA = "F" and LONGI = "T 10 T T".

RUNNR	17915				
EVTNR	1				
SEED	869045969	0	0		
SEED	501312295	0	0		
SEED	535334553	0	0		
NSHOW	1				
ERANGE	1e+08	1e+08			
PRMPAR	14				
THETAP	47.3024	47.3024			
PHIP	192.236	192.236			
ECUTS	3.000E-01	3.000E-01	4.010E-04	4.010E-04	
ELMFLG	T	T			
THIN	1.000E-06	100	0.000E+00		
THINH	1.000E+01	1.000E+02			
OBSLEV	67501.1				
ECTMAP	1.E5				
STEPFC	1.0				
MUADDI	T				
MUMULT	T				
MAXPRT	1				
MAGNET	18.8823	57.2864			
ATMOD	0	F			
PAROUT	F	F			
LONGI	T	5.	T	T	
RADNKG	5.e5				

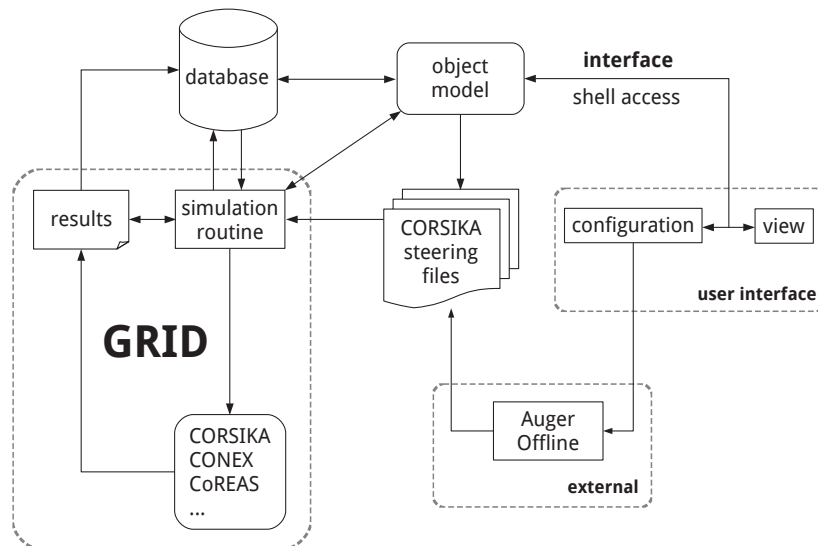


Figure B.1.: Principal scheme of the SiMM software. It provides an interface between CONEX, CORSIKA, CoREAS and Offline using a MySQL database. The software is useful for managing thousands of parallel simulations (particularly, on cluster/Grid), e.g., for precisely fitting air-showers properties, like X_{\max} , etc. The detailed documentation will be published in Ref. [143].

C. Remarks on the complexity of the methods

Is it really necessary to apply the developed sophisticated methods, such as the Gaussian LDF and the asymmetry correction, or would simple methods be sufficient? Only the amplitude adjustment for noise correction is not discussed, because the influence of noise is significant, and it is already proven, that correcting signals improves the reconstruction [155]. To get an impression of how various complications change the reconstruction quality, they were selective toggled one by one, and the reconstruction was done with a simplified process. The methods of air-shower reconstruction were kept the way they are, only the lateral distribution function was varied.

In this way, the reconstruction for the events of 2012-2014 was performed with the following simplifications:

- Approximation of zero asymmetry ($\varepsilon = 0$): In this approximation, the correction operator \hat{K} defined in Eq. (5.21) converts to the simple form given in Eq. (5.22). This form contains only the normalization to the geomagnetic angle α_g . At Tunka, the value of the charge excess contribution is on the order of 10%, which is less than the amplitude uncertainty. This means, that there might be no clear improvement for the reconstruction of the air-shower parameters.
- Approximation of the LDF by a simple exponential function with charge excess consideration: in this approximation the simplest reasonable LDF was chosen, i.e. $\mathcal{E}_1 = \mathcal{E}_2(a_2 = 0)$. As it was shown in the previous Chapter, this function describes the lateral distribution much worse than the Gaussian LDF. Nevertheless, it is interesting to investigate how this changes the resolution of the air-shower reconstruction. Moreover, with small number of antennas stations per events, this parameterization still might provide sufficient resolution.
- The simplest parameterization, an exponential LDF without asymmetry correction, i.e. $\varepsilon = 0$ and $a_2 = 0$.

The results of the reconstruction are given in Table C.1. One can see, that the precision of the energy reconstruction is the same for all datasets. This is simply explained by the fact that the simplest method already provides a resolution comparable to Tunka-133 [134]. The combined resolution of the shower-maximum reconstruction significantly differs for the different LDFs: $47 \pm 5 \text{ g/cm}^2$ for \mathcal{E}_2 (i.e. standard reconstruction) versus $61 \pm 6 \text{ g/cm}^2$ for \mathcal{E}_1 . Subtracting the resolution of 28 g/cm^2 of Tunka-133, one obtains corresponding values for stand-alone Tunka-Rex precision: 38 g/cm^2 and 54 g/cm^2 , respectively. Since the latter precision is significantly worse than the one reached with the standard reconstruction procedure, it is interesting to discuss the obtained result. One can see the comparison between shower maxima reconstructed by Tunka-Rex and Tunka-133 in Fig. C.1.

The obtained results indicate, that even the simple LDF parameterization gives a significant correlation of the slope of the radio LDF and the distance to shower maximum. It is surprising, that the resolution of Tunka-Rex, when using this parameterization is about 54 g/cm^2 , which is the same as the theoretical prediction for LOPES, with a more complicated Gaussian LDF [82]. This can be explained by the different treatment of shower

Table C.1.: Comparison of the resolutions of air-shower reconstructions given by standard and simplified methods.

O: Standard reconstruction described in Chapter 6.

I: Reconstruction without charge excess asymmetry correction ($\varepsilon = 0$).

II: Reconstruction with simple exponential LDF \mathcal{E}_1 instead of Gaussian \mathcal{E}_2 .

III: Reconstruction with simple exponential LDF \mathcal{E}_1 instead of Gaussian, and without asymmetry correction ($\varepsilon = 0$).

#	Reconstruction	$\Delta E_{\text{pr}}/E_{\text{pr}}$ (%)	ΔX_{max} (g/cm ²)	Tunka-Rex precision (g/cm ²)
O	Standard	19 ± 2	47 ± 5	≈ 38
I	$\varepsilon = 0$	16 ± 1	54 ± 6	≈ 46
II	$a_2 = 0$	17 ± 1	66 ± 7	≈ 60
III	$\varepsilon = 0$ and $a_2 = 0$	18 ± 1	61 ± 6	≈ 54

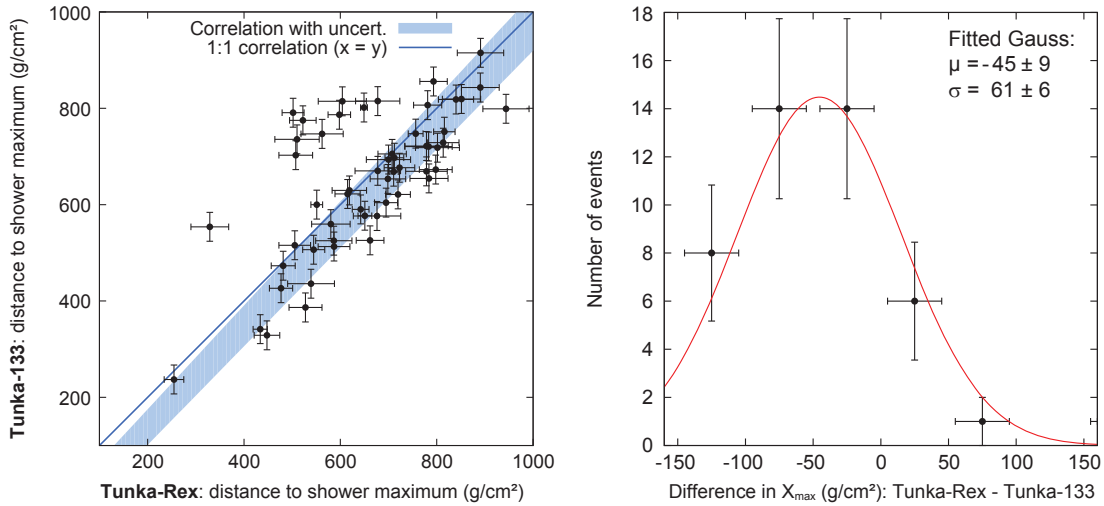


Figure C.1.: Correlation of the distance to the shower maximum between Tunka-133 and Tunka-Rex arrays, when Tunka-Rex uses the simplest LDF parameterization, i.e. the exponential LDF instead of the Gaussian LDF.

maximum: the methods in the present work were developed in terms of distance to shower maximum (which squeezed the value domain in factor of $1/\cos\theta$). In Ref. [82] there was an attempt to find a correlation to shower maximum using fixed zenith bins. The resolution even in simulations was not as high or stable as the method used here, so probably, this approach simply does not work well. The same approach was also used for the Yakutsk radio array [93, 94], but only average values have been presented as results. No studies of uncertainties or cross-checks for individual events have been published.

D. Magnetic field of the Earth

To perform accurate calculations of the geomagnetic effect, it is important to know the configuration of the magnetic field. Any magnetic field is defined by two properties: strength and direction. In the case of radio detection of air-showers, the first parameter defines the maximum emission power coming from the geomagnetic effect, and the second parameter defines the fraction of this power for a given air-shower direction.

The magnetic field of the Earth can be either directly measured or calculated with one of the two popular models: the International Geomagnetic Reference Field (IGRF) [158] or the World Magnetic Model (WMM) [159]. To know the vector of the geomagnetic field at the time t at geocentric coordinates r , θ , and ϕ one uses the relation $\mathbf{B}(r, \theta, \phi, t) = \nabla V(r, \theta, \phi, t)$ with the scalar potential

$$V(r, \theta, \phi, t) = a \sum_{n=1}^N \sum_{m=0}^n \left(\frac{a}{r}\right)^{n+1} [g_n^m(t) \cos(m\phi) + h_n^m(t) \sin(m\phi)] P_n^m(\cos \theta), \quad (\text{D.1})$$

where r is the radial distance from the center of the Earth, $a = 6371.2$ km is the reference radius of the Earth, which is close to the mean value, and θ and ϕ denote latitude and longitude, respectively. $P_m^n(\cos \theta)$ are the normalized associated Legendre functions of degree n and order m . The time-dependent Gauss coefficients $g_n^m(t)$ and $h_n^m(t)$ are interpolated from tabulated values $g_n^m(T_0)$ and $h_n^m(T_0)$ measured every 5 years.

The corresponding software usually gives the components X_B , Y_B and Z_B of the geomagnetic field, i.e. $\mathbf{B} = (X_B, Y_B, Z_B)$. The horizontal H_B and vertical V_B components used in the CORSIKA software are connected to them by the relations

$$H_B = \sqrt{X_B^2 + Y_B^2}, \quad V_B = Z_B. \quad (\text{D.2})$$

The inclination θ_I and declination ϕ_D are defined as

$$\theta_I = \arctan(V_B/H_B), \quad \phi_D = \arctan(Y_B/X_B). \quad (\text{D.3})$$

The shower axis and geomagnetic field are defined as follows in detector coordinate system with origin in the shower core

$$\begin{cases} x_A = \sin \theta_A \cos \phi_A \\ y_A = \sin \theta_A \sin \phi_A \\ z_A = \cos \theta_A \end{cases}, \quad \begin{cases} x_B = \sin(\pi + \pi/2 + \theta_I) \cos(\pi/2 - \phi_D) \\ y_B = \sin(\pi + \pi/2 + \theta_I) \sin(\pi/2 - \phi_D) \\ z_B = \cos(\pi + \pi/2 + \theta_I) \end{cases}, \quad (\text{D.4})$$

here θ_A and ϕ_A are the zenith and azimuth of the arrival direction of the air-shower. Inclination and declination of the geomagnetic field are denoted as θ_I and ϕ_D , respectively. These transformations give the normalized vectors $\hat{\mathbf{V}} = (x_A, y_A, z_A)$ and $\hat{\mathbf{B}} = (x_B, y_B, z_B)$ used in the present work.

One the next page the location of historical and modern radio experiments measuring air-showers are shown on a map of the strength of the geomagnetic field (Fig. D.1).

D. Magnetic field of the Earth

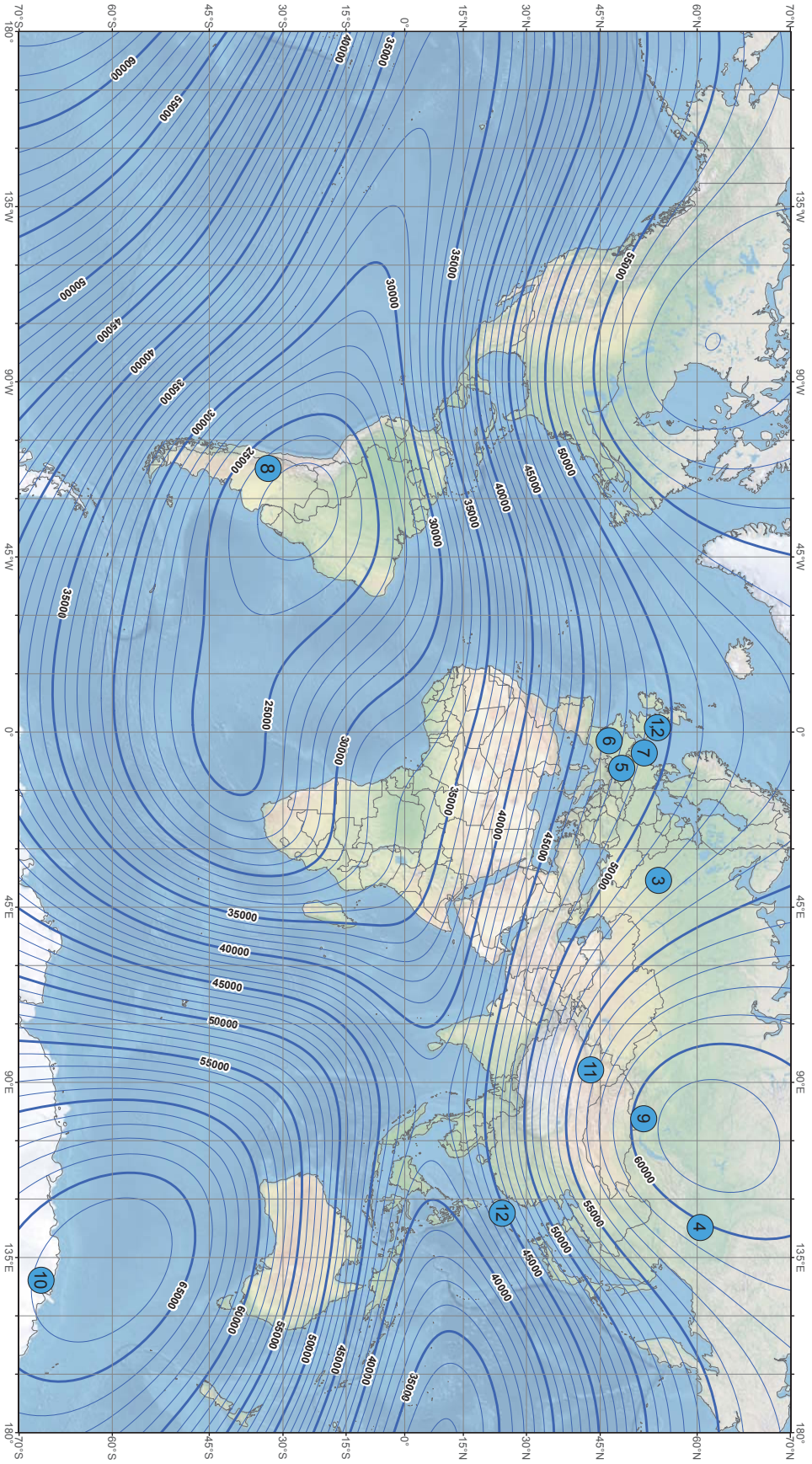


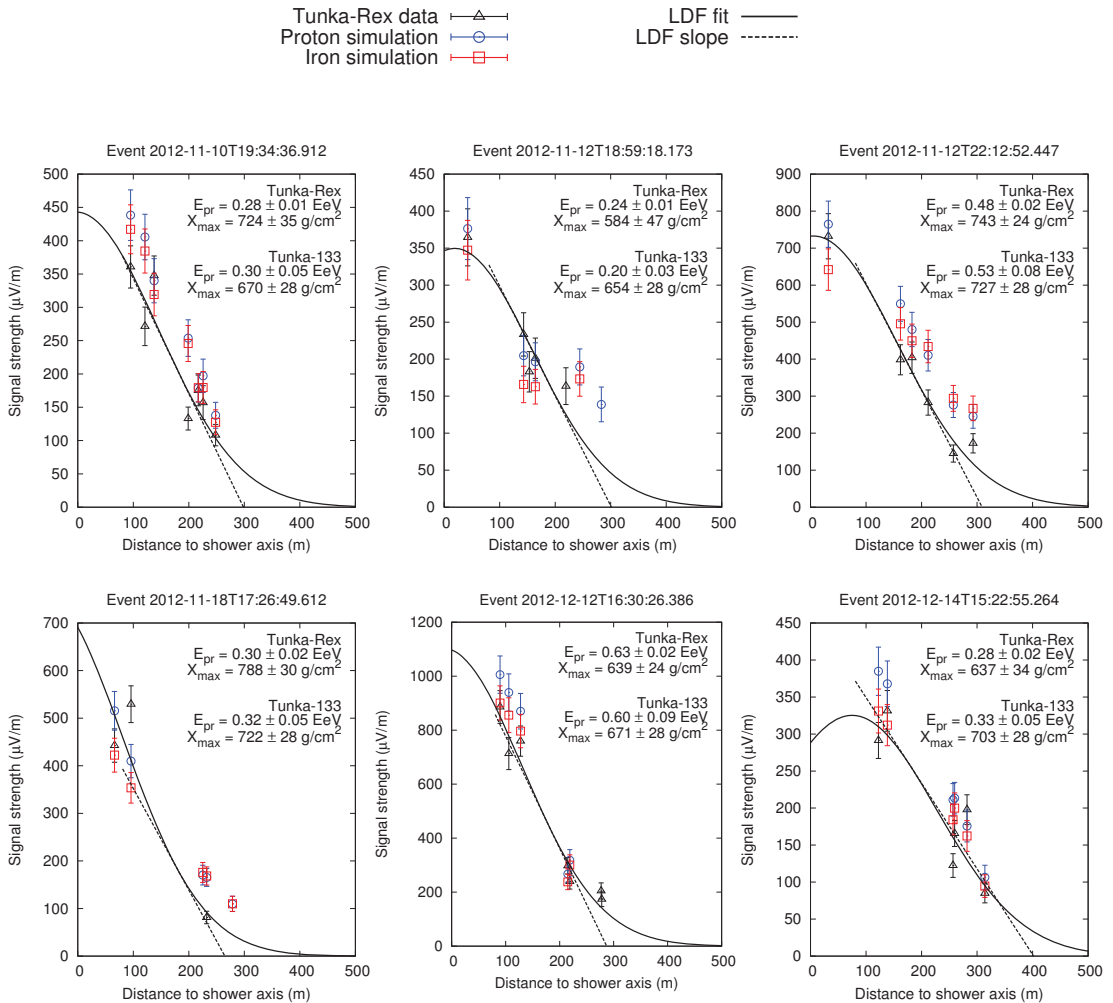
Figure D.1.: Strength of the Earth's magnetic field predicted by WMM2015 [159] with radio setups measuring geomagnetic emission.
 1 – Jodrell Bank (England, first discovery of the radio emission from air-showers) [48]; 2 – Haverah Park (England) [51]; 3 – MSU (Russia) [75];
 4 – Yakutsk (Russia) [94]; 5 – LOPES (Germany) [82]; 6 – CODALEMA (France) [83]; 7 – LOFAR (Netherlands) [86]; 8 – AERA (Argentina) [91];
 9 – Tunka-Rex (Russia) [72]; 10 – ANITA (Antarctica) [100]; 11 – TREND (China) [97]; 12 – TAROGE (Taiwan) [108];

E. Example events

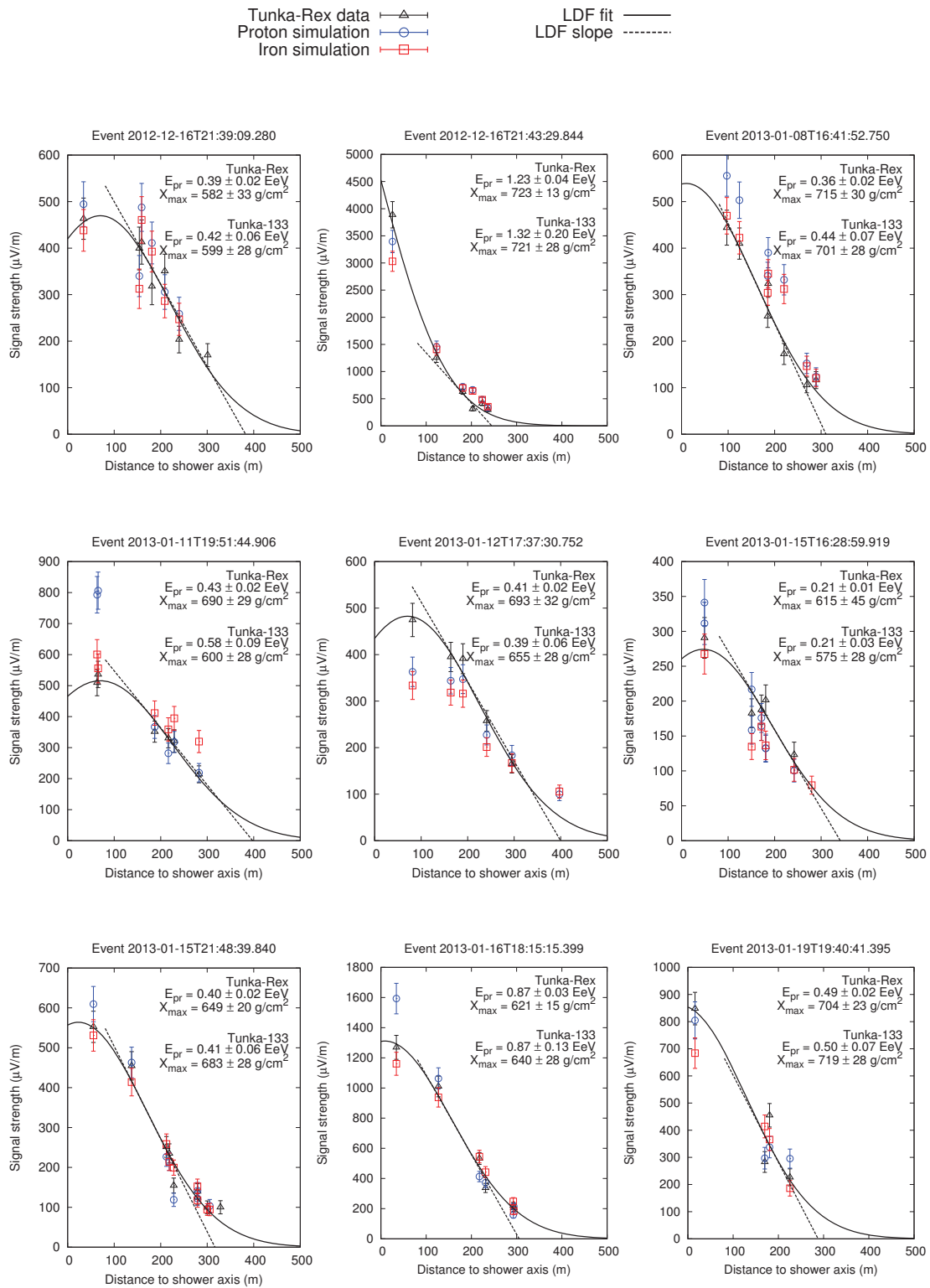
This Appendix gives a visualization of example events measured by Tunka-Rex and simulated with CoREAS software in the frame of the present work.

Tunka-Rex reconstruction compared with simulations

This Section presents a subset (first 15 events ordered by time) of high-quality Tunka-Rex events (selected for X_{\max} reconstruction) measured during the Tuning season. As it was explained in Section 5.2, air-showers detected by Tunka-133 in the Tuning season were simulated with CoREAS. Each plot presents the Tunka-Rex amplitudes with respect to the distance to shower axis, the LDF fitted with these points and its slope. The Tunka-Rex points are given in comparison with simulated amplitudes for proton and iron showers with shower parameters similar to the Tunka-133 reconstruction. Some amplitudes are missing for Tunka-Rex due to failures of antenna stations.



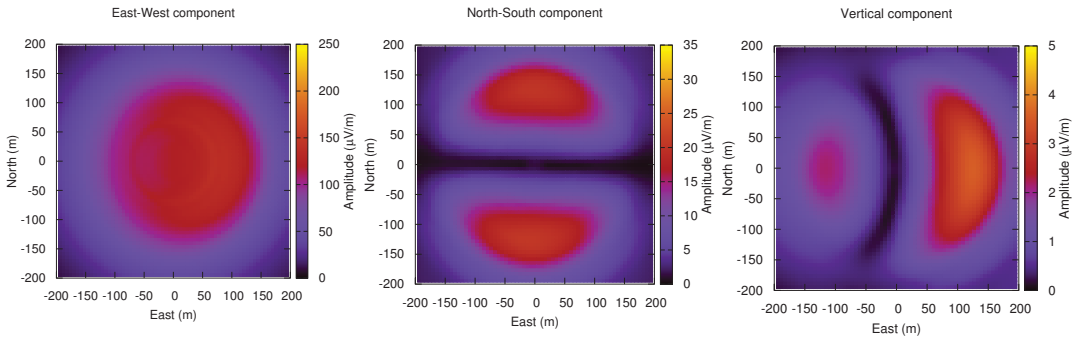
E. Example events



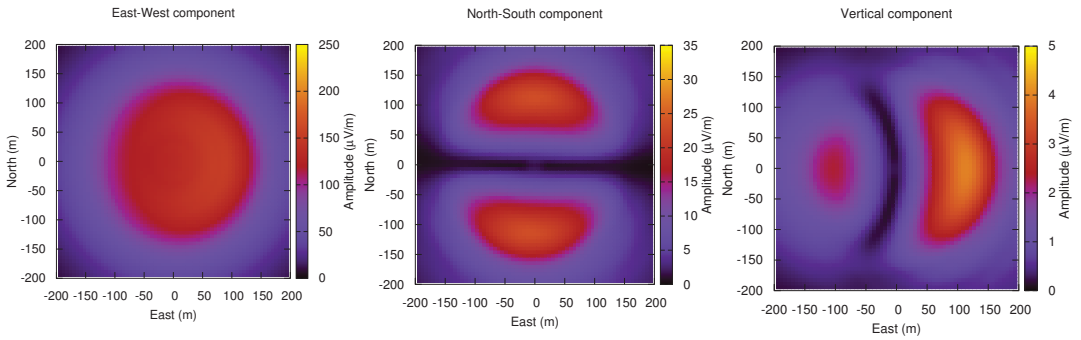
Profiles of radiotomographic simulation

This Section shows the distribution of amplitudes of the simulation dataset T-SET. All plots are from the same simulated vertical proton air-shower with $E_{pr} = 0.1$ EeV and $X_{max} = 630$ g/cm² at different observation depths (for details see Section 5.2). Amplitudes are directly taken from the CoREAS simulation and filtered with a 30-80 MHz rectangular filter. Each amplitude is presented component-wise: East-West, North-South, and vertical. For a vertical air-shower they are the $\hat{\mathbf{V}} \times \hat{\mathbf{B}}$, $\hat{\mathbf{V}} \times (\hat{\mathbf{V}} \times \hat{\mathbf{B}})$ and $\hat{\mathbf{V}}$ components in geomagnetic coordinates. Here the properties of the distributions are not discussed, the corresponding discussion can be found, for example, in Ref. [54]. Only a subset of the plots is shown, the full package can be downloaded from <http://3d.tunkarex.info>.

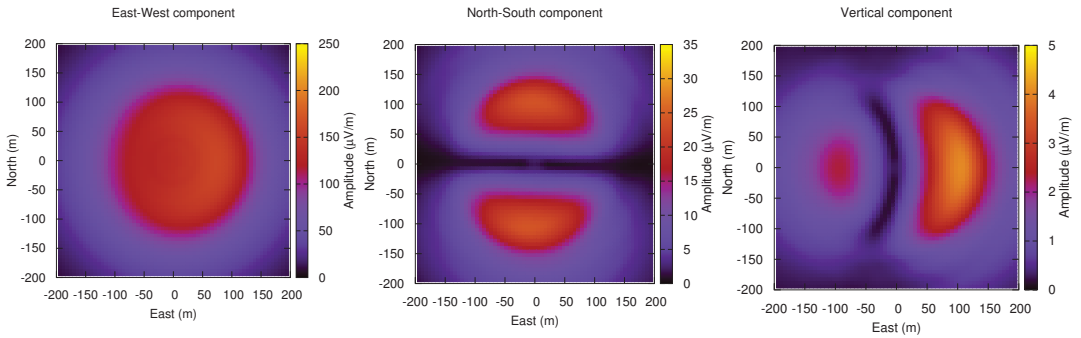
Observation depth 800 g/cm² (distance to $X_{max} = 170$ g/cm²)



Observation depth 830 g/cm² (distance to $X_{max} = 200$ g/cm²)

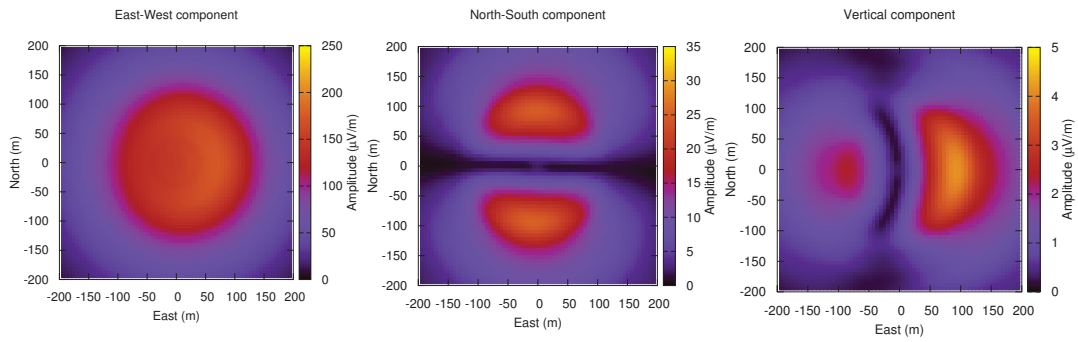


Observation depth 860 g/cm² (distance to $X_{max} = 230$ g/cm²)

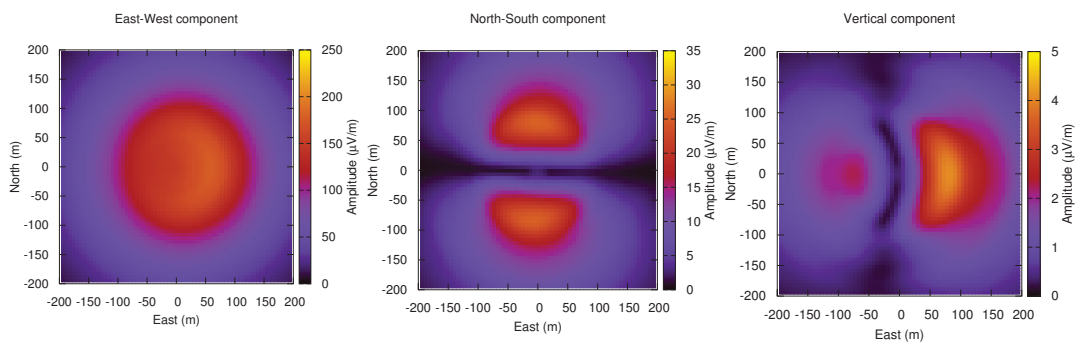


E. Example events

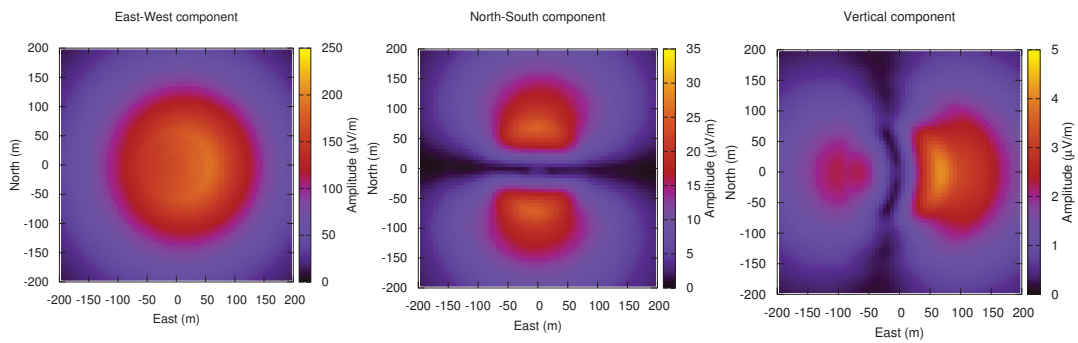
Observation depth 890 g/cm^2 (distance to $X_{\text{max}} = 260 \text{ g/cm}^2$)



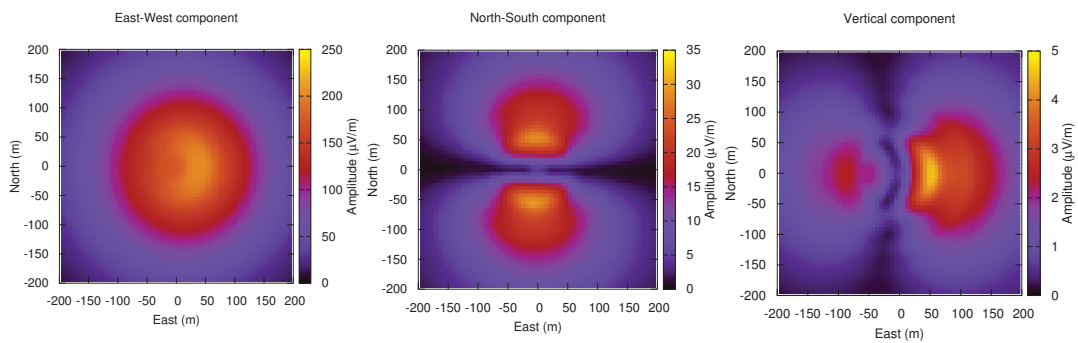
Observation depth 920 g/cm^2 (distance to $X_{\text{max}} = 290 \text{ g/cm}^2$)



Observation depth 950 g/cm^2 (distance to $X_{\text{max}} = 320 \text{ g/cm}^2$)



Observation depth 980 g/cm^2 (distance to $X_{\text{max}} = 350 \text{ g/cm}^2$)



Bibliography

- [1] V. F. Hess. Über Beobachtungen der durchdringenden Strahlung bei sieben Freiballonfahrt. *Physikalische Zeitschrift*, 13:1084, 1912.
- [2] K. Greisen. End to the Cosmic-Ray Spectrum? *Physical Review Letters*, 16:748–750, 1966.
- [3] G. T. Zatsepin and V. A. Kuzmin. Upper limit of the spectrum of cosmic rays. *ZhETF Pisma Redaktsiiu*, 4(3):114–117, 1966.
- [4] Donald V. Reames. The two sources of solar energetic particles. *Space Science Reviews*, 175(1-4):53–92, 2013.
- [5] L. J. Gleeson and W. I. Axford. Solar modulation of galactic cosmic rays. *Astrophysical Journal*, 154:1011, December 1968.
- [6] E. Fermi. On the Origin of Cosmic Radiation. *Physical Review*, 75(8):1169, 1949.
- [7] W. Axford et al. In *Proceedings of the 15th ICRC, Plovdiv, Bulgaria*, volume 11, page 132, 1977.
- [8] F. Aharonian, et al. (H.E.S.S. Collaboration). Primary particle acceleration above 100 TeV in the shell-type supernova remnant RX J1713.7-3946 with deep HESS observations. *Astronomy & Astrophysics*, 464(1):235–243, 2007.
- [9] M. Ackermann et al. Detection of the characteristic pion-decay signature in supernova remnants. *Science*, 339(6121):807–811, 2013.
- [10] B. F. Rauch et al. (TIGER Collaboration). Cosmic Ray origin in OB Associations and Preferential Acceleration of Refractory Elements: Evidence from Abundances of Elements $_{26}\text{Fe}$ through $_{34}\text{Se}$. *Astrophysical Journal*, 697:2083–2088, 2009.
- [11] K.A. Olive et al. Review of Particle Physics. *Chin.Phys.*, C38:090001, 2014.
- [12] W. D. Apel, et al. (KASCADE-Grande Collaboration). The spectrum of high-energy cosmic rays measured with KASCADE-Grande. *Astroparticle Physics*, 36(1):183–194, 2012.
- [13] W. D. Apel, et al. (KASCADE-Grande Collaboration). Kneelike Structure in the Spectrum of the Heavy Component of Cosmic Rays observed with KASCADE-Grande. *Phys. Rev. Lett.*, 107:171104, Oct 2011.
- [14] M. G. Aartsen, et al. (IceCube Collaboration). Measurement of the cosmic ray energy spectrum with IceTop-73. *Phys. Rev. D*, 88:042004, Aug 2013.
- [15] L. Sveshnikova, L. Kuzmichev, E. Korosteleva, V. Prosin, and V.S. Ptuskin. Interpretation of cosmic ray spectrum above the knee measured by the Tunka-133 array. *Nuclear Physics B - Proceedings Supplements*, 256–257(0):218 – 224, 2014. Cosmic Ray Origin – Beyond the Standard Models.

- [16] Denis Allard. Extragalactic propagation of ultrahigh energy cosmic-rays. *Astroparticle Physics*, 39–40:33 – 43, 2012. Cosmic Rays Topical Issue.
- [17] Kseniya V. Ptitsyna and Sergei V. Troitsky. Physical conditions in potential sources of ultra-high-energy cosmic rays. I. Updated Hillas plot and radiation-loss constraints. *Phys. Usp.*, 53:691–701, 2010.
- [18] A. M. Hillas. The origin of ultra-high-energy cosmic rays. *Annual Review of Astronomy and Astrophysics*, 22(1):425–444, 1984.
- [19] T. Antoni, et. al (KASCADE Collaboration). KASCADE measurements of energy spectra for elemental groups of cosmic rays: Results and open problems. *Astropart.Phys.*, 24:1–25, 2005.
- [20] W. D. Apel, et al. (KASCADE-Grande Collaboration). Ankle-like feature in the energy spectrum of light elements of cosmic rays observed with KASCADE-Grande. *Phys. Rev. D*, 87:081101, Apr 2013.
- [21] R. Aloisio, V. Berezhinsky, and A. Gazizov. Transition from galactic to extragalactic cosmic rays. *Astroparticle Physics*, 39–40(0):129 – 143, 2012. Cosmic Rays Topical Issue.
- [22] Veniamin Berezhinsky, A. Z. Gazizov, and S. I. Grigorieva. Dip in UHECR spectrum as signature of proton interaction with CMB. *Phys. Lett.*, B612:147–153, 2005.
- [23] V. Berezhinsky, A. Z. Gazizov, and S. I. Grigorieva. On astrophysical solution to ultrahigh-energy cosmic rays. *Phys. Rev.*, D74:043005, 2006.
- [24] R. Aloisio, V. Berezhinsky, Pasquale Blasi, A. Gazizov, S. Grigorieva, and B. Hnatyk. A dip in the UHECR spectrum and the transition from galactic to extragalactic cosmic rays. *Astropart. Phys.*, 27:76–91, 2007.
- [25] *The Pierre Auger Observatory: Contributions to the 34th International Cosmic Ray Conference (ICRC 2015)*, 2015. arXiv:1509.03732.
- [26] T. K. Gaisser and A. M. Hillas. Reliability of the method of constant intensity cuts for reconstructing the average development of vertical showers. *International Cosmic Ray Conference*, 8:353–357, 1977.
- [27] K. Kamata and J. Nishimura. The Lateral and the Angular Structure Functions of Electron Showers. *Progress of Theoretical Physics Supplement*, 6:93–155, 1958.
- [28] K Greisen. Cosmic ray showers. *Annual Review of Nuclear Science*, 10(1):63–108, 1960.
- [29] O. Scholten, K. Werner, and F. Rusydi. A Macroscopic Description of Coherent Geomagnetic Radiation from Cosmic Ray Air Showers. *Astropart.Phys.*, 29:94–103, 2008.
- [30] O. Adriani et al. The PAMELA Mission: Heralding a new era in precision cosmic ray physics. *Physics Reports*, 544(4):323 – 370, 2014.

-
- [31] M. Aguilar, et al. (AMS Collaboration). First Result from the Alpha Magnetic Spectrometer on the International Space Station: Precision Measurement of the Positron Fraction in Primary Cosmic Rays of 0.5–350 GeV. *Phys. Rev. Lett.*, 110:141102, Apr 2013.
- [32] W. D. Apel et al. (KASCADE-Grande Collaboration). The KASCADE-Grande energy spectrum of cosmic rays and the role of hadronic interaction models. *Advances in Space Research*, 53(10):1456 – 1469, 2014. Cosmic Ray Origins: Viktor Hess Centennial Anniversary.
- [33] I. Allekotte et al. The Surface Detector System of the Pierre Auger Observatory. *Nucl.Instrum.Meth.*, A586:409–420, 2008.
- [34] M. C. Chantell et al. Limits on the isotropic diffuse flux of ultrahigh-energy gamma radiation. *Phys. Rev. Lett.*, 79:1805–1808, 1997.
- [35] Robert J. and Lauer et al. (HAWC Collaboration). Gamma-ray astronomy with the HAWC observatory. *International Journal of Modern Physics: Conference Series*, 28:1460185, 2014.
- [36] A. Aab et al. (Pierre Auger Collaboration). The Pierre Auger Observatory: Contributions to the 33rd International Cosmic Ray Conference (ICRC 2013). In *Proceedings, 33rd International Cosmic Ray Conference (ICRC2013)*, 2013. arXiv:1307.5059.
- [37] J. Abraham et al. The fluorescence detector of the pierre auger observatory. *Nuclear Instruments and Methods in Physics Research Section A: Accelerators, Spectrometers, Detectors and Associated Equipment*, 620(2–3):227 – 251, 2010.
- [38] H. Tokuno et al. New air fluorescence detectors employed in the Telescope Array experiment. *Nuclear Instruments and Methods in Physics Research A*, 676:54–65, June 2012.
- [39] J. Aleksic et al. Performance of the MAGIC stereo system obtained with Crab Nebula data. *Astroparticle Physics*, 35(7):435 – 448, 2012.
- [40] H.E.S.S. Collaboration. H.E.S.S. observations of the Crab during its March 2013 GeV gamma-ray flare. *Astronomy&Astrophysics*, 562:L4, 2014.
- [41] A.A. Ivanov et al. Wide field-of-view Cherenkov telescope for the detection of cosmic rays in coincidence with the Yakutsk extensive air shower array. *Nuclear Instruments and Methods in Physics Research Section A: Accelerators, Spectrometers, Detectors and Associated Equipment*, 772(0):34 – 42, 2015.
- [42] J.W. Fowler, L.F. Fortson, C.C.H. Jui, D.B. Kieda, R.A. Ong, C.L. Pryke, and P. Sommers. A measurement of the cosmic ray spectrum and composition at the knee. *Astroparticle Physics*, 15(1):49 – 64, 2001.
- [43] V.V. Prosin et al. (Tunka-133 Collaboration). Tunka-133: Results of 3 year operation. *Nucl.Instrum.Meth.*, A756:94–101, 2014.
- [44] O. Gress et al. (HiSCORE Collaboration). Tunka-HiSCORE – A new array for multi-TeV astronomy and cosmic-ray physics. *Nuclear Instruments and Methods in Physics*

- Research Section A: Accelerators, Spectrometers, Detectors and Associated Equipment*, 732(0):290 – 294, 2013. Vienna Conference on Instrumentation 2013.
- [45] B.A. Khrenov et al. Pioneering space based detector for study of cosmic rays beyond GZK Limit. *EPJ Web of Conferences*, 53:09006, 2013.
- [46] M. Panasyuk et al. Ultra high energy cosmic ray detector KLYPVE on board the Russian Segment of the ISS. In *Proceedings of the 34th International Cosmic Ray Conference 2015, The Hague, The Netherlands*, 2015. PoS (ICRC 2015) 255.
- [47] M. Casolino et al. Detecting ultra-high energy cosmic rays from space with unprecedented acceptance: objectives and design of the jem-euso mission. *Astrophysics and Space Sciences Transactions*, 7(4):477–482, 2011.
- [48] J. V. Jelley, J. H. Fruin, N. A. Porter, et al. Radio Pulses from Extensive Cosmic-Ray Air Showers. *Nature*, 205:327–328, 1965.
- [49] F. D. Kahn and I. Lerche. Radiation from cosmic ray air showers. In *Proceedings of the Royal Society of London. Series A, Mathematical and Physical Sciences*, volume 289, page 206, 1966.
- [50] G. A. Askaryan. Excess negative charge of an electron-photon shower and its coherent radio emission. *Soviet Physics JETP*, 14:441, 1962.
- [51] H. R. Allan and R. W. Clay. Radio Pulses from Extensive Air Showers. *Nature*, 227:1116–1118, September 1970.
- [52] H. Falcke et al. (LOPES Collaboration). Detection and imaging of atmospheric radio flashes from cosmic ray air showers. *Nature*, 435:313–316, 2005.
- [53] D. Ardouin et al. Radio-detection signature of high-energy cosmic rays by the CODALEMA experiment. *Nuclear Instruments and Methods in Physics Research Section A: Accelerators, Spectrometers, Detectors and Associated Equipment*, 555(1–2):148 – 163, 2005.
- [54] T. Huege, M. Ludwig, and C.W. James. Simulating radio emission from air showers with CoREAS. *AIP Conf.Proc.*, 1535:128, 2013.
- [55] Jaime Alvarez-Muniz, Washington R. Carvalho, Jr., and Enrique Zas. Monte Carlo simulations of radio pulses in atmospheric showers using ZHAireS. *Astropart. Phys.*, 35:325–341, 2012.
- [56] Klaus Werner, Krijn D. de Vries, and Olaf Scholten. A Realistic Treatment of Geomagnetic Cherenkov Radiation from Cosmic Ray Air Showers. *Astropart. Phys.*, 37:5–16, 2012.
- [57] L. D. Landau and E. M. Lifshitz. *The classical theory of fields*. Pergamon Press, Oxford, 1998. ISBN: 0-7506-2768-9.
- [58] Klaus Werner and Olaf Scholten. Macroscopic treatment of radio emission from cosmic ray air showers based on shower simulations. *Astroparticle Physics*, 29(6):393–411, 2008.

-
- [59] T. Huege and H. Falcke. Radio emission from cosmic ray air showers. Coherent geosynchrotron radiation. *Astronomy & Astrophysics*, 412:19–34, 2003.
- [60] S. Buitink et al. (LOPES Collaboration). Amplified radio emission from cosmic ray air showers in thunderstorms. *Astronomy & Astrophysics*, 467:385–394, 2007.
- [61] G. A. Askaryan. Coherent radio emission from cosmic showers in air and in dense media. *Soviet Physics JETP*, 21:658, 1965.
- [62] V.L. Ginzburg. Transition radiation and transition scattering. *Physica Scripta*, 1982(T2A):182, 1982.
- [63] Krijn D. de Vries et al. The cosmic-ray air-shower signal in Askaryan radio detectors. *Astropart. Phys.*, 74:96–104, 2016.
- [64] P.W. Gorham et al. Observations of microwave continuum emission from air shower plasmas. *Physical Review D*, 78(3):032007, 2008.
- [65] R. Šmída et al. First Experimental Characterization of Microwave Emission from Cosmic Ray Air Showers. *Phys. Rev. Lett.*, 113(22):221101, 2014.
- [66] D. Heck, J. Knapp, J. N. Capdevielle, et al. CORSIKA: A Monte Carlo Code to Simulate Extensive Air Showers. FZKA Report 6019, Forschungszentrum Karlsruhe, 1998.
- [67] S. J. Sciutto. AIRES: A System for air shower simulations. User’s guide and reference manual. Version 2.2.0. 1999.
- [68] T. Pierog, M.K. Alekseeva, Till Bergmann, V. Chernatkin, R. Engel, et al. First results of fast one-dimensional hybrid simulation of EAS using CONEX. *Nucl.Phys.Proc.Suppl.*, 151:159–162, 2006.
- [69] N.N. Kalmykov and A.A. Konstantinov. Macroscopic model of radio emission from extensive air showers. *Physics of Atomic Nuclei*, 74(7):1019–1031, 2011.
- [70] E. Zas, F. Halzen, and T. Stanev. Electromagnetic pulses from high-energy showers: Implications for neutrino detection. *Phys. Rev. D*, 45:362–376, Jan 1992.
- [71] Clancy W. James, Heino Falcke, Tim Huege, and Marianne Ludwig. General description of electromagnetic radiation processes based on instantaneous charge acceleration in “endpoints”. *Phys. Rev. E*, 84:056602, Nov 2011.
- [72] P. A. Bezyazeev et al. (Tunka-Rex Collaboration). Measurement of cosmic-ray air showers with the Tunka Radio Extension (Tunka-Rex). *Nucl. Instrum. Meth.*, A802:89–96, 2015.
- [73] T. Huege. Theory and simulations of air shower radio emission. *AIP Conf.Proc.*, 1535:121, 2013.
- [74] Konstantin Belov. Radio emission from Air Showers. Comparison of theoretical approaches. *AIP Conf. Proc.*, 1535:157, 2013.

- [75] S. N. Vernov, G. B. Khristiansen, A. T. Abrosimov, V. B. Atrashkevitch, et al. Detection of radio emission from extensive air showers with a system of single half-wave dipoles. *Canadian Journal of Physics*, 46(10):S241–S242, 1968.
- [76] B. McBreen, E.P O'Mongain, N.A. Porter, and P.J. Slevin. Correlation between optical and radio emission from extensive air showers at large zenith angles. *Physics Letters*, 23(11):677 – 678, 1966.
- [77] P. R. Barker, W. E. Hazen, and A. Z. Hendel. Radio pulses from cosmic-ray air showers. *Phys. Rev. Lett.*, 18:51–54, Jan 1967.
- [78] J. R. Prescott, G. G. C. Palumbo, J. A. Galt, and C. H. Costain. Radio signals from air showers at 22 MHz. *Canadian Journal of Physics*, 46(10):S246–S249, 1968.
- [79] Pedro Abreu et al. Results of a self-triggered prototype system for radio-detection of extensive air showers at the Pierre Auger Observatory. *JINST*, 7:P11023, 2012.
- [80] T. Antoni et al. (KASCADE Collaboration). The Cosmic ray experiment KASCADE. *Nucl. Instrum. Meth.*, A513:490–510, 2003.
- [81] W. D. Apel et al. (LOPES Collaboration). Experimental evidence for the sensitivity of the air-shower radio signal to the longitudinal shower development. *Phys. Rev.*, D85:071101, 2012.
- [82] W. D. Apel et al. (LOPES Collaboration). Reconstruction of the energy and depth of maximum of cosmic-ray air showers from LOPES radio measurements. *Phys.Rev.*, D90(6):062001, 2014.
- [83] O. Ravel et al. (CODALEMA Collaboration). The CODALEMA experiment. *Nucl. Instrum. Meth.*, A662:S89–S94, 2012.
- [84] Lilian Martin et al. (CODALEMA Collaboration). Investigating the extensive air shower properties: Tackling the challenges of the next generation cosmic ray observatory with the CODALEMA experiment. *Nucl. Instrum. Meth.*, A742:107–114, 2014.
- [85] M. P. van Haarlem et al. LOFAR: The LOw-Frequency ARray. *Astronomy & Astrophysics*, 556:A2, August 2013.
- [86] A. Nelles et al. A new way of air shower detection: measuring the properties of cosmic rays with LOFAR. *J. Phys. Conf. Ser.*, 632(1):012018, 2015.
- [87] S. Buitink et al. Method for high precision reconstruction of air shower X_{max} using two-dimensional radio intensity profiles. *Phys. Rev.*, D90(8):082003, 2014.
- [88] P. Schellart, S. Buitink, A. Corstanje, J.E. Enriquez, H. Falcke, et al. Polarized radio emission from extensive air showers measured with LOFAR. *JCAP*, 1410(10):014, 2014.
- [89] The Pierre Auger Cosmic Ray Observatory. *Nucl. Instrum. Meth.*, A798:172–213, 2015.
- [90] A. Aab et al. (Pierre Auger Collaboration). Probing the radio emission from air showers with polarization measurements. *Phys.Rev.*, D89(5):052002, 2014.

-
- [91] A. Aab et al. (Pierre Auger Collaboration). Energy Estimation of Cosmic Rays with the Engineering Radio Array of the Pierre Auger Observatory. *Submitted to: Phys. Rev. D*, 2015. arXiv:1508.04267.
- [92] A. A. Ivanov, S. P. Knurenko, and I. Ye. Sleptsov. Measuring extensive air showers with Cherenkov light detectors of the Yakutsk array: the energy spectrum of cosmic rays. *New Journal of Physics*, 11(6):065008, 2009.
- [93] Stanislav Knurenko and Igor Petrov. Radio signal correlation at 32 MHz with extensive air showers parameters. *Journal of Physics: Conference Series*, 632(1):012100, 2015.
- [94] I. Petrov et al. Depth of Maximum Development of Extensive Air Showers by Radio Emission Data at Yakutsk EAS Array. In *Proceedings of the 34th International Cosmic Ray Conference 2015, The Hague, The Netherlands*, page PoS (ICRC 2015) 255, 2015.
- [95] Chris L. Carilli and S. Rawlings. Science with the Square Kilometer Array: Motivation, key science projects, standards and assumptions. *New Astron. Rev.*, 48:979, 2004.
- [96] Tim Huege et al. Precision measurements of cosmic ray air showers with the SKA. *PoS, AASKA14:148*, 2015.
- [97] D. Ardouin et al. First detection of extensive air showers by the TREND self-triggering radio experiment. *Astropart. Phys.*, 34:717–731, 2011.
- [98] P. W. Gorham et al. The Antarctic Impulsive Transient Antenna Ultra-high Energy Neutrino Detector Design, Performance, and Sensitivity for 2006-2007 Balloon Flight. *Astropart. Phys.*, 32:10–41, 2009.
- [99] P. W. Gorham et al. Observational Constraints on the Ultra-high Energy Cosmic Neutrino Flux from the Second Flight of the ANITA Experiment. *Phys. Rev.*, D82:022004, 2010. [Erratum: *Phys. Rev.*D85,049901(2012)].
- [100] S. Hoover et al. Observation of Ultra-high-energy Cosmic Rays with the ANITA Balloon-borne Radio Interferometer. *Phys. Rev. Lett.*, 105:151101, 2010.
- [101] Ilya Kravchenko, S. Hussain, Dave Seckel, Dave Besson, E. Fensholt, John Ralston, John Taylor, Ken Ratzlaff, and Rob Young. Updated Results from the RICE Experiment and Future Prospects for Ultra-High Energy Neutrino Detection at the South Pole. *Phys. Rev.*, D85:062004, 2012.
- [102] P. Allison et al. Design and Initial Performance of the Askaryan Radio Array Prototype EeV Neutrino Detector at the South Pole. *Astropart. Phys.*, 35:457–477, 2012.
- [103] H. Landsman, L. Ruckman, and G. S. Varner. AURA - A radio frequency extension to IceCube. *Nucl. Instrum. Meth.*, A604:S70–S75, 2009.
- [104] Steven W. Barwick. ARIANNA: A New Concept for UHE Neutrino Detection. *J. Phys. Conf. Ser.*, 60:276–283, 2007.
- [105] P. Allison et al. First Constraints on the Ultra-High Energy Neutrino Flux from a Prototype Station of the Askaryan Radio Array. *Astropart. Phys.*, 70:62–80, 2015.

- [106] S. W. Barwick et al. Livetime and sensitivity of the ARIANNA Hexagonal Radio Array. In *Proceedings of the 34th International Cosmic Ray Conference 2015, The Hague, The Netherlands*, 2015. arXiv:1509.00115.
- [107] A. G. Vieregge, K. Bechtol, and A. Romero-Wolf. A Technique for Detection of PeV Neutrinos Using a Phased Radio Array. *JCAP*, 1602(02):005, 2016.
- [108] Nam, J. et al. Taiwan Astroparticle Radiowave Observatory for Geo-synchrotron Emissions (TAROGÉ). In *Proceedings of the 34th International Cosmic Ray Conference 2015, The Hague, The Netherlands*, 2015. PoS (ICRC 2015) 663.
- [109] P. M. S. Blackett and A. C. B. Lovell. Radio echoes and cosmic ray showers. *Proceedings of the Royal Society of London A: Mathematical, Physical and Engineering Sciences*, 177(969):183–186, 1941.
- [110] Peter W. Gorham. On the possibility of radar echo detection of ultrahigh-energy cosmic ray induced and neutrino induced extensive air showers. *Astropart. Phys.*, 15:177–202, 2001.
- [111] M. I. Bakunov, A. V. Maslov, A. L. Novokovskaya, and A. Kryemadhi. The no-reflection regime of radar detection of cosmic ray air showers. *New J. Phys.*, 17(5):053015, 2015.
- [112] R. Abbasi et al. Telescope Array Radar (TARA) Observatory for Ultra-High Energy Cosmic Rays. *Nucl. Instrum. Meth.*, A767:322–338, 2014.
- [113] J. Stasielak, R. Engel, S. Baur, P. Neunteufel, R. Šmída, F. Werner, and H. Wilczyński. Feasibility of radar detection of extensive air showers. *Astropart. Phys.*, 73:14–27, 2016.
- [114] Krijn D. de Vries, Kael Hanson, and Thomas Meures. On the feasibility of RADAR detection of high-energy neutrino-induced showers in ice. *Astropart. Phys.*, 60:25–31, 2014.
- [115] M. G. Aartsen et al. Evidence for High-Energy Extraterrestrial Neutrinos at the Ice-Cube Detector. *Science*, 342:1242856, 2013.
- [116] A. D. Avrorin et al. The prototyping/early construction phase of the BAIKAL-GVD project. *Nucl. Instrum. Meth.*, A742:82–88, 2014.
- [117] Tim Huege and Clancy W. James. Full Monte Carlo simulations of radio emission from extensive air showers with CoREAS. In *Proceedings, 33rd International Cosmic Ray Conference (ICRC2013)*, 2013.
- [118] ITU (International Telecommunication Union). Radio noise. Recommendation ITU-R P.372-12, ITU, Geneva, Switzerland, 2015.
- [119] S.F. Berezhnev, D. Besson, N.M. Budnev, A. Chiavassa, O.A. Chvalaev, et al. The Tunka-133 EAS Cherenkov light array: status of 2011. *Nucl. Instrum. Meth.*, A692:98–105, 2012.
- [120] O.A. Gress et al. The study of primary cosmic rays energy spectrum and mass composition in the energy range 0.5 – 50 PeV with Tunka EAS Cherenkov array. *Nuclear Physics B - Proceedings Supplements*, 75(1–2):299 – 301, 1999.

-
- [121] N. Budnev et al. Tunka-25 Air Shower Cherenkov array: The main results. *Astroparticle Physics*, 50–52:18 – 25, 2013.
- [122] B. A. Antokhonov et al. The new Tunka-133 EAS Cherenkov array: Status of 2009. *Nucl. Instrum. Meth.*, A628:124–127, 2011.
- [123] N. M. Budnev et al. TAIGA the Tunka Advanced Instrument for cosmic ray physics and Gamma Astronomy - present status and perspectives. *JINST*, 9(09):C09021, 2014.
- [124] Bayarto Lubsandorzhev. Cherenkov experiments in the Tunka Valley. *Nucl. Instrum. Meth.*, A766:52–56, 2014.
- [125] Martin Tluczykont, Daniel Hampf, Dieter Horns, Dominik Spitschan, Leonid Kuzmichev, Vasily Prosin, Christian Spiering, and Ralf Wischnewski. The HiSCORE concept for gamma-ray and cosmic-ray astrophysics beyond 10 TeV. *Astropart. Phys.*, 56:42–53, 2014.
- [126] S. F. Berezhnev et al. First results from the operation of the prototype Tunka-HiSCORE array. *Bull. Russ. Acad. Sci. Phys.*, 79(3):348–351, 2015. [Izv. Ross. Akad. Nauk Ser. Fiz.79,no.3,381–384(2015)].
- [127] W. D. Apel et al. (KASCADE-Grande Collaboration). The KASCADE-Grande experiment. *Nucl. Instrum. Meth.*, A620:202–216, 2010.
- [128] I. Yashin et al. Depth of Maximum Development of Extensive Air Showers by Radio Emission Data at Yakutsk EAS Array. In *Proceedings of the 34th International Cosmic Ray Conference 2015, The Hague, The Netherlands*, 2015. PoS (ICRC 2015) 986.
- [129] J. Oertlin. Radio Data Analysis of a Prototype Antenna at the Tunka-133 Experiment. Bachelor Thesis, Karlsruhe Institute of Technology, 2011.
- [130] O. Krömer et al. (LOPES Collaboration). New Antenna for Radio Detection of UHECR. In *Proceedings of the 31st ICRC, Łódź, Poland*, number 1232, 2009. <http://icrc2009.uni.lodz.pl/proc/html/>.
- [131] Pedro Abreu et al. Antennas for the Detection of Radio Emission Pulses from Cosmic-Ray. *JINST*, 7:P10011, 2012.
- [132] Y. Kazarina. Investigation of the structure of radio emission from high energy extensive air-showers on the Tunka experiment. PhD Thesis, Irkutsk State University, Russia, 2016.
- [133] R. Hiller. Signal and event reconstruction with the radio signal of UHECR with the Tunka Radio Extension (Tunka-Rex). PhD Thesis, Karlsruhe Institut für Technologie, Germany, 2016.
- [134] V. V. Prosin et al. Primary CR energy spectrum and mass composition by the data of Tunka-133 array. *EPJ Web Conf.*, 99:04002, 2015.
- [135] P. Abreu et al. Advanced functionality for radio analysis in the Offline software framework of the Pierre Auger Observatory. *Nucl.Instrum.Meth.*, A635:92–102, 2011.

- [136] F.G. Schröder, T. Asch, L. Bähren, J. Blümer, H. Bozdog, H. Falcke, A. Haungs, A. Horneffer, T. Huege, P.G. Isar, O. Krömer, and S. Nehls. New method for the time calibration of an interferometric radio antenna array. *Nuclear Instruments and Methods in Physics Research Section A: Accelerators, Spectrometers, Detectors and Associated Equipment*, 615(3):277 – 284, 2010.
- [137] F. G. Schröder et al. The Tunka Radio Extension (Tunka-Rex): Radio Measurements of Cosmic Rays in Siberia (PISA 2015). In *13th Pisa Meeting on Advanced Detectors: Frontier Detectors for Frontier Physics La Biodola, Isola d'Elba, Livorno, Italy, May 24-30, 2015*, 2015. doi:10.1016/j.nima.2015.08.075.
- [138] D. Kostunin, P. A. Bezyazeekov, R. Hiller, F. G. Schröder, V. Lenok, and E. Levinson. Reconstruction of air-shower parameters for large-scale radio detectors using the lateral distribution. *Astroparticle Physics*, 74:79–86, 2015.
- [139] H. R. Allan. Radio Emission From Extensive Air Showers. *Progress in Elementary Particle and Cosmic Ray Physics*, Vol. 10:171–302, 1971.
- [140] S. Grebe and Pierre Auger Collaboration. Spectral index analysis of the data from the Auger Engineering Radio Array. *AIP Conference Proceedings*, 1535(1):73–77, 2013.
- [141] Sergey Ostapchenko. Monte Carlo treatment of hadronic interactions in enhanced Pomeron scheme: I. QGSJET-II model. *Phys.Rev.*, D83:014018, 2011.
- [142] Alfredo Ferrari, Paola R. Sala, Alberto Fassio, and Johannes Ranft. FLUKA: A multi-particle transport code (Program version 2005). 2005.
- [143] D. Kostunin. SiMulation Management software. *In preparation*, 2016.
- [144] David Saltzberg, Peter Gorham, Dieter Walz, Clive Field, Richard Iverson, et al. Observation of the Askaryan effect: Coherent microwave Cherenkov emission from charge asymmetry in high-energy particle cascades. *Phys.Rev.Lett.*, 86:2802–2805, 2001.
- [145] K. Belov et al. Accelerator measurements of magnetically-induced radio emission from particle cascades with applications to cosmic-ray air showers. 2015. SLAC-PUB-16338, arXiv:1507.07296.
- [146] Krijn D. de Vries, Olaf Scholten, and Klaus Werner. The air shower maximum probed by Cherenkov effects from radio emission. *Astropart.Phys.*, 45:23–27, 2013.
- [147] W.D. Apel, J.C. Arteaga-Velázquez, L. Bähren, K. Bekk, M. Bertaina, et al. The wave-front of the radio signal emitted by cosmic ray air showers. *JCAP*, 1409(09):025, 2014.
- [148] Anna Nelles, Stijn Buitink, Heino Falcke, Jörg Hörandel, Tim Huege, et al. A parameterization for the radio emission of air showers as predicted by CoREAS simulations and applied to LOFAR measurements. *Astropart.Phys.*, 60:13–24, 2014.
- [149] Nikolai N. Kalmykov and Andrey A. Konstantinov. Lateral distribution of radio emission and its dependence on air shower longitudinal development. *Journal of Cosmology and Astroparticle Physics*, 2012(12):029, 2012.

-
- [150] O. V. Vedeneev. Depth of the maximum of extensive air showers and mass composition of primary cosmic radiation at an energy of 4×10^{17} eV according to data on radioemission from extensive air showers. *Phys. Atom. Nucl.*, 72:250–256, 2009. [Yad. Fiz.72,277(2009)].
- [151] D. Kostunin et al. (Tunka-Rex Collaboration). The Tunka Radio Extension: Latest Analysis Results. *J. Phys. Conf. Ser.*, 632(1):012096, 2015.
- [152] D. Kostunin et al. The Tunka Radio Extension: two years of air-shower measurements. In *Proceedings of the 34th International Cosmic Ray Conference 2015, The Hague, The Netherlands*, 2015. PoS (ICRC 2015) 285.
- [153] T. Huege, R. Ulrich, and R. Engel. Energy and composition sensitivity of geosynchrotron radio emission from cosmic ray air showers. *Astropart.Phys.*, 30:96, 2008.
- [154] H. R. Allan, R. W. Clay, and J. K. Jones. Frequency spectrum of air shower radio pulses. *Nature*, 225:253–254, 1970.
- [155] F.G. Schröder et al. On noise treatment in radio measurements of cosmic ray air showers. *Nuclear Instruments and Methods in Physics Research Section A: Accelerators, Spectrometers, Detectors and Associated Equipment*, 662, Supplement 1:S238 – S241, 2012. 4th International workshop on Acoustic and Radio EeV Neutrino detection Activities.
- [156] The Radio Offline Group (Pierre Auger Collaboration). The radio extension of auger offline. Auger internal note GAP-2010-056, 2010.
- [157] P. A. Bezyazeev et al. Radio measurements of the energy and the depth of the shower maximum of cosmic-ray air showers by Tunka-Rex. *JCAP*, 1601(01):052, 2016.
- [158] Erwan Thebault et al. International geomagnetic reference field: the 12th generation. *Earth, Planets and Space*, 67(1):79, 2015.
- [159] A. Chulliat et al. The US/UK World Magnetic Model for 2015-2020: Technical Report, National Geophysical Data Center, NOAA. 2015.

List of Figures

2.1. Fluxes of the primaries of low-energy cosmic rays	4
2.2. The all-particle spectrum measured with various air-shower techniques . . .	5
2.3. Updated Hillas plot taking into account radiation losses	6
2.4. Principle description of an air-shower produced by a high-energy proton . .	7
3.1. Schematic representation of the main contributions to the radio emission from air-showers	12
3.2. Lateral distribution of components of the electrical field induced by an air- shower on the surface of the detector	13
3.3. Radio emission from a vertical air-shower with primary energy of 1 EeV simulated with CoREAS	14
3.4. Sources of radio background at MHz frequencies	17
4.1. Development stages of the Tunka-133 detector	19
4.2. Tunka-133 PMT	20
4.3. HiSCORE station installed at the Tunka facility	21
4.4. External and internal view of a Tunka-Grande station	21
4.5. Map of the Tunka facility as of 2013	23
4.6. A Tunka-Rex antenna station	25
4.7. Internal view of Tunka-133 cluster center	25
4.8. Schematic signal chain of a Tunka-Rex antenna	26
4.9. Distributions of peaks in the radio traces (times of maximum amplitude) . .	27
4.10. Scheme of the data acquisition of Tunka-133/Tunka-Rex	28
4.11. The mean background spectrum in one night of operation	29
4.12. Trace of the radio signal from air-showers before correcting for the antenna pattern	30
4.13. Example event reconstructed by Tunka-Rex	30
4.14. Spectra of Tunka-Rex antennas stations measured with the beacon switched on	31
4.15. Spectra of the background at antenna station 15 measured on January 2013	32
4.16. Noise fluctuations and their correlation with the temperature inside the clus- ter center during a single run (one night)	33
5.1. Coherence limits during air-shower development with respect to the observer	36
5.2. Schematic representation of the shower-maximum fitting procedure	39
5.3. Shower maximum reconstructed by Tunka-133 in comparison with Tunka- Rex simulations	40
5.4. Comparison of lateral distributions of Tunka-Rex events from 2012-2013, and simulations using proton and iron primaries	41
5.5. Schematic representation of a three-dimensional simulation	42
5.6. Averaged asymmetry profile of the radio lateral distribution for protons and iron nuclei	45

5.7. Distribution of the asymmetry against the distance to the shower axis for different observation depths	46
5.8. Comparison between experimental observations of the asymmetry and their theoretical prediction made for Tunka-Rex	47
5.9. Quality of the asymmetry correction	47
5.10. Comparison between different methods of correction for about 300 simulated showers	48
5.11. Example events before and after asymmetry correction	49
5.12. Distribution of the quality of LDF fits for different parameterizations	51
5.13. Correlation between Gaussian LDF properties and distance to shower maximum	52
5.14. Correlation between logarithms of amplitude and energy, and precision of the energy reconstruction	53
5.15. Contour plot of the correlation between LDF slope η and true X_{\max} depending on the LDF parameter r_x and the free parameter \bar{b}	53
5.16. Comparison between true and reconstructed primary energy and shower maximum of the CoREAS simulations	54
5.17. Dependence of the primary-energy reconstruction on the distance to shower maximum and zenith of arrival direction	56
5.18. Dependence of the shower-maximum reconstruction on the primary energy and zenith of the arrival direction	56
5.19. Comparison between true and reconstructed primary energy and shower maximum of the CoREAS simulations after adding background samples	57
6.1. Fraction between true and measured amplitudes after adding noise	62
6.2. Example event with rejected antenna station	63
6.3. Distribution of the antennas per event for the Tuning and Prediction seasons	64
6.4. Correlation of LDF parameters with cosine of the zenith angle of the arrival direction for CoREAS simulations	65
6.5. Dependence of the parameters a_{20} and a_{21} on the primary energy	65
6.6. Example events with underestimation of the slope of the lateral distribution	67
6.7. Different types of low-quality events (rejected by quality cuts)	68
6.8. Angular distribution of arrival directions	70
6.9. Distribution of shower cores of detected events	70
6.10. Primary energy and atmospheric depth of shower maximum distributions reconstructed with Tunka-Rex for tuning and prediction seasons	71
6.11. Correlation of the shower energy reconstructed with Tunka-Rex radio and Tunka-133 air-Cherenkov measurements for Tuning and Prediction seasons	72
6.12. Histograms of the relative deviation between the Tunka-133 and Tunka-Rex energy reconstructions for the Tuning and Prediction seasons	72
6.13. Correlation of the distance to shower maximum as reconstructed with Tunka-Rex radio and Tunka-133 air-Cherenkov measurements for the Tuning and Prediction seasons	73
6.14. Histograms of the difference between the Tunka-133 and Tunka-Rex shower maximum reconstructions for the Tuning and Prediction seasons	73
6.15. Correlation of the shower energy reconstructed with Tunka-Rex radio and Tunka-133 air-Cherenkov measurements for the merged dataset (2012-2014)	76

6.16. Correlation of the distance to shower maximum as reconstructed with Tunka-Rex radio and Tunka-133 air-Cherenkov measurements for the merged dataset (2012-2014)	76
6.17. Distributions of the energy and the atmospheric depth of the shower maximum as reconstructed by Tunka-Rex and Tunka-133 for the merged dataset (2012-2014)	77
6.18. The number of Tunka-Rex events with energy and shower maximum reconstruction to total number of triggered Tunka-133 events	77
6.19. Mean experimental depth of maximum versus the primary energy reconstructed by the Tunka-133 and Tunka-Rex experiments	78
A.1. Background spectrum measured on the antenna attached to HiSCORE detector	83
B.1. Principal scheme of the SiMM software	87
C.1. Correlation of the distance to the shower maximum between Tunka-133 and Tunka-Rex arrays, when Tunka-Rex uses the simplest LDF parameterization	90
D.1. Strength of the Earth's magnetic field predicted by WMM2015 with radio setups measuring geomagnetic emission	92

List of Tables

2.1. Comparison chart of air-shower detection techniques	10
4.1. Systematic uncertainties of Tunka-133	26
5.1. Geometrical properties of the Tunka site	40
5.2. Configuration of the tomographic simulation	43
5.3. Global fit values for the asymmetry-profile fit in Fig. 5.6 of averaged CoREAS simulations (from the T-SET).	46
6.1. Open and hidden parameters for the Tuning and Prediction seasons	60
6.2. Parameters for Eq. (6.9) for a_2 coefficient in LDF	66
6.3. Statistics of events in both seasons after selection and quality cuts	69
6.4. Summary of the cross-check between the air-shower reconstructions of Tunka-133 and Tunka-Rex (measurements in 2012-2014)	74
6.5. Summary of dataset merged of both seasons (2012-2014) reconstructed with additional quality cut excluding outer events	75
B.1. Example CORSIKA steering card for a proton event with energy of 0.1 EeV .	87
C.1. Comparison of the resolutions of air-shower reconstructions given by standard and simplified methods	90

List of Abbreviations

a.s.l.	above sea level
AERA	Auger Engineering Radio Array
AGN	Active Galactic Nuclei
Aires	Air-shower Extended Simulations
ANITA	Antarctic Impulsive Transient Antenna
CODALEMA	COsmic ray Detection Array with Logarithmic ElectroMagnetic Antennas
CoREAS	CORSIKA-based Radio Emission from Air Showers
CORSIKA	COsmic Ray SIMulations for KAscade
CROME	Cosmic-Ray Observation via Microwave Emission
DAQ	Data acquisition
EAS	extensive air-shower
EeV	exa electron volt (10^{18} eV)
eV	electron volt
FADC	fast analog-digital converter
FLUKA	FLUktuierende KAskade
GVD	Giga-volume detector
GZK	Greisen – Zatsepin – Kuzmin [cut-off]
HAS	Horizontal air-shower
HiSCORE	Hundred* <i>i</i> Square-km Cosmic ORigin Explorer
HRJRG	Helmholtz Russian Joint Research Group
IACT	Imaging atmosphere(air)-Čerenkov Telescope
IGRF	International Geomagnetic Reference Field
ISS	International Space Station
JEM-EUSO	Japanese Experiment Module – Extreme Universe Space Observatory
KASCADE	KARlsruhe Shower Core and Array DEtector

KLYPVE	Cosmic Rays of Extremely High Energy (russian <i>Kosmicheskie Luchi Predel'no Vysokikh Energiy</i>)
LDF	Lateral distribution function
LNA	Low-noise amplifier
LOFAR	LOW-Frequency ARray
LOPES	LOFAR Prototype Station
LPDA	Logarithmic Periodic Dipole Antenna
MGMR	Macroscopic model of GeoMagnetic Radiation
MSU	Moscow State University
NKG	Nishimura-Kamata-Greisen [parameterization]
PAO	Pierre Auger Observatory
PDG	Particle data group
PMT	Photomultiplier tube
QGSJET	Quark-Gluon String JET [model]
RFI	Radio Frequency Interference
RMS	Root-mean-square
SALLA	Short aperiodic loop antenna
SiMM	SiMulation Manager
SKA	Square Kilometre Array
SNR	Signal-to-noise ratio
TAIGA	Tunka Advanced Instrument for cosmic ray physics and Gamma Astronomy
TARA	Telescope Array RAdar
TAROGÉ	Taiwan Astroparticle Radiowave Observatory
TREND	Tianshan Radio Experiment for Neutrino Detection
TRex	Tunka-Rex (using for detector stages and in software)
Tunka-Rex	Tunka Radio Extension
WMM	World Magnetic Model
ZHAires	ZHS + AIRES [model]
ZHS	Zas – Halzen – Stanev [model]

Acknowledgement

I would like to acknowledge people who made this work possible and who assisted me during the writing of my thesis.

First, I would like to thank my referee, Prof. Johannes Blümer for giving me an opportunity to working on this subject, and Prof. Michael Feindt for acting as co-referee.

My supervisor, Frank G. Schröder, has played very important role from the very beginning of my work and until writing was finished. It is hard to count each aspect of my scientific activity which was contributed to by Frank. His leadership and organisatory abilities made the success of this experiment possible. In an hour of need he is always ready to lend his shoulder or give an advice to his colleagues.

My colleague and officemate, Roman Hiller, became my good friend during years working on Tunka-Rex. I am happy to work together with him on one team, our discussions are very useful and productive. Also I thank him for his valuable support relating my stay in Germany.

Furthermore, I would like to thank my colleagues in the cosmic-ray group at KIT. Andreas Haungs, a key scientist of Tunka-Rex, with his extensive experience in the topic, often pointed me to the right directions. Matthias Kleifges, the vice head of IPE, made possible the production of electronics for the each stage of experiment. Tim Huege, creator and guru of CoREAS, gave me many recommendations for the calculation of the radio emission from cosmic rays. I thank William Painter for the proof-reading of the text of my thesis. I cannot list everybody of my colleagues from KIT, but I also would like to give a mention to Qader Dorosti, Igor Katkov, Victor Trusov, Doris Wochele, Sabine Bucher, Marie-Christine Kauffmann, Michael Gahr and Hartmut Speck.

Not least important is the support, which I obtained from my colleagues from Russia. I would like to acknowledge Leonid Kuzmichev and Nicolai Budnev, the heads of Tunka facility. Vasiliy Prosin and Nicolai Kalmykov brought me priceless advice, which defined the main direction of my study. The large part of Tunka-Rex success is made by the people involved in Tunka/TAIGA activities: Elena Korostyleva, Oleg Gress, Rashid Mirgazov, Yulia Kazarina, Oleg Fedorov, Alexey Zagorodnikov, Alexander Pahorukov, Eugeniy Konstantinov, Sergey Epimakhov, Grigory Rubtsov and many others. I especially thank my co-authors and best friends Vladimir Lenok for the design of Tunka-Rex logo and Eduard Levinson for his assistance during deployment of Tunka-Rex, as well as Pavel Bezyazeev, my diploma student, who also taught me a lot.

I am also grateful to my teachers and colleagues from other institutes, who inspired my scientific activity: Alexander Vall, Mikhail Volkov, Andrei Arbuzov, Maxim Polyakov, Konstantin Belov.

Last, but certainly not least, I thank my family and my friends.